The Pennsylvania State University

The Graduate School

College of Engineering

STABILITY OF LOW DAMPING RUBBER AND LEAD-RUBBER SEISMIC ISOLATION BEARINGS

A Thesis in

Civil Engineering

by

Jared R. Weisman

Submitted in Partial Fulfillment
of the Requirements
for the Degree of

Master of Science

August 2010

The thesis of Jared R. Weisman was reviewed and approved* by the following:

Gordon P. Warn
Assistant Professor of Civil Engineering
Thesis Adviser

Maria M. Lopez de Murphy
Associate Professor of Civil Engineering

Ali M. Memari
Associate Professor of Architectural Engineering

Peggy A. Johnson
Department Head & Professor of Civil Engineering

*Signatures are on file in the Graduate School.

ABSTRACT

Elastomeric bearings are one of the most commonly used types of seismic isolation devices. Composed of alternating layers of rubber and steel shims, this study focuses on elastomeric bearings made from low damping rubber with and without a lead core. AASHTO specifications require these bearings to remain stable both service loading as well as seismic loading. Stability under service loading is well understood and evaluated in a method similar to column buckling. During seismic loading some of the bearings in the isolation system are subjected to increased axial compressive loads at large displacements and their ability to sustain load in this configuration is less clear. At present, design for stability under these conditions is performed using the overlapping area method, which reduces the critical load calculated for service loading as a function of the area that overlaps between the top and bottom bearing end plates. Finite element and experimental investigations were conducted to evaluate the performance of the overlapping area method and to provide insight into finding an improved method for assessment of stability when bearings are laterally displaced. In addition, the use of a simple mechanical model to predict instability was explored.

The results of these studies showed that the overlapping area method fails to accurately capture trends observed in experiments and finite elements and that it provides inconsistent predictions between low damping rubber and lead-rubber bearings. The lead core was found to have negligible impact on bearing stability by comparison to the low damping rubber bearing. A two-dimensional parametric study performed in finite elements demonstrated the impact of several geometric properties that are ignored in the simplistic overlapping area formulation. The mechanical model that was studied better estimated the stability behavior for the low damping rubber bearing in the range of displacements of interest for design, but like the overlapping area method still lacks a significant theoretical foundation.

Table of Contents

List of Figures

List of Tables

CHAPTER 1

Introduction

1.1 Background

Seismic isolation is a method for reducing inertial forces that develop in a structure as a result of earthquake ground motion by shifting the natural period of vibration. This period shift is accomplished by decoupling a building superstructure from its supporting foundation via laterally flexible, yet vertically stiff elements called isolators (Figure 1.1a). During earthquake ground motion, the majority of shear deformation is concentrated across the isolation interface which must be accommodated by the individual isolators. One type of seismic isolation hardware commonly used in practice is the elastomeric bearing (Fig. 1.1b).

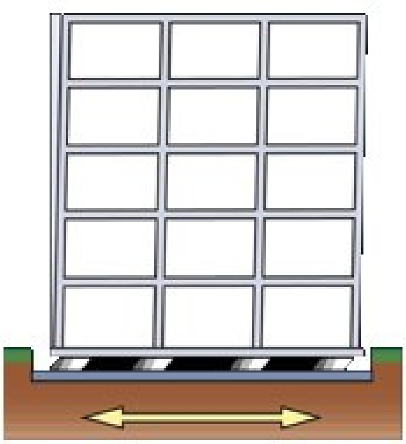

a) Illustration of isolated building (http://www.dis-inc.com/ seismic_isolation.html)

b) Bearing cross section

Figure 1.1 Seismic Isolation

Elastomeric bearings are composite structural elements consisting of alternating layers of rubber and steel shims. The rubber layers provide low shear stiffness whereas the close spacing of the steel shims provide increased vertical stiffness by restraining the bulging of the rubber. In cases where additional energy dissipation is required a lead core is added to a centrally located hole to form lead-rubber (LR) bearings.

During a maximum considered earthquake (MCE) event some of the elastomeric seismic isolation bearings (EBs) in a seismically isolated structure will be subject to simultaneous large lateral displacements and increased axial compressive load due to overturning forces (Fig. 1.2). As a result, one important consideration when designing seismic isolation systems is stability of the individual EBs in this deformed configuration.

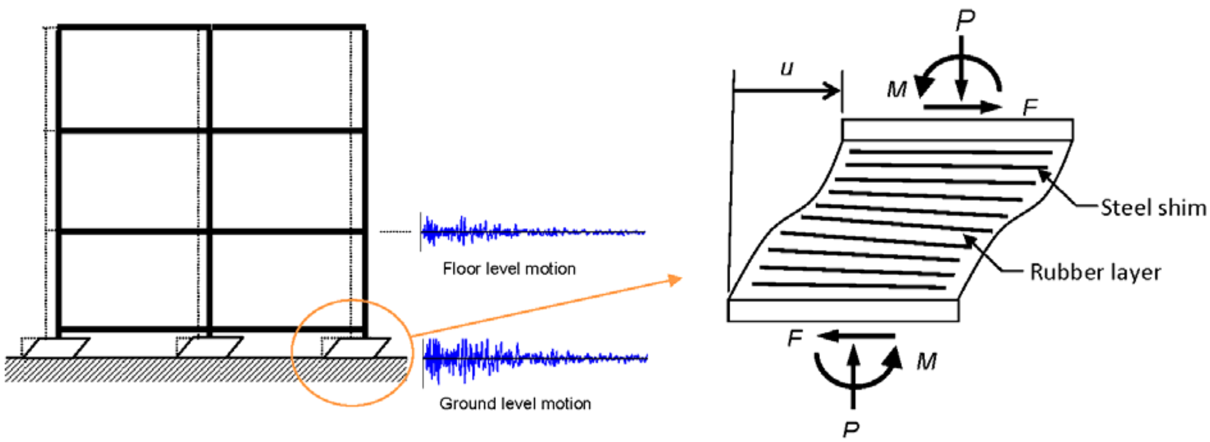

Figure 1.2 Loading for EBs in deformed configuration

Currently stability is assessed using procedures that have been adopted from the *AASHTO Guide Specifications for Seismic Isolation Design* (1999). The guide specifications require that each EB satisfy two stability criteria:

For service loading,

$$\frac{P_{cr}}{P_D + P_L} \geq 3 \tag{1-1}$$

where P_{cr} is the critical load at zero displacement, P_D is unfactored axial dead load, and P_L is the axial live load.

Under MCE loading,

$$P_{cr}^{'} \geq 1.2P_D + P_{SL} + P_{OT} \tag{1-2}$$

where $P_{cr}^{'}$ is the reduced critical load at the MCE displacement level, P_{SL} is the axial effect due to seismic live load, and P_{OT} is the axial load due to overturning.

The work presented in this thesis focuses on the determination of the reduced critical load, $P_{cr}^{'}$, of low damping rubber (LDR) and LR bearings. Although not specified in the codes of practice, stability under MCE conditions is typically checked using the overlapping area method introduced by Buckle and Liu (1994). The OLAM reduces the load carrying capacity of an EB in the undeformed configuration (P_{cr}, from Haringx 1949 and Gent 1964) using the ratio of the overlapping area between top and bottom bearing end plates (A_r) to the bonded rubber area (A_b) at a given displacement (u) as illustrated in Fig. 1.3.

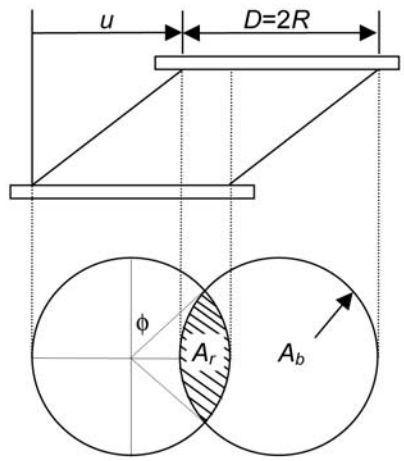

Figure 1.3 Overlapping area method

Using the OLAM, the reduced critical load, $P_{cr}^{'}$, is calculated as:

$$P_{cr}^{'} = P_{cr} \cdot \left(\frac{A_r}{A_b} \right) \tag{1-3}$$

While the OLAM provides a simple methodology for calculating $P_{cr}^{'}$, it lacks a rigorous theoretical basis and previous studies (Buckle and Liu 1994, Nagarajaiah and Ferrell 1999, Buckle et al. 2002) have suggested that the OLAM:

1. does not agree well with experimental data over a wide range of lateral displacements,
2. predicts zero load capacity at a lateral displacement equal to the bearing diameter, in contrast with experimental evidence.

1.2 Scope

This thesis will review research on stability of bolted LDR and LR seismic isolation bearings and expand the current knowledge with respect to stability in the deformed configuration using several analytical and experimental techniques. While previous research has concentrated only on LDR bearings with shape factors less than or equal to 5, this study will focus primarily on LDR and LR seismic isolation bearings having shape factors greater than 10 – values within a typical range of those used in seismic applications, where the shape factor, S, is a parameter of an EB defined as the ratio of the loaded area to the area free to bulge for an individual rubber layer that is illustrated in more detail in the body of this thesis.

1.3 Motivation

At present no experimental stability data exists for LR bearings or for LDR bearings with shape factors greater than 5. Further, it is unclear how well the overlapping area method performs for bearings with larger shape factors ($S \geq 10$) and lead-rubber bearings, though previous studies (Buckle and Liu 1994; Nagarajaiah and Ferrell 1999; Buckle et al. 2002) have shown it to be inconsistent in its predictions with variation of bearing geometry and displacement level. It is also unknown how the lead core will impact stability. Lastly, there still remains a gap in the fundamental understanding of instability in the deformed configuration.

1.4 Objectives

The principal goals of this study are to:

1. investigate the stability of LDR and LR EBs in the deformed configuration (reduced critical load) using finite element analysis (FEA) and experimental testing,
2. use this data to evaluate the OLAM, and
3. build on previous work (Nagarajaiah 1999) that explored an existing two-spring mechanical model as the basis for developing an improved formula that has a rational basis for predicting the reduced critical load of an LDR bearing for a wide range of shape factors and displacements.

CHAPTER 2

Literature Review

2.1 General

Stability refers to a structure or structural element's ability to return to an equilibrium position after being unloaded. When a structure becomes unstable it is no longer able to support an increase in load and will displace without bound unless another stable condition is reached. It should be noted that this research will focus on EBs with bolted, rather than doweled connections. Although bearings with doweled connections prevent the development of tensile stresses, bearings with that connection detail are susceptible to another type of instability termed "rollover" when laterally displaced.

Under service conditions elastomeric seismic isolation bearings (EBs) are subject to axial compressive loads and therefore are susceptible to instability in this undeformed configuration (UC) similarly to a column in a building.

During a seismic event the demands imposed on some EBs are exacerbated due to the combination of lateral displacement and simultaneous increase in axial compressive load due to overturning. Current design procedures require that all bearing remain stable (able to return to the UC) following the earthquake event. Therefore, stability must also be assessed in the laterally deformed configuration (DC).

This review considers several studies, in chronological order, from the simplest determination of stability in which only axial loads and bending deformations are considered (UC) to the laterally deformed (or post-buckling) configuration in which shear deformations are taken into account (DC).

2.2 Undeformed Configuration

Information related to the design for global stability of columns in the laterally undeformed configuration is well-documented. For columns where shear deformations can be neglected, critical loads can be predicted with reasonable accuracy using the Euler Buckling formula and effective length factors for a wide range of boundary conditions. However, in EBs with low shear moduli the shear deformations (neglected in the above) must be considered.

Engesser (1891) was the first to derive equations for buckling accounting for shear deformations. This derivation assumes the shear components of force and deformation act normal to the total slope of the column. While Engesser's formulations are reasonable (Roeder 1987), subsequent research and experimental testing (Gent 1964; Timoshenko and Gere 1961; Derham and Thomas 1981) suggest other research (Haringx 1948, 1949) provides a more accurate prediction of the buckling load for elastomeric bearings in the UC.

In Haringx's study of buckling in helical springs (extended to rubber rods and later to reinforced rubber bearings by Gent 1964) the shear components of force and displacement were assumed to act perpendicular to the bending (rather than total) slope. This fundamental deviation between Haringx's and Engesser's approaches resulted in a drastically different estimate of the critical load, P_{cr} (Roeder 1987).

For the first mode of buckling the Haringx formulation yields:

$$P_{cr} = \frac{\sqrt{P_s^2 + 4P_s \cdot P_E} - P_s}{2} \tag{2-1}$$

where P_{cr} denotes the critical load in the UC, P_s is the product of the shear modulus (G) and shear area (A_s), and P_E is the Euler Buckling Load $\left(\pi^2 EI / l^2\right)$.

For EBs, P_E is typical several magnitudes greater than P_S so that (2-1) can be simplified to:

$$P_{cr} = \sqrt{P_E \cdot P_s} \tag{2-2}$$

Equation (2-2) provides an expression to estimate the critical load for bolted EBs in the UC, accounting for shear deformations.

2.3 Deformed Configuration

Under seismic conditions EBs along the perimeter on one side of the building are subject to maximum simultaneous axial compressive load and lateral displacement. Similarly to a column in a sway frame in which buckling loads are reduced due to second order effects the load carrying capacity of EBs reduces from the value calculated by (2-2) to some reduced value at a given lateral displacement (Buckle and Liu 1994).

Currently no explicit guidance is provided in most codes of practice such as the International Building Code (IBC 2003) and ASCE 7 (ASCE 2005) as to how $P_{cr}^{'}$ should be calculated. For example, Section 17.2.4.6 of ASCE 7-05 states, "each element of the isolation system shall be designed to be stable under the design vertical load where subjected to a horizontal displacement equal to the total maximum displacement", but does not provide means for this assessment. Similar provisions can be found in IBC 2003 as well as FEMA documents 356 (FEMA 2000) and 450 (FEMA 2004). However, the overlapping area method (OLAM), which appears in the *AASHTO Guide Specifications for Seismic Isolation Design*, has largely been adopted as the preferred way to determine $P_{cr}^{'}$.

2.3.1 Overlapping Area Method

As previously mentioned, the OLAM uses the ratio of the overlapping area between the top and bottom bearing end plates to the bonded rubber area to reduce the critical load in the UC (Eqn. 2-2) for a given lateral displacement. Using the OLAM, the reduced critical load, P_{cr}', is calculated according to (1-3). Figure 2.1 illustrates the overlapping area for three different lateral displacements including the UC (Fig. 2.1a), the DC when u is less than the bearing diameter, D (2.1b), and the DC when u is equal to D.

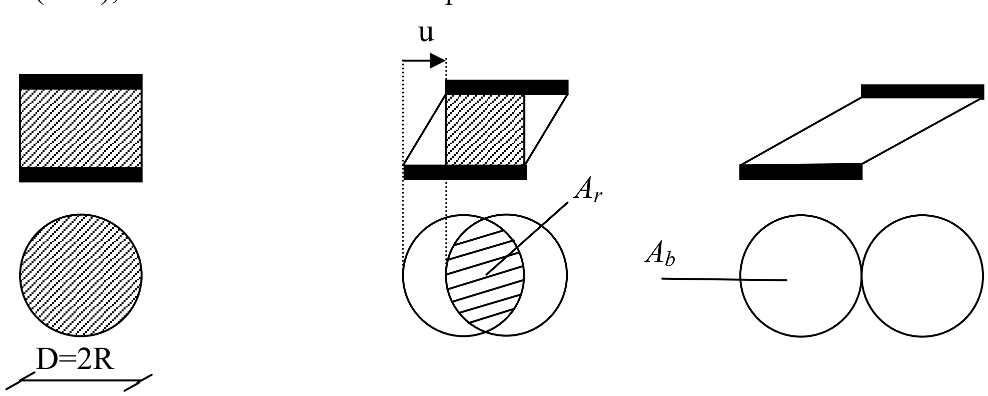

a) $u = 0$ b) $0 < u < D$ c) $u = D$

Figure 2.1 Illustration of the overlapping area method for a circular bearing

In Fig. 2.1a, the ratio A_r / A_b is unity, which from (2-3) results in $P_{cr}' = P_{cr}$. As u increases (Fig. 2.1b), the ratio A_r / A_b reduces and therefore P_{cr}' is reduced based on the percentage of bonded area that remains overlapping. At $u = D$, the OLAM predicts P_{cr}' to be zero as a result of no overlapping area $(A_r = 0)$. Outside of the notion of the "effective column" that exists in the overlapped area the OLAM has no rigorous theoretical basis in mechanics or otherwise to support the way the critical load is reduced.

To evaluate the OLAM, Buckle and Liu (1994) performed finite element analysis (FEA) and experimentally tested 18 square bearings at shear strains (γ, defined as u divided by the total thickness of rubber, T_r) of 50%-600%. The bearings were separated into six different sets based on shape factor (S=1.67 to 10), rubber layer thickness, and number of rubber layers. It should be noted that bearings with shape factors lower than 10 would typically be used for non-seismic bridge applications. Shape factors for EBs typically range from 10 to 30.

Of the six bearing sets only data for two (S=1.67 and S=2.5) were presented due to limitations on the axial compressive force that could be applied to the bearing. The maximum axial load was insufficient to observe critical behavior for the bearings with $S = 10$. A sample plot of the experimental data from Buckle and Liu (1994) for a bearing with S=2.5 is presented along with the prediction of P_{cr}' from the OLAM in Fig. 2.2.

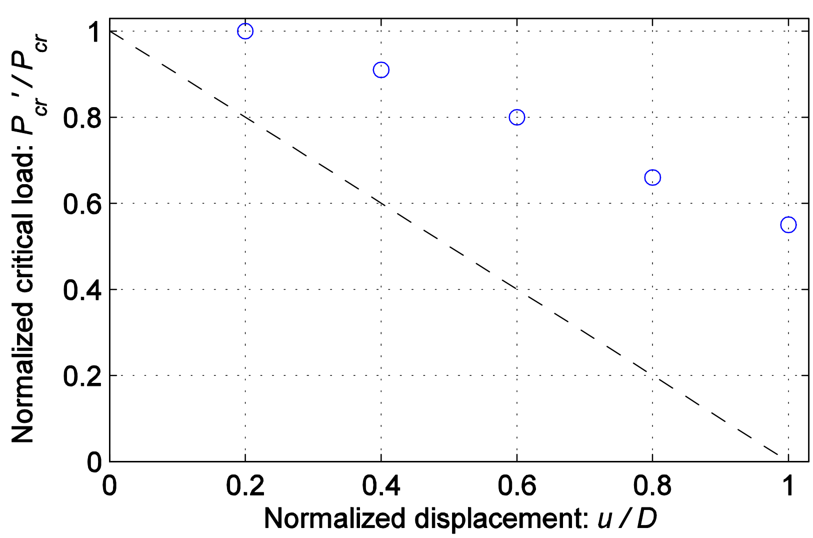

Figure 2.2 Data adapted from Buckle and Liu (1994) for a bearing with S=2.5

The horizontal axis in Fig. 2.2 represents the lateral displacement normalized by the bearing width (square) (u/D), whereas the vertical axis represents the reduced critical load P_{cr}' normalized by the critical load in the UC, P_{cr} (Eqn. 2-2). Figure 2.2 shows the OLAM conservatively estimates the reduced critical load (P_{cr}') for all displacement levels and at $u/D=1$, the OLAM predicts $P_{cr}'=0$ whereas the experimental data suggests $P_{cr}'/P_{cr}=0.55$ or 55% of the initial capacity remains at a displacement equal to the bearing width. Other bearings in this set, as well as the bearings with S=1.67 exhibited similar trends, though the OLAM was shown to be more conservative for bearings with S=1.67. Although conservative for the bearings shown in Buckle and Liu (1999), the OLAM is inconsistent and does not capture the experimentally observed trends in reduced critical load or provide an accurate estimate of P_{cr}' with increasing u.

Using data from Buckle and Liu (1994) (including some from the bearing set with S=5 that was not previously presented), Nagarajaiah and Ferrell (1999) conducted research investigating the stability of EBs in the laterally DC with varying axial load. The additional data (S=5) showed that the OLAM was unconservative for $u/D<0.45$. The results of Nagarajaiah and Ferrell once again showed that the OLAM does not agree well with experimental trends, that it is conservative in range of displacements for which stability would be assessed ($0.6 \le u/D \le 1.0$), and the conservatism of the OLAM decreases with increasing S.

2.3.2 Two-Spring Model

In an effort to improve the prediction of P_{cr}' over the estimations provided by the OLAM, Nagarajaiah and Ferrell (1999) examined a mechanical model initially developed by Koh and Kelly (1987) for its potential application to stability. This model, herein referred to as the two-spring model (TSM) was originally developed to predict the effect of axial load on the reduction in horizontal stiffness (K_H), decrease in height (v), and increase in damping. The TSM (shown in Fig. 2.3) consists of two rigid tee sections connected via frictionless rollers, a linear (K_s) and two rotational springs ($K_\theta/2$) connected to top and bottom end plates. The top is free to translate laterally whereas the bottom plate is fixed in all degrees of freedom. Under simultaneous axial load, P, and shear force, F, the model undergoes lateral displacement, u, producing shear deformation concentrated in the linear spring, s, and rotation concentrated in the two rotational springs, θ.

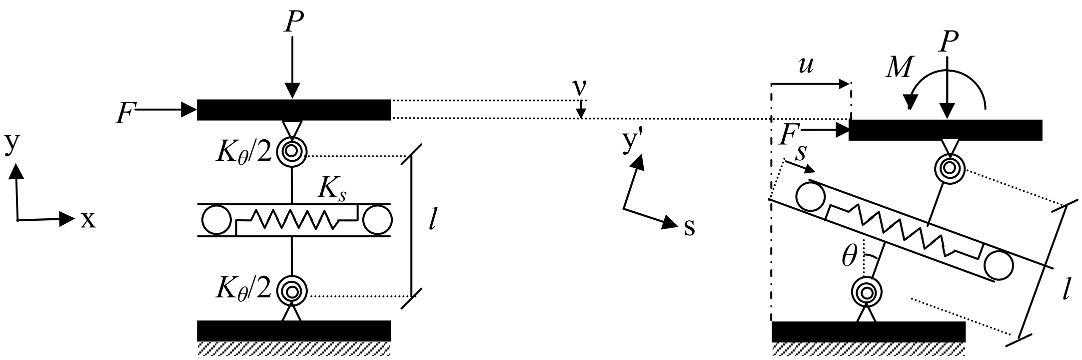

(a) Undeformed (service) **(b) Deformed (seismic)**

Figure 2.3 Two-spring model (adapted from Koh-Kelly 1987)

Though a simple model, the TSM has been shown by Koh and Kelly (1987) and others (Warn and Whittaker 2006) to accurately predict the reduction in height, v, with lateral displacement, the reduction in K_H and increase in mechanical damping with increasing axial load (P), and the reduction in the vertical stiffness with increasing lateral displacement (u).

By introducing nonlinear geometric and material properties (K_s and K_θ) Nagarajaiah and Ferrell (1999) were able to apply the TSM to the stability problem. Using equilibrium equations in the deformed configuration from this model and employing nonlinear spring properties (reducing the spring stiffnesses as some function of displacement) Nagarajaiah and Ferrell (1999) were able to show that the TSM could predict a reduction of P_{cr}' with increasing lateral displacement. Although these solutions were obtained numerically a closed-form solution was not presented. Moreover, the manner in which the spring stiffness properties varied with displacement is unable to be scrutinized as no rational or theoretical justification was provided. Other studies (Simo and Kelly 1984) suggests that instability observed in EBs is related to geometry, and not due to material instability or "softening." This argument is explored in further detail via numerical methods in Chapter 5 (Analytical Investigation).

CHAPTER 3

Finite Element Investigation

3.1 General

Finite element analysis (FEA) was employed to investigate the influence of lateral displacement on the load carrying capacity of low damping rubber (LDR) and lead-rubber (LR) bearings. Two three-dimensional half-space bearings were modeled, one LDR bearing with a shape factor (S) equal to 10 and one LR bearing with S equal to 12. The results of the FEA were used to generate numerical stability data which could be validated by experimental testing.

In addition to the 3D models, a number of two-dimensional models were developed for a parametric study to attempt to identify key geometric properties affecting the stability of LDR bearings.

3.2 Finite Element Analysis of Model LDR and LR Bearings

Three-dimensional FEA was performed using the commercially available finite element software package ABAQUS/Standard (DSSC 2008). A finite element model (FEM) of an annular LDR bearing that is circular in plan was generated. The LDR bearing has a shape factor (S) of 10, which is given by:

$$S = \frac{Loaded\ area}{Area\ free\ to\ bulge} = \frac{\pi(D_o - D_i)^2/4}{\pi\left(D_o + D_i\right)t_r} = \frac{D_o - D_i}{4t_r} \qquad (3\text{-}1)$$

for an annular bearing, where the subscripts o and i refer to the outer and inner diameters respectively, and t_r is the thickness of an individual rubber layer. A LR bearing model ($S = 12$) was constructed using the LDR model as a base through the addition of elements to represent the lead-core. Each model consists of two 25 mm steel end plates, 20 layers of 3 mm thick rubber with 19 intermediate steel shims (3 mm thick), and a 12 mm rubber cover. The LR bearing also includes a 30 mm diameter lead plug. Figure 3.1 shows details of the bearing, while Figs. 3.2a and 3.2b present a rendering of the LDR and LR bearing models, respectively. A detailed description of the modeling assumptions regarding element types, boundary conditions, and material properties is provided in subsequent sections.

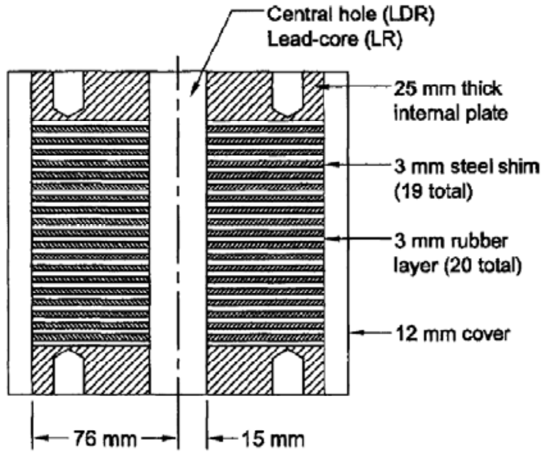

Figure 3.1 Bearing details

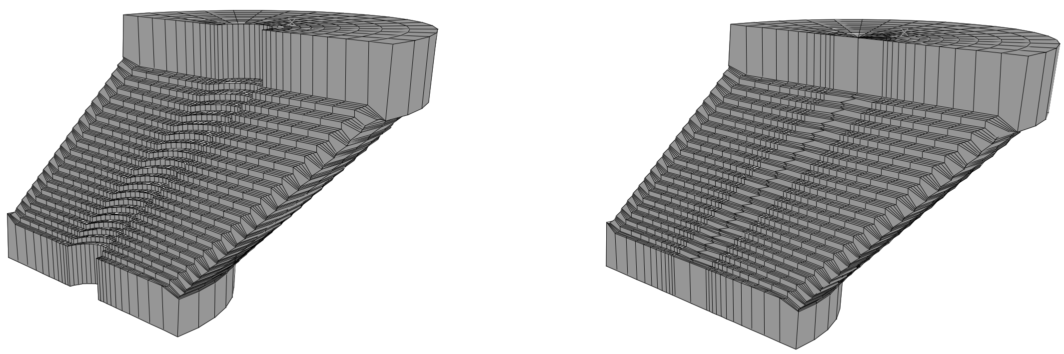

a) LDR FEM ($S = 10$) **b) LR FEM ($S = 12$)**

Figure 3.2 Finite element models

3.2.1 Model Description

The geometric and material properties of the FEM are based on bearings used for earthquake simulation testing (Warn and Whittaker 2006) which were also used in the experimental testing portion of this study. Exploiting symmetry, only half of the bearing was modeled in each case to maximize computational efficiency. Boundary conditions were chosen to mimic field bearings in which the bottom plate is fixed in all degrees of freedom and the top plate is fixed against rotation, but free to translate laterally and vertically. Because the bearings were modeled in half space the interior nodes not part of the central hole (which would normally be restrained by the other side of the bearing) were constrained to prevent motion perpendicular to the direction of displacement (i.e. bulging out of plane).

All elements of the LDR FEM used eight-noded C3D8 brick elements. These elements have first order formulations which have been shown to be more accurate than second order elements for materials that undergo large deformation (DSSC 2008).

More specifically, the rubber layers and cover were modeled with C3D8H elements that use a hybrid (or mixed) formulation in which pressure and displacement fields are independently specified. Due to the nearly incompressible behavior of rubber (Poisson ratio, $\upsilon \approx 0.5$) the two fields (displacement and pressure) are required to avoid the development of excessive hydrostatic stresses that could lead to volumetric locking (Bathe 1976, DSSC 2008). Steel layers were represented using C3D8I elements which include incompatible modes to avoid shear locking due to parasitic (non-existent) shear stresses. The lead core of the LR FEM was composed of a mix of C3D8H and six-noded, C3D6H (hybrid triangular prism) elements, where the hybrid formulation was once again used due to the high Poisson ratio of lead (Sivaraman 2000).

Following the selection of element types, material definitions were chosen for the steel and rubber. The steel material was modeled using a linear elastic, isotropic material with $\upsilon = 0.3$ and an elastic modulus, $E = 200$ GPa (29,000 ksi). Rubber, however, displays more complex behavior by comparison. Like most cross-linked polymers, the vulcanized rubber typically used in elastomeric bearings exhibits a behavior that is best characterized as nonlinear elastic, or hyperelastic. The Neo-Hookean material model, which is an extension of Hooke's Law for materials with large deformations was selected because the two parameters required are directly related to the engineering properties of the rubber, namely, the shear and bulk moduli. The strain energy potential takes the form:

$$U = C_{10}(\overline{I}_1 - 3) + \frac{1}{D_1}(J^{el} - 1)^2 \tag{3-2}$$

where U is the volumetric strain energy; C_{10} is defined as one-half the initial shear modulus; $\overline{I}_1$ is the first invariant of the deviatoric strain tensor; $1/D_1$ is one-half the initial bulk modulus; and J^{el} is the elastic volume ratio.

The effective shear modulus of 0.73 MPa (106 psi) was determined from shear testing in the experimental investigation (Chapter 4) and a value of 2,000 MPa (290 ksi) was assumed for the bulk modulus. The value of the bulk modulus was chosen based on typical values for lightly filled natural rubber. FEA performed by Warn and Whittaker (2006) showed that the vertical stiffness of the LDR bearing was insensitive to the exact value of the bulk modulus ($\pm 20\%$), but sensitive to the assumption of fully incompressible ($K \approx \infty$) behavior. Lead elements were modeled as elastic-perfectly plastic using material properties $\upsilon = 0.44$ and $E = 16$ GPa (2,320 ksi) from Guruswamy (2000). The uniaxial yield stress (σ_y) of 14.3 MPa (2,085 psi) was calculated using a relationship of the von Mises yield criterion and pure shear data in Warn and Whittaker (2006):

$$\tau_y = \frac{\sigma_y}{\sqrt{3}} \tag{3-3}$$

where τ_y is the yield stress in pure shear which was determined experimentally as 8.3 MPa (1,203 psi).

3.2.2 Convergence Study

To ensure the models used in this study had converged, three different meshes were generated for both the LDR and LR bearings. Models were run using eight nodes on Penn State's LION-XJ PC Cluster. LION-XJ uses an IBTM x3450 1U Rackmount Server with dual 3.0 GHz Intel Xeon E5472 quad-core processors and 64 GB of ECC RAM (HPC Group). A summary of the different meshes considered, along with the number of elements and wallclock times for each can be found in Table 3.1.

Table 3.1 Summary of models for convergence study

Mesh		No. Elements	Wallclock time (s)
LDR	Coarse	3,294	133
	Medium	19,998	1,486
	Fine	79,992	9,168
LR	Coarse	3,843	668
	Medium	21,816	3,728
	Fine	83,628	20,088

For the LDR bearing both horizontal stiffness (K_H) and critical displacement (u_{crit}) as illustrated in Fig. 3.3 were considered as convergence criteria. The horizontal stiffness is simply the slope of the shear force – lateral displacement curve and the critical displacement is the point of neutral equilibrium (stability limit) which is found when $K_H = 0$.

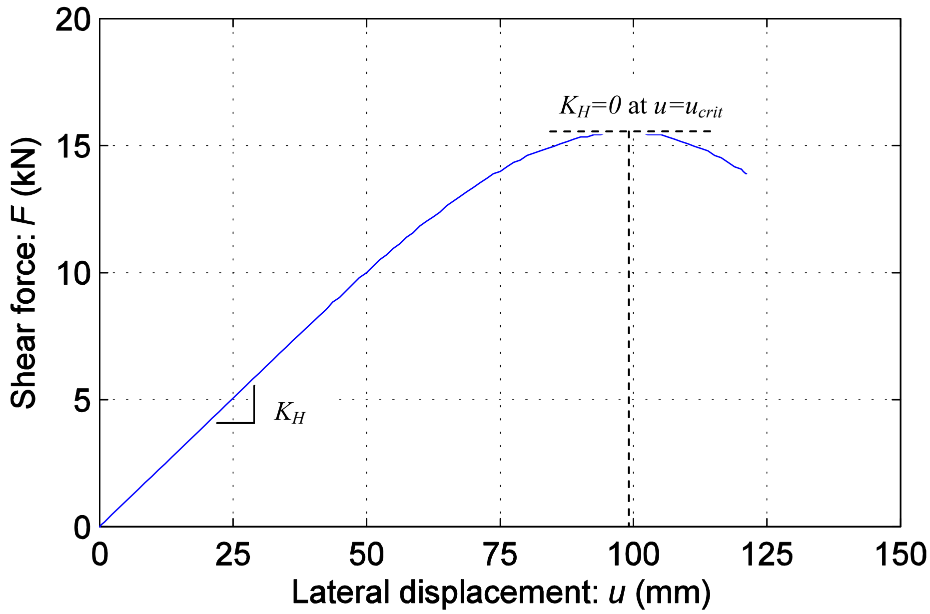

Figure 3.3 Illustration of convergence criteria for LDR bearing

The results of the convergence study for the LDR model is shown in Figs. 3.4, 3.5 and 3.6.

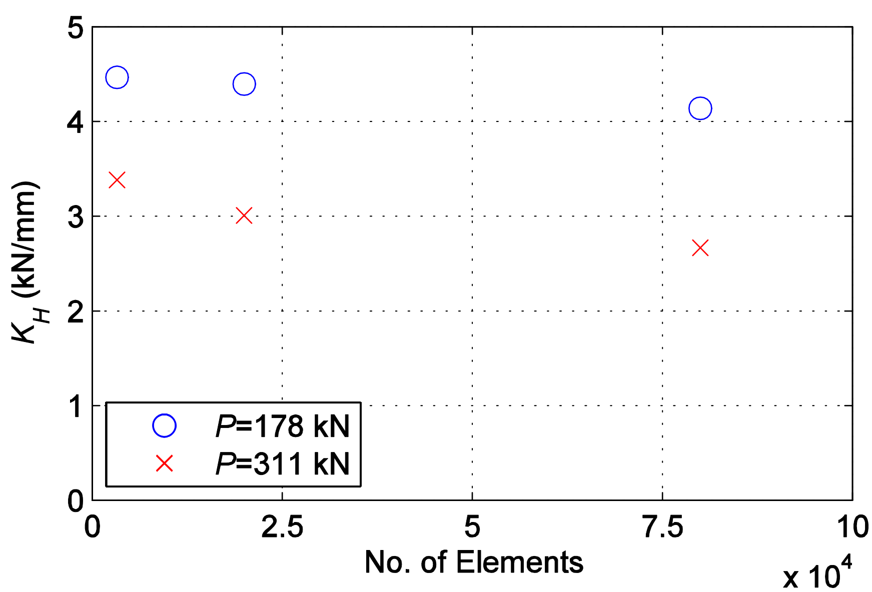

Figure 3.4 Convergence of LDR bearing using K_H for criteria

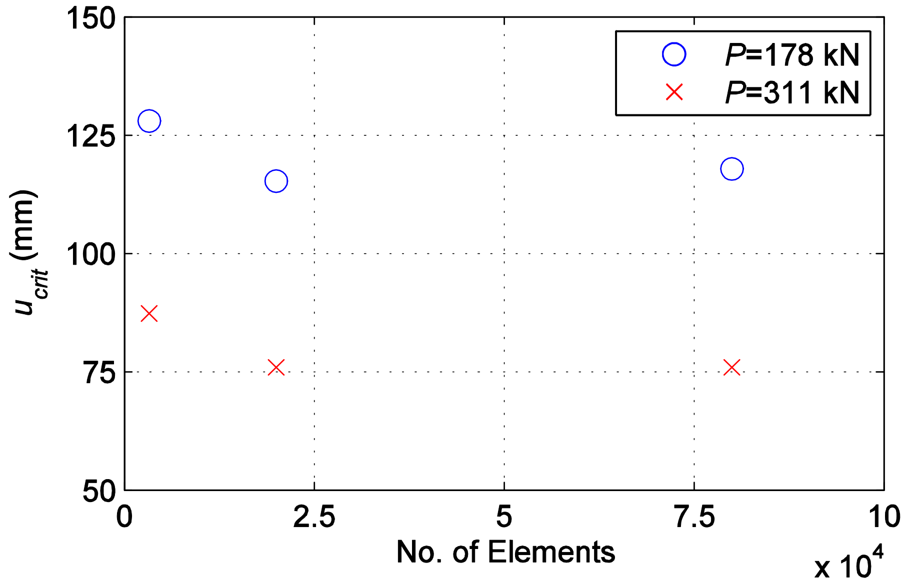

Figure 3.5 Convergence of LDR bearing using u_{crit} for criteria

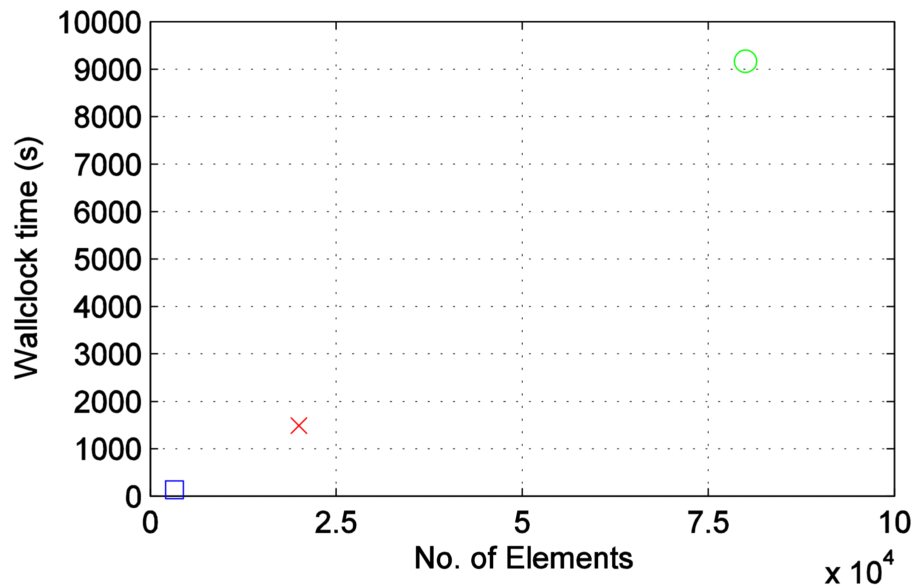

Figure 3.6 Wallclock time variation with number of elements for the LDR bearing

For both criteria (K_H and u_{crit}) the medium mesh provided less deviation from the fine mesh than the coarse mesh. Table 3.2 shows the numerical difference in results of the convergence study between the coarse and fine mesh, and medium and fine mesh.

Table 3.2 Percentage difference of convergence criteria for the LDR bearing

Criteria/Meshes	Coarse to Fine	Medium to Fine
$K_{H,P=178kN}$	8.0%	6.2%
$K_{H,P=311kN}$	27.1%	13.0%
$u_{crit,P=178kN}$	8.6%	2.2%
$u_{crit,P=311kN}$	15.1%	0.0%

While ideal convergence for K_H was not achieved (in which the difference between the results from the medium and fine meshes were kept under 10%) it was decided that the medium mesh still provided a reasonable approximation of the horizontal stiffness, but more importantly converged for the main parameter of interest in this study, u_{crit}. Since a significant number of analyses needed to be run, wallclock times were also strongly considered as a dominating factor in the decision. To provide a balance between acceptable error and efficiency the medium mesh was selected for this study.

For the LR bearing the characteristic strength (Q_d), which is defined as the zero-displacement force intercept from one fully reversed cycle, (as illustrated in Fig. 3.7) was added to the convergence criteria.

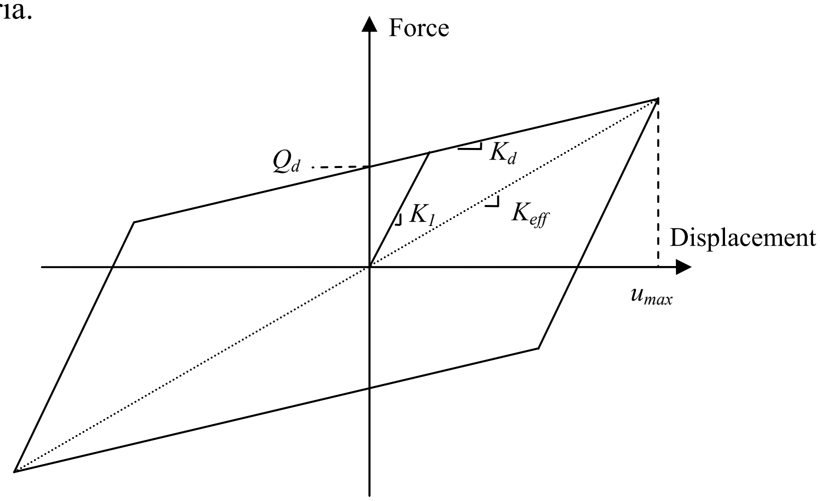

Figure 3.7 Idealized behavior of an LR bearing

Results of the convergence study for the LR bearing are presented in Figs. 3.8, 3.9 and 3.10.

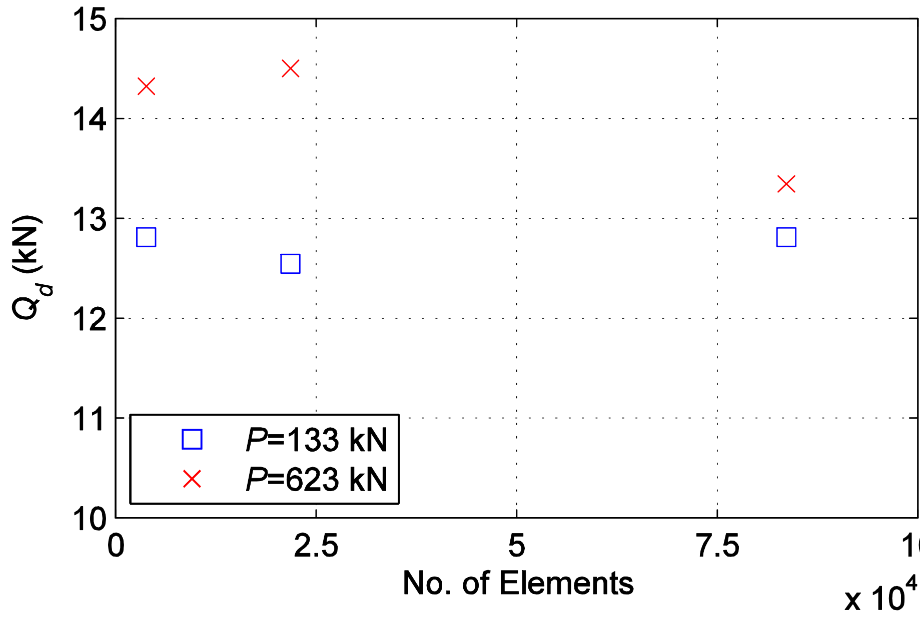

Figure 3.8 Convergence of LR bearing using Q_d for criteria

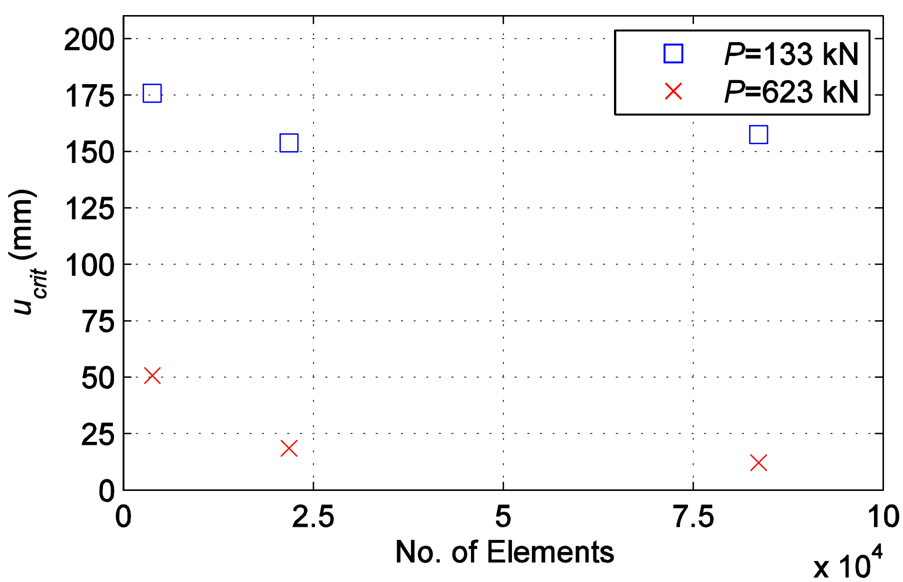

Figure 3.9 Convergence of LR bearing using u_{crit} for criteria

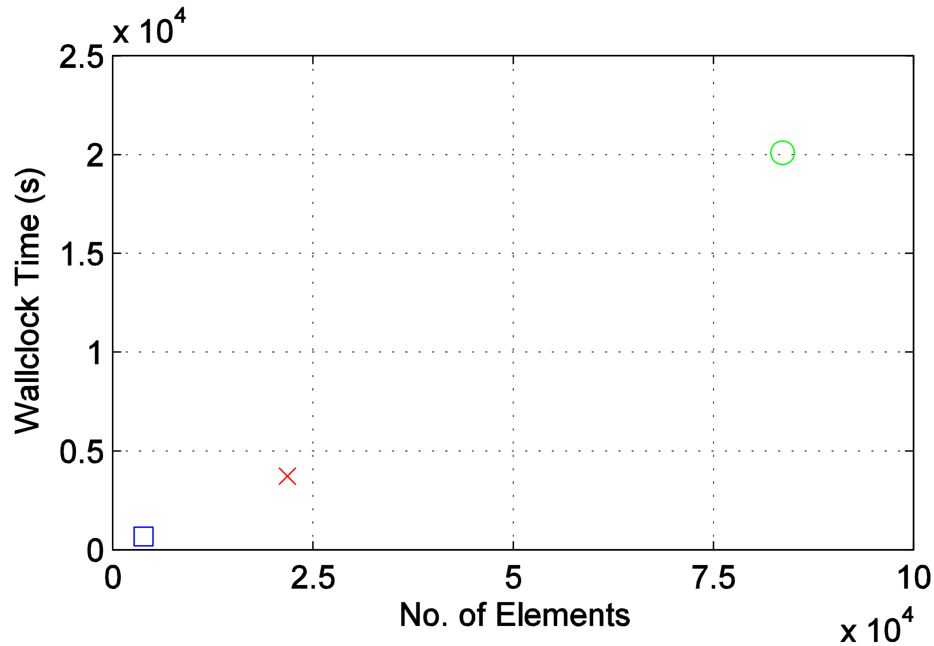

Figure 3.10 Wallclock time variation with number of elements for the LR bearing

Again u_{crit} was considered to be the principal interest for convergence. The results for the convergence of u_{crit} was similar to that of the LDR bearing, where the medium mesh provided a more accurate result (using the fine mesh as the 'true' solution) than the coarse mesh and within a reasonable tolerance of error. The characteristic strength appeared to be irregularly sensitive to mesh density, with the medium mesh providing a more inaccurate result (when compared to the fine mesh) than the coarse mesh. Table 3.2 shows the numerical difference in results of the convergence study between the coarse and fine mesh, and medium and fine mesh.

Table 3.3 Percentage difference of convergence criteria for the LR bearing

Criteria/Meshes	Coarse to Fine	Medium to Fine
$Q_{d,P=133kN}$	0.0%	2.1%
$Q_{d,P=623kN}$	7.3%	8.7%
$u_{crit,P=133kN}$	11.5%	2.4%
$u_{crit,P=623kN}$	316.7%	52.1%

Though the percentage difference is quite large under 623 kN of axial load the actual difference in the critical displacement is only 6 mm (0.25 in) and is a marked improvement over the coarse mesh. For similar reasons to the convergence study for the LDR bearing the medium mesh was used in a trade off of time and accuracy.

3.2.3 Analysis Using Constant Axial Force

The FEMs were analyzed under constant axial load and monotonically increasing lateral displacement to identify points of neutral equilibrium (identified in this study as the stability limit). Each analysis was carried out in two steps. First, the bearing was compressed axially to a specified load. Then, the bearing was sheared to a specified lateral displacement. This analysis was repeated for a wide range of axial loads (0 to 0.93 P_{cr}).

The force-displacement results generated from the aforementioned steps were then used to determine the point of neutral equilibrium ($\partial F / \partial u = K_H$ =0) which corresponds to a reduced the critical displacement, u_{crit} . The axial load corresponding to u_{crit} was identified as the critical load capacity at the given displacement (or the reduced critical load), $P_{cr}^{'}$. Neutral equilibrium represents a condition for which the change in the total potential energy (or its second variation) is zero (Tauchert 1974). Graphically this is observed when the shear force passes through a maximum under constant axial load. Similarly for a constant shear force, the critical point is reached when $\partial P / \partial u = 0$ as will be utilized in subsequent sections. Figure 3.11 shows sample FEA results for the LDR bearing under three axial load levels, demonstrating the influence of axial load on shear force and illustrating the critical point.

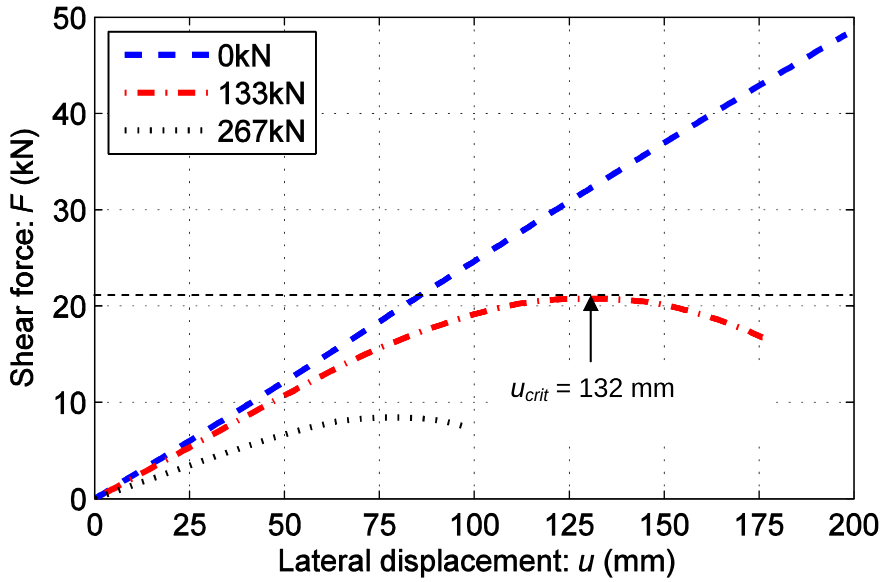

Figure 3.11 Force-displacement results from LDR FEM for varying axial load

The results presented in Fig. 3.11 show that for zero axial load no critical point is observed up to a lateral displacement of 200 mm (7.9 in) and there exists a linear relationship between shear force and displacement per the Neo-Hookean material model assigned to the rubber layers. As the axial load was increased from 0 kN to 133 kN (30 kips) and then 267 kN (60 kips) several results seen in previous studies (Koh and Kelly 1987, Nagarajaiah and Ferrell 1999) were observed. These results include:

1. As axial load increases the horizontal stiffness decreases.
2. As axial load increases the maximum shear force decreases and occurs at a smaller displacement.

Moreover, Fig. 3.11 illustrates an example of a point of neutral equilibrium. When the LDR bearing is subject to 133 kN of axial load the shear force passes through a maximum (shown by the horizontal dashed line) of 22 kN (4.9 kips) at a displacement (u_{crit}) of 132 mm (5.2 in). The displacement and axial load at which $K_H = 0$ are critical points used to define stability in the deformed configuration.

3.2.4 Analysis Using Constant Displacement

Due to eventual constraints with the experimental test setup, a constant displacement method (CDM) used in other studies (Buckle and Liu 1994, Nagarajaiah and Ferrell 1999, Buckle et. al 2002) was adopted for experimental testing. For verification purposes, FEA was performed using the constant displacement method for both the LDR and LR models to:

1. Determine the impact of loading history on the point of neutral equilibrium.
2. Facilitate direct comparison of FE and experimental results.

The CDM operates under the principle that critical displacements represent a unique equilibrium configuration at which there is a single shear force and axial load combination corresponding to a point of neutral equilibrium. Unlike constant force methods the CDM requires an indirect determination of critical points. The analysis is carried out by first shearing the bearing to a specified displacement level. Then, the axial load is monotonically increased and shear force is monitored as it tends to zero. Shear force-axial load curves are generated from the collected data and lines of constant shear or axial load are drawn. Figure 3.12 shows sample results of the FEA using the constant displacement method.

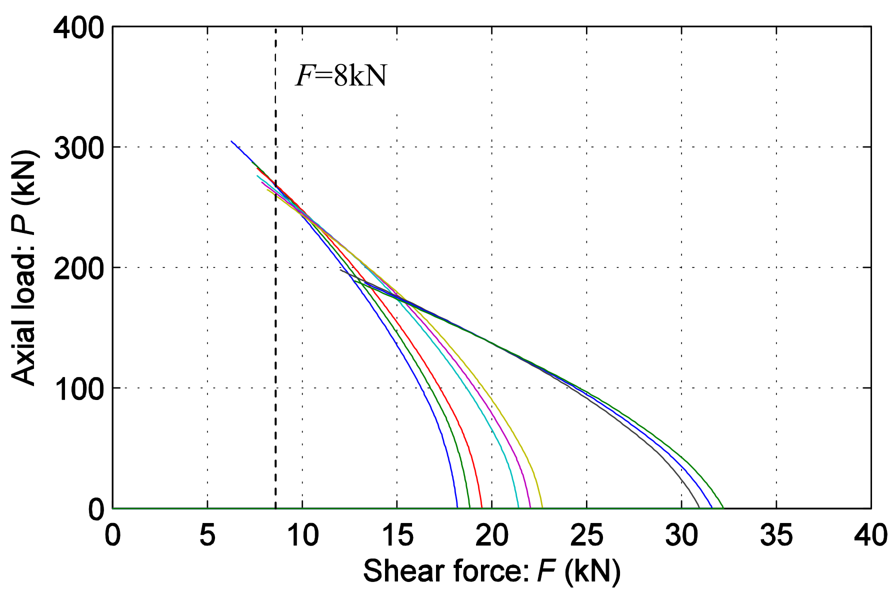

Figure 3.12 Sample FEA *P-F* curves using the CDM

Points where the lines of constant shear force (F=8kN for example) intersect the shear force-axial load curves are replotted on a force-displacement graph (Fig. 3.13).

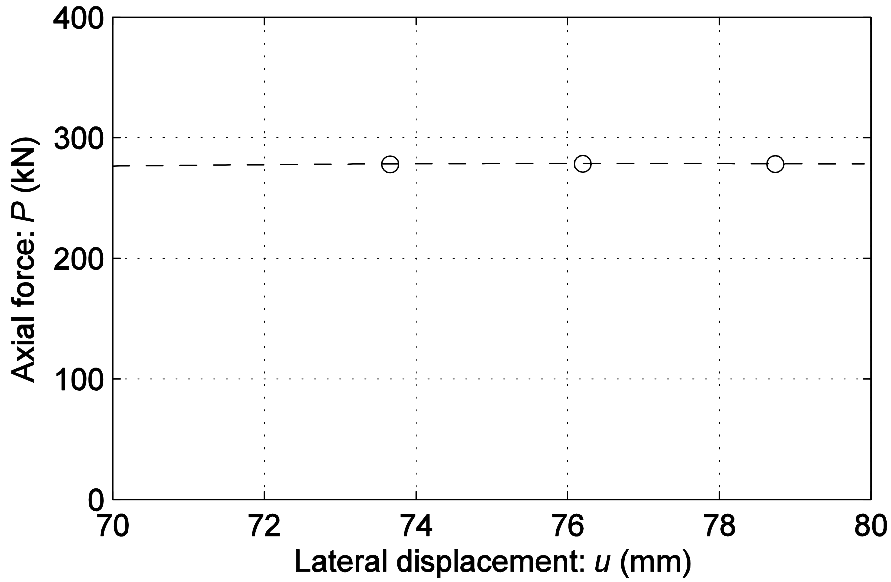

Figure 3.13 Sample FEA *P-u* curves using the CDM

The second point in Fig. 3.13 corresponds very nearly to the maximum axial force value, indicating the critical point for F=8kN is at approximately u_{crit} = 76 mm and $P_{cr}^{'}$ = 278 kN. Though only a finite number of analyses can be run and the true maximum cannot be determined exactly, FEA provides the ability to specify displacements and calculate forces at a resolution not possible in experimentation. As a result, curve fitting is unnecessary using this method in FEA, though it will be required in the experimental investigation. The critical point is found where the shear force passes through a maximum under constant axial load (or axial load passes through a maximum under constant shear force). This process is revisited and illustrated further in section 4.3.3 for the experimental phase.

3.2.5 Results

The theoretical critical load for the LDR bearing, P_{cr}, was calculated to be 341 kN (76 kips). This was found using a modified version of Haringx theory (Eqn. 2-2) in which P_s (the term that accounts for shear deformation) was increased by a factor of 1.2 to account for the apparent increase in the shear stiffness observed both in the FEA and in Warn and Whittaker (2006). Traditionally, for LDR bearings the effective shear stiffness, K_{eff}, is given by:

$$K_{eff} = \frac{G_{eff} A_b}{T_r} = \frac{P_s}{l} \tag{3-4}$$

where T_r is the total thickness of the rubber layers and l is the bearing height. Because A_b and T_r are fixed values, the observed twenty percent increase in shear stiffness is simulated by premultiplying the effective shear modulus (referred heretofore simply as G) by 1.2. However, since the vertical and rotational properties were found to be largely unaffected by the cover, the unmodified value of the shear modulus (determined experimentally as 0.73 MPa [106 psi]) is used in the calculation of P_E (the term more closely related to the rotational behavior of the bearing). Using the same modified effective shear modulus for both terms would lead to an overestimation of P_{cr}. As a result of the aforementioned (2-2) becomes:

$$P_{cr} = \sqrt{P_s \cdot P_E} = \sqrt{(G \cdot A_s) \cdot P_E} \rightarrow \sqrt{(1.2G \cdot A_s) \cdot P_E} \tag{3-5}$$

with the Euler buckling load defined as $P_E = \pi^2 (EI)_{eff} / l^2$ where E is the rotational modulus, for a annular bearings (from Constantinou et al. 1992):

$$E = \left[(1 / \left(6GS^2 F \right) + 4 / \left(3K \right) \right]^{-1} / 3 \tag{3-6}$$

where $S = 10.2$ is the shape factor; $K = 2000\,MPa$ is the bulk modulus; $F = 0.69$ is a geometric factor to account for the compression behavior due to the presence of the central hole; and $I = 26.5 \cdot 10^{-6} m^4$ is the second moment of area. Effective values of GA_s and EI in which those terms are multiplied by the ratio of the bearing height to total rubber layer thickness are used to account for the fact that the steel does not deform in the composite system. When values are input for each of the variables, (3-5) leads to the following calculation:

$$P_{cr} = \sqrt{(1.2G \cdot A_s) \cdot \frac{\pi^2 (EI)}{l^2}} \tag{3-6}$$

$$P_{cr} = 341\,kN \tag{3-7}$$

Figure 3.14 presents the results of the FEA for the LDR bearing using the constant axial force method with axial loads ranging from 0 to 0.93 P_{cr}.

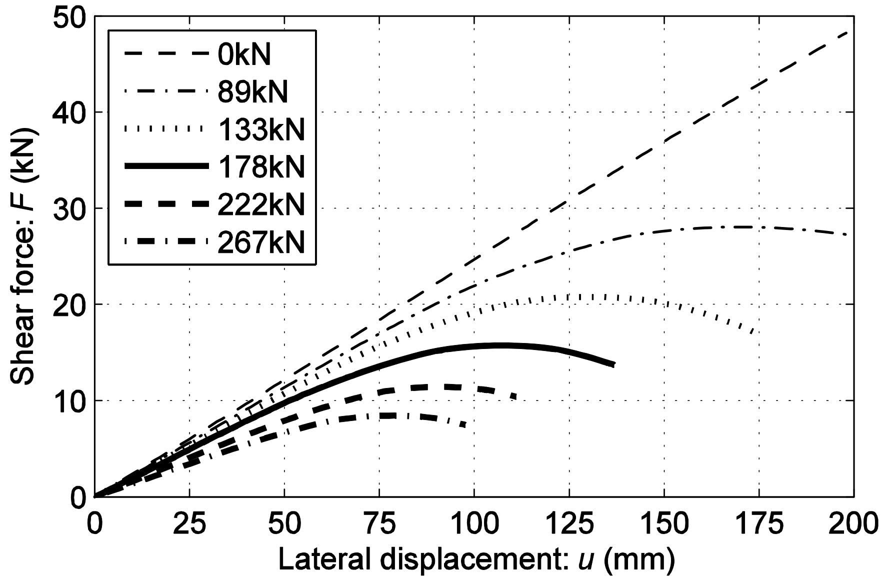

Figure 3.14 LDR force-displacement results, $S = 10$

The results presented in Fig. 3.14 show that the LDR FEM predicts a reduction in the critical displacement (u_{crit}) for increasing axial loads. For example, under 89 kN of axial load, u_{crit} occurs at 172 mm, but as the axial load is increased to 178 kN the displacement at which neutral equilibrium is reached decreases to $u_{crit} = 109$ mm.

For the LR bearing the theoretical critical load (P_{cr}) was again determined using (2-2), however, as with the LDR bearing, P_s needed to be modified to account for the effect of the cover. In the case of LR bearings the effective horizontal stiffness is given by:

$$K_{eff} = \frac{Q_d}{u_{\max}} + K_d = \frac{P_s}{l} \tag{3-8}$$

where $K_d = GA_b / T_r$ is the second slope stiffness (see Fig. 3.7). Because the lead core is assumed to behave independently of the additional cover only the K_d term is modified for the calculation of P_s. The result is:

$$K_{eff} = \frac{Q_d}{u_{\max}} + \frac{(1.2G)A_b}{T_r} = \frac{P_s}{l} \tag{3-9}$$

Again, the unmodified value of the shear modulus is used for the calculation P_E while (3-9) is used for calculating P_s. Based on these assumptions and using experimentally determined values of Q_d and $u_{\max}$, P_{cr} for the LR bearing was found to be 693 kN (156 kips):

$$P_s = K_{eff} \cdot l = \left(\frac{Q_d}{u_{\max}} + \frac{(1.2G)A}{T_r} \right) l = \left(\frac{5.9kN}{0.06m} + \frac{(1.2 \cdot 0.73MPa) \cdot 0.017m^2}{0.06m} \right) \cdot 0.117m = 40.5\,kN \tag{3-10}$$

$$P_E = \frac{\pi^2 (321MPa \cdot 26.2 \cdot 10^{-6} m^4) \left(\frac{0.117m}{0.06m} \right)}{(0.117m)^2} = 11{,}962\,kN \tag{3-11}$$

$$P_{cr} = \sqrt{(40.5kN) \cdot (11{,}851kN)} = 693kN \tag{3-12}$$

Figure 3.15 presents the results of the constant axial force method results for the LDR bearing.

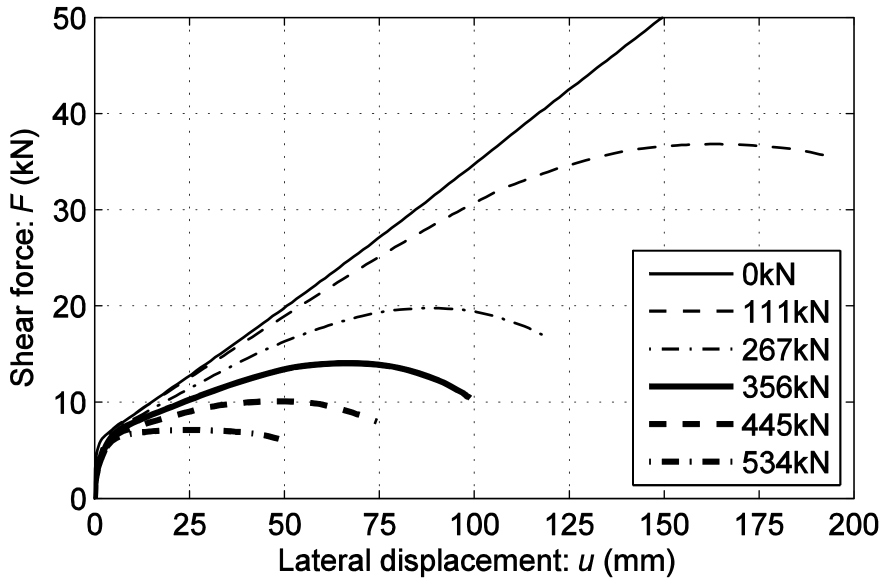

Figure 3.15 LR bearing force-displacement results, $S = 12$

The reduced critical loads (P_{cr}'), shear force (F), and corresponding displacements (u_{crit}) obtained for each axial load level (each curve) from Figs. 3.14 and 3.15 were used to generate numerical stability data that are plotted in Fig. 3.16.

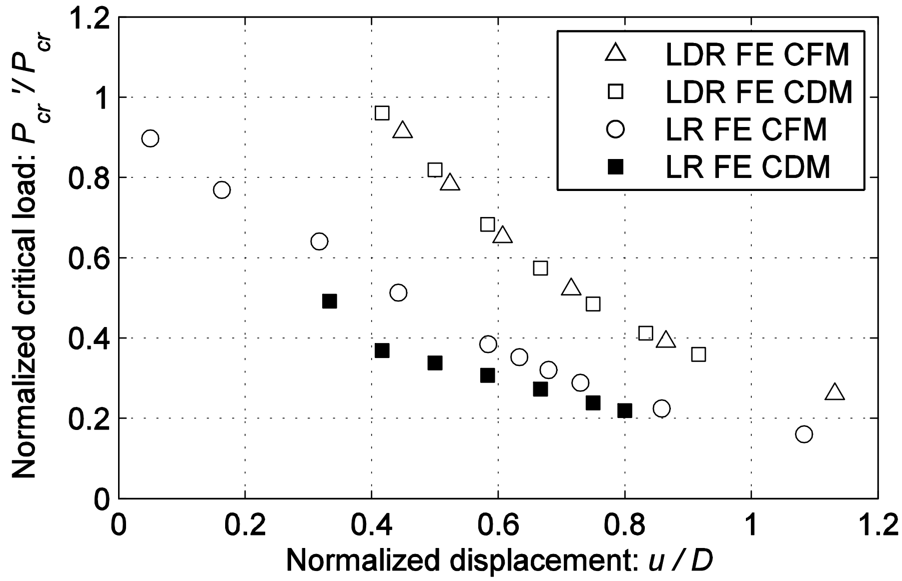

Figure 3.16 Normalized stability results of FEA

Figure 3.16 presents normalized results of the FEA for both the LDR and LR bearing models using the constant axial force method (CFM) and constant displacement method (CDM) where the horizontal axis is lateral displacement, u, normalized by the bearing diameter, D, and the vertical axis is the reduced critical load, P_{cr}', normalized by the critical load in the undeformed configuration, P_{cr}. At a displacement equal to the bearing diameter ($u / D = 1$) the bearings have on the order of $0.19P_{cr}$ and $0.30P_{cr}$ for the LR and LDR bearings respectively.

3.3 Discussion of Model LDR and LR Bearing FEA Results

The stability data shown in Fig. 3.16 provides several useful observations. For LDR bearings it was confirmed that the constant axial force and constant displacement methods yield the same critical load behavior, suggesting a path independency of the critical point to loading. Conversely, the FEA results for the LR bearing only agreed moderately well, having the largest disparity in the region between $u / D = 0.2$ and $u / D = 0.6$ suggesting the reduced critical load is path dependent.

The discrepancy between the two methods for the LR bearing can be explained in small part due to the inexactness of the CDM, but the degree of discrepancy suggests that the nonlinear behavior of the lead core is the cause. A consequence of this result is that due to the random nature of seismic loading (which will fall somewhere between the two methods in terms of how loading is applied) the CDM, which was shown to be the more conservative of the two methods, should be used in practice unless otherwise justified.

Another observation from Fig. 3.14 is that the critical load capacity reduces at a faster rate for the LR bearing than the LDR bearing. This suggests that the LR bearing will be most effective for the stability limit state when the design displacements are small relative to bearing diameter and that the benefit of a increasing P_{cr} in absolute terms through the introduction of the lead core are going to be offset to some degree by the quicker reduction.

Lastly, the capacity of both bearing types is significantly greater than zero at $u/D=1$ once again suggesting the overlapping area method (OLAM) is excessively conservative at large normalized displacements. However, due to the aforementioned rate of reduction of critical load the OLAM will tend to be less conservative for LR bearings than LDR bearings.

3.4 Parametric Study of LDR Strip Bearings

In addition to the three-dimensional analysis of the LDR and LR bearings a two-dimensional parametric study was performed to determine whether certain geometric properties had an effect on the reduced critical load of LDR bearings.

The first step of the parametric study was the development of several prototype bearings to be modeled using finite elements. In choosing the bearings to be studied there is implicit bias on the properties to be studied. Initially the use of Latin Hypercube Sampling (a random sampling technique) was examined to avoid this bias, but the result was the generation of models without enough in common that trends would be unable to be discerned. The decision was made to constrain the study to three typically specified bearing properties: the shape factor (S), the bearing width (b), and the thickness of rubber layers (t_r). The shape factor for strip bearings is defined as:

$$S=\frac{b}{2t_r} \tag{3-13}$$

and can therefore be thought of a composite of the latter two properties.

To allow direct comparisons to be made the bearings were chosen to have constant values of one or more of the three properties, while the other(s) were free to vary. A summary of the models is shown in Table 3.4. Additional properties such as the number of rubber layers (n), bearing height (h), shim thickness (t_s) and critical load at zero displacement (P_{cr}) are also presented.

Table 3.4 Model bearings used in the parametric study

Model Name	S	b (mm)	t_r (mm)	n	h (mm)	t_s (mm)	P_{cr} (kN)	No. Elements	Wallclock time[1] (s)
b15tr250n20	30.00	381	6.4	20	187.3	3.2	487.1	21240	760
b15tr375n20	20.00	381	9.5	20	250.8	3.2	216.5	10620	461
b15tr500n20	15.00	381	12.7	20	314.3	3.2	121.7	8496	364
b15tr625n20	12.00	381	15.9	20	377.8	3.2	77.9	9440	389
b10tr375n20	13.33	254	9.5	20	250.8	3.2	64.1	11328	728
b12tr375n20	16.00	305	9.5	20	250.8	3.2	110.8	18880	542
b20tr375n20	26.67	508	9.5	20	250.8	3.2	513.1	3360	602
b15tr375n5	20.00	381	9.5	5	60.3	3.2	865.9	6960	225
b15tr375n10	20.00	381	9.5	10	123.8	3.2	432.9	10560	440
b15tr375n15	20.00	381	9.5	15	187.3	3.2	288.6	14160	654
b15tr1500n20	5.00	381	38.1	20	822.3	3.2	13.5	3540	167
b375tr375n20	5.00	95	9.5	20	250.8	3.2	3.4	3540	112
b15tr3000n20	2.50	381	76.2	20	1584.3	3.2	3.4	1770	97
b187tr375n20	2.50	48	9.5	20	250.8	3.2	0.4	1770	105

[1]The wallclock time presented is associated with the time it took to run each model using the aforementioned LION-XJ cluster in Penn State's High Performance Computer network using 8 cpus in parallel.

3.4.1 Model Description

In the interest of computational efficiency and to allow more analyses to be conducted the aforementioned bearings were modeled as two-dimensional strip bearings using the commercial finite element software package ABAQUS. Because the bearings were being modeled as strips a plane strain condition was enforced. The rubber layers were modeled with CPE4H elements, where the "C" refers to continuum, "PE" refers to plane strain, "4" denotes number of nodes, and "H" once again denotes the use of a hybrid formulation of pressure and displacement for the reasons previously discussed. Similarly, CPE4I elements were used to model the steel shims.

Each rubber layer was discretized into two layers for a better approximation of the bulging that takes place under load while not dramatically increasing the computational cost. Ideally the aspect ratio would have been kept to 1, however, several models had issues with excessive deformations. To address this problem the elements were "preshaped" such that they were tall and narrow when the bearing was undeformed, but as the bearing was displaced the elements would tend to become square and were prevented from becoming excessively squat. Figure 3.17 illustrates the concept of preshaping elements.

a) Original (undeformed) **b) Original (deformed)** **c) Preshaped (undeformed)** **d) Preshaped (deformed)**

Figure 3.17 Illustration of preshaped elements

In cases where a given model could be run with elements having aspect ratios of 1 or 3 the resulting critical points varied by less than 10%. This suggests a reasonable insensitivity to the aspect ratio and supports the use of an aspect ratio of 3 where required. For consistency the aspect ratio was held constant at 3 for rubber elements in all models. The decision to maintain this aspect ratio determined the number of elements (and as a result the mesh density). Figure 3.18 shows a sample strip bearing model.

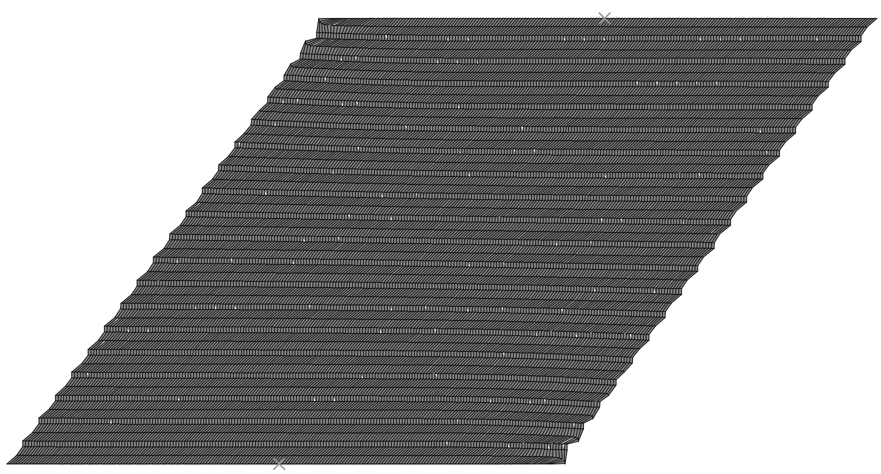

Figure 3.18 Sample strip bearing model (b12tr375n20)

3.4.2 Results

Both rubber and steel elements made use of the same material models used in the three-dimensional FEA. Boundary conditions mirrored those described in section 3.2.1. The same loading procedure in which the bearing was subjected to a constant axial load and then sheared was used to find critical points. Each model was run at axial loads ranging from 0.1 P_{cr} to 0.9 P_{cr} though results were not able to be achieved in every case. Figure 3.19 shows a sample of shear force – displacement curves for one of the bearing models.

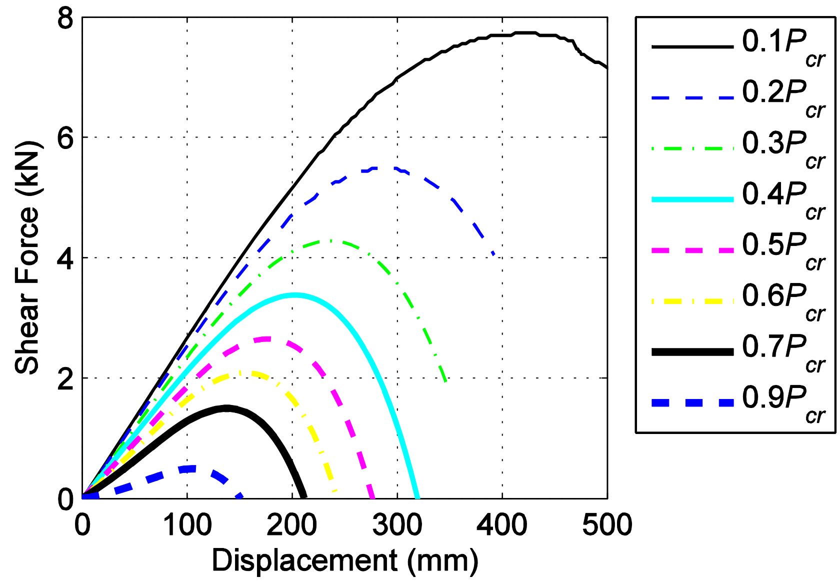

Figure 3.19 Shear force – displacement curves for model b12tr375n20

Having obtained the above plot the stability curve shown in Fig. 3.20 could be constructed. For reference the predictions of the OLAM are plotted along with the FE results.

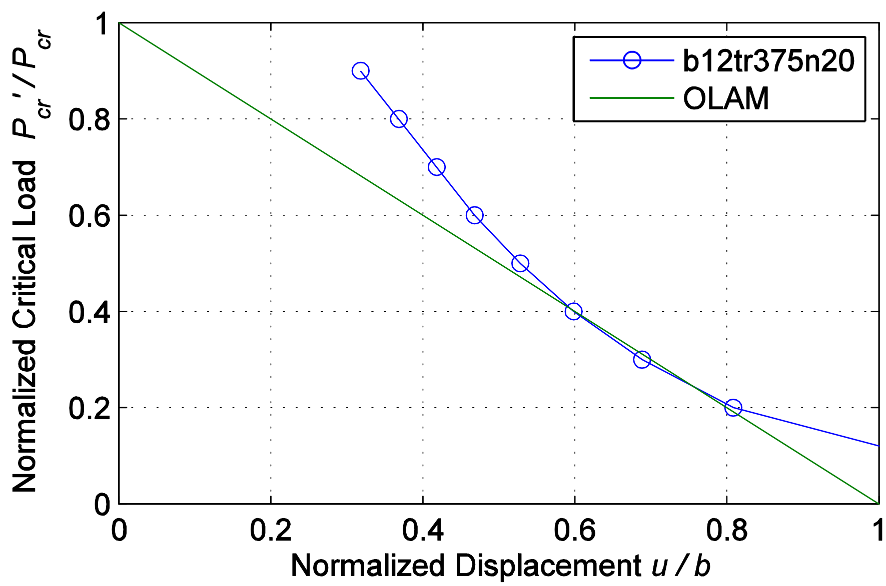

Figure 3.20 Stability curve for model b12tr375n20

The expected result of diminishing capacity with increasing displacement is observed. This process is repeated for each model bearing to generate individual stability curves. Several of the models (such as the aforementioned) would not run for the full range of axial loads, however, in most cases there were enough data points to sufficiently describe the variation of capacity with displacement (even if only in certain regions, for example, between u/b =0.6 to 1.0). The stability curves for the remaining model bearings appear in the Appendix A.

Figures 3.21, 3.22, and 3.23 are a series of plots that show the variation of normalized critical load capacity ($P_{cr}^{'}/P_{cr}$) with shape factor (S), bearing width (b), and rubber layer thickness (t_r) respectively.

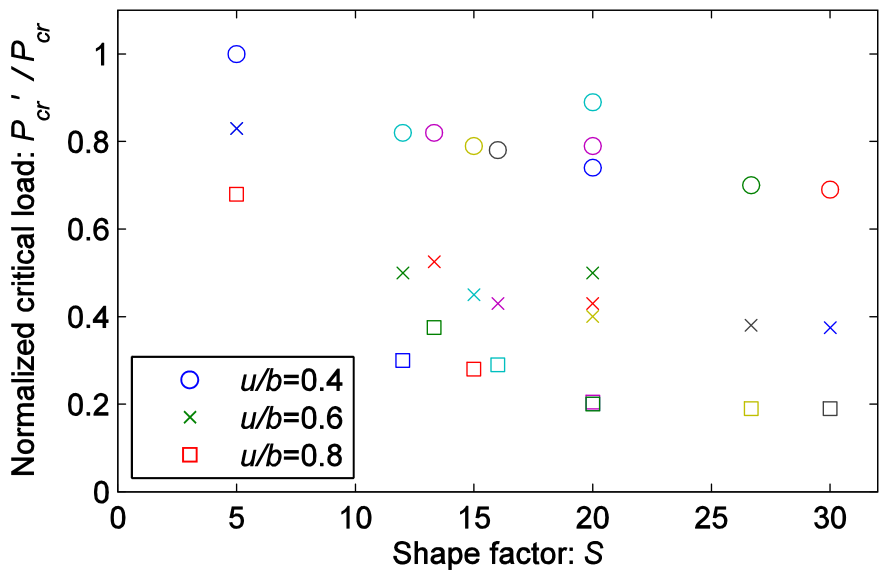

Figure 3.21 Variation of normalized critical load capacity with shape factor

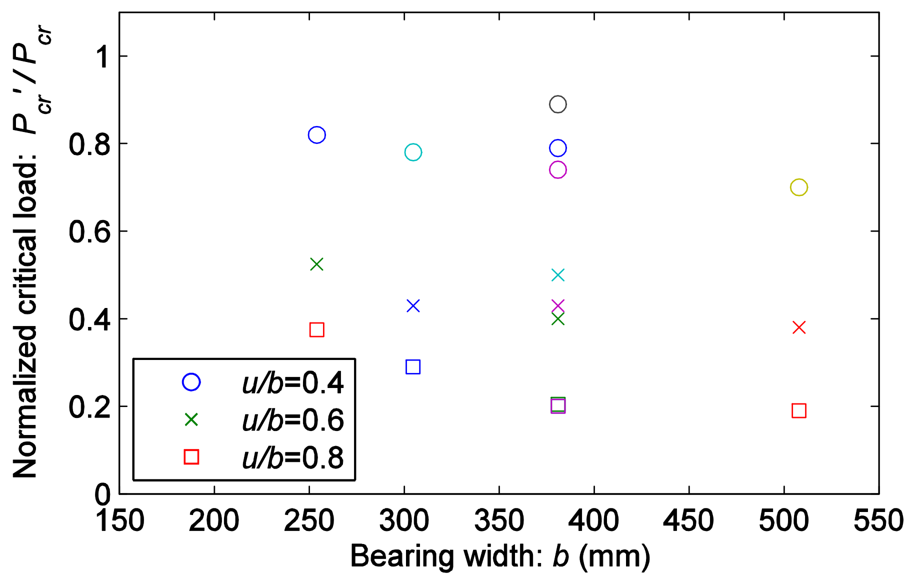

Figure 3.22 Variation of normalized critical load capacity with bearing width

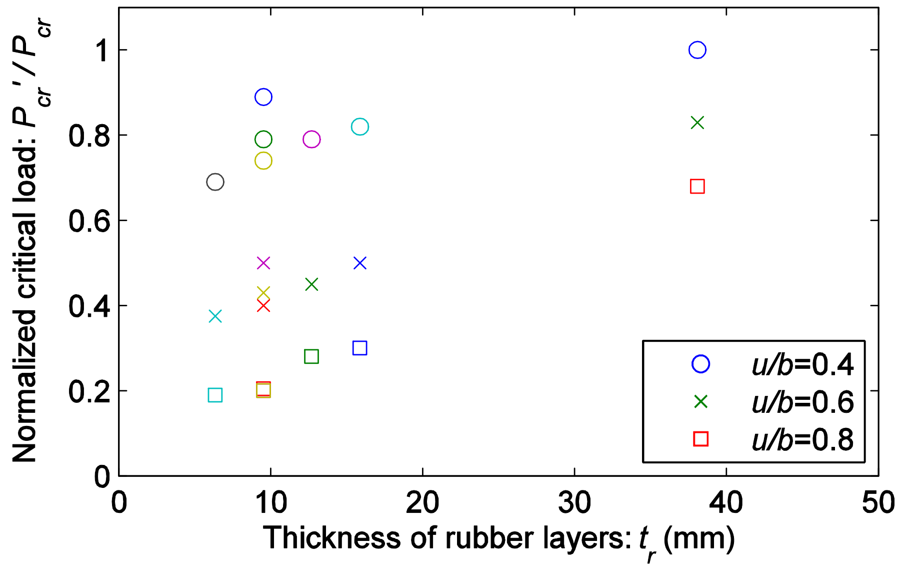

Figure 3.23 Variation of normalized critical load capacity with rubber layer thickness

To compare the predictions of the overlapping area method with the parametric FEA results a series of plots comprising Figs. 3.24, 3.25, and 3.26 were generated for normalized displacement levels of 0.4, 0.6, and 0.8.

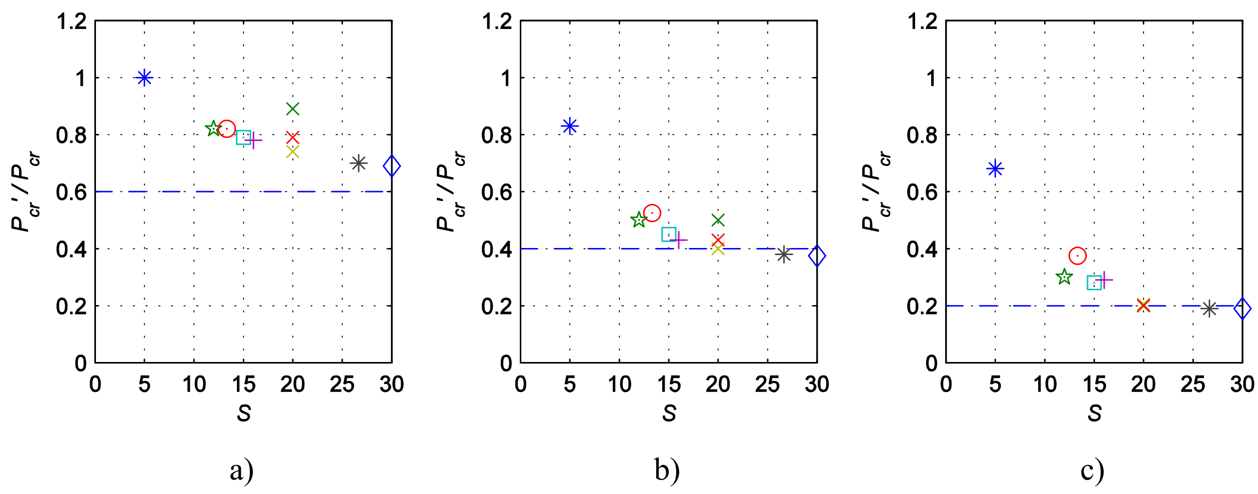

Figure 3.24 Comparison of critical load predictions from FE and OLAM (dashed) for shape factor for a) $u/b = 0.4$ b) $u/b = 0.6$ c) $u/b = 0.8$

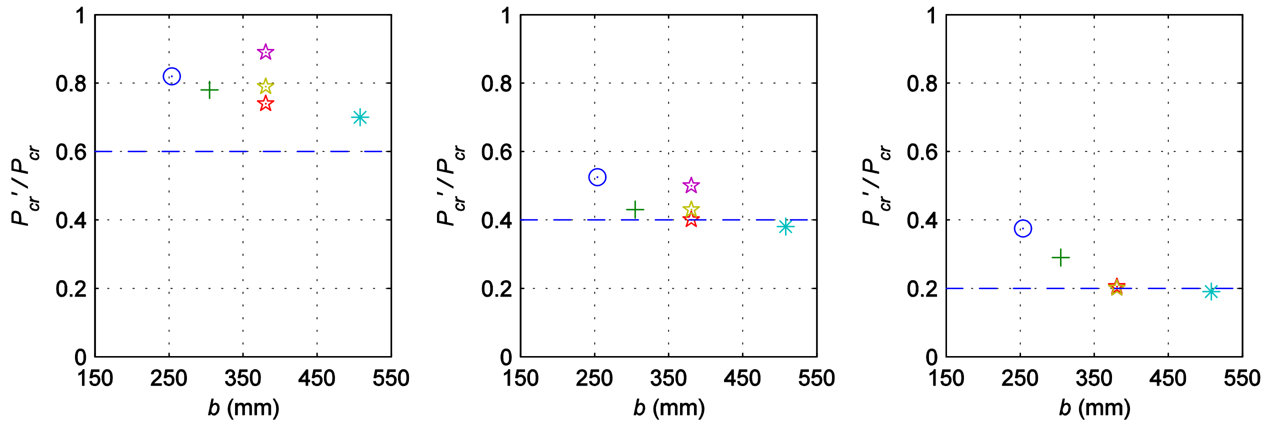

Figure 3.25 Comparison of critical load predictions from FE and OLAM (dashed) for bearing width for a) $u/b = 0.4$ b) $u/b = 0.6$ c) $u/b = 0.8$

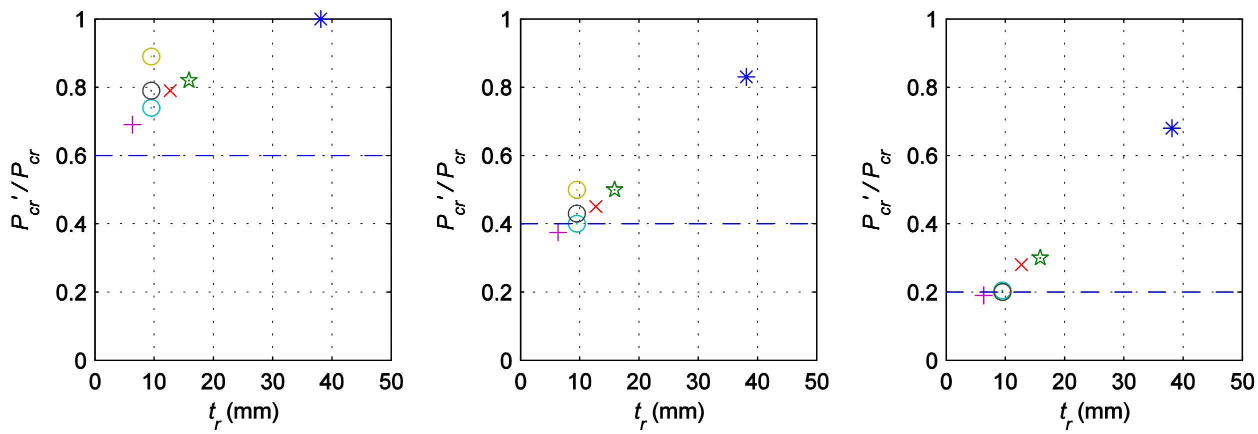

Figure 3.26 Comparison of critical load predictions from FE and OLAM (dashed) for rubber layer thickness for a) $u/b = 0.4$ b) $u/b = 0.6$ c) $u/b = 0.8$

3.5 Discussion of Parametric Study Results

Shape Factor (S)

Figure 3.21 shows that at a given displacement level bearings with larger shape factors, in general, will have lower reduced critical load capacity (in normalized terms). The trend becomes more pronounced as the displacement level increases (at $u/b = 0.4$ the trend is nearly linear, at $u/b = 0.6$ and $u/b = 0.8$ it is closer to an exponential decay).

In addition, as evidenced from Fig. 3.24 the FEA results indicate that the OLAM is conservative for all shape factors at $u/b = 0.4$ and that the degree to which it is conservative decreases with increasing shape factor. The latter result has been observed in experimental studies (Buckle and Liu 1994, Buckle et al. 2002), but due to the limited sample size of experimental data lacked confidence that the trend would be observed for other bearings. At $u / b = 0.6$ and $u / b = 0.8$ the OLAM does not consistently provide conservative predictions of capacity suggesting the OLAM might lead to unconservative estimates of P_{cr}' for large (20-30) shape factors which are typical of seismic isolation bearings.

Bearing Width (b)

Figure 3.22 shows that for a given rubber layer thickness and shape factor, an increase in bearing width results in a lower normalized capacity at a given displacement level. This is counterintuitive at first glance because a bearing that is more squat would be expected to have a higher capacity (and they do). However, when normalized, the wider bearings have a smaller percent of P_{cr} remaining by comparison to narrower bearings. This means that even though the absolute capacity is higher for a wider bearing, in terms of the undeformed capacity we see a faster rate of reduction in the critical load with increasing displacement. This implies that the benefit of increasing the bearing width that could result from the OLAM would have diminishing marginal returns that are unaccounted for at present.

Rubber Layer Thickness (t_r)

Figure 3.23 shows that for a given bearing width and shape factor, an increase in the rubber layer thickness results in an increase in normalized capacity at a given displacement level. The trends are inversely related to the shape factor as would be expected by the definition of shape factor for strip bearings where $S = b / 2t_r$. However, the rubber layer thickness tends to have greater physical meaning and similarly to the bearing width one may intuitively arrive at the incorrect result. By increasing the rubber layer thickness the normalized capacity appears to increase despite increased bulging. It should however be reiterated that this is only looking into the vertical load stability of the bearings and increasing the rubber layer thickness could negatively impact other limit states, for example, vertical stiffness.

3.6 Application of Parametric Study Results to the OLAM

To improve the predictions of the OLAM and highlight a potential method for making it generally applicable for elastomeric bearings the results of parametric study were examined to develop a modified version of the OLAM. It has been shown that P_{cr}' is a function of bearing geometry (width, thickness of rubber layers, shape factor). Because the shape factor takes into account both bearing width (diameter) and the thickness of individual rubber layers it was chosen as the basis for the modification factor.

For simplicity of integration with the current method, which for strip bearings predicts:

$$P_{cr}' = P_{cr} \cdot \left(1 - \frac{u}{b}\right) \tag{3-14}$$

a linear shift by a factor, λ ,was implemented. The result of this modification is Eqn. (3-15).

$$P_{cr}' = P_{cr} \cdot \left(1 - \frac{u}{b} + \lambda\right) \le P_{cr} \tag{3-15}$$

where λ is given by:

$$\lambda = \left\{ \begin{matrix} 0.4 - 0.045 \cdot (S - 5) \\ 0.04 - 0.008 \cdot (S - 15) \end{matrix} \quad for \quad \begin{matrix} S < 15 \\ S \ge 15 \end{matrix} \right\} \tag{3-16}$$

The modification factor, λ , represents the dependence of the minimum residual between the OLAM predictions and the parametric results on the shape factor of the bearing. Because λ gives rise to the potential of Eqn. (3-15) to predict the undesirable situation in which reduced critical load exceeds the undeformed capacity it carries the additional stipulation that P_{cr}' is limited to P_{cr}. To illustrate the derivation of λ Fig. 3.27 shows the variation of minimum residual with shape factor.

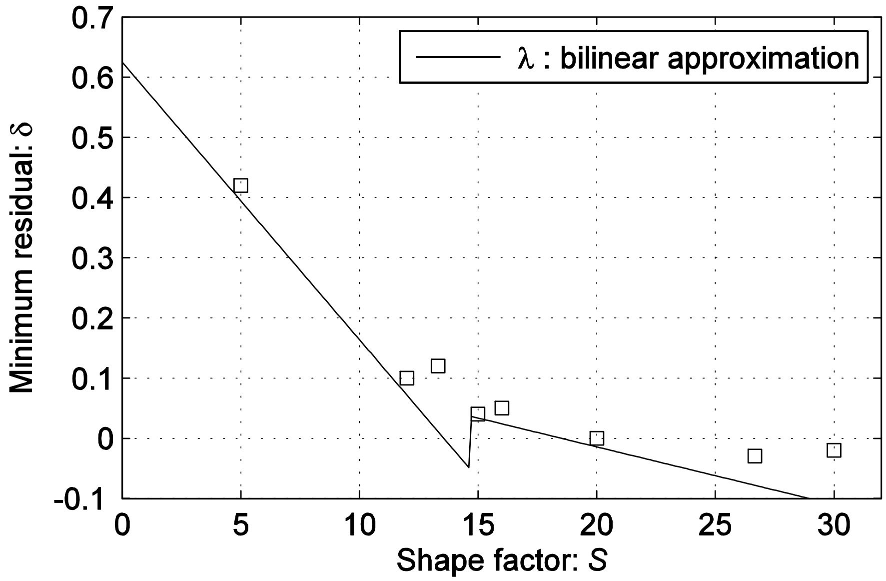

Figure 3.27 Variation of minimum residual between OLAM and FEA with shape factor

In lieu of fitting λ to a smooth, but complex function using curve fitting techniques it was approximated by a bilinear function in which a convenient (by inspection of Fig. 3.27) shape factor of 15 was chosen as the distinctive value.

Figure 3.28 shows the result of the modified overlapping area method (mOLAM) based on Eqns. (3-15) and (3-16) for several shape factors.

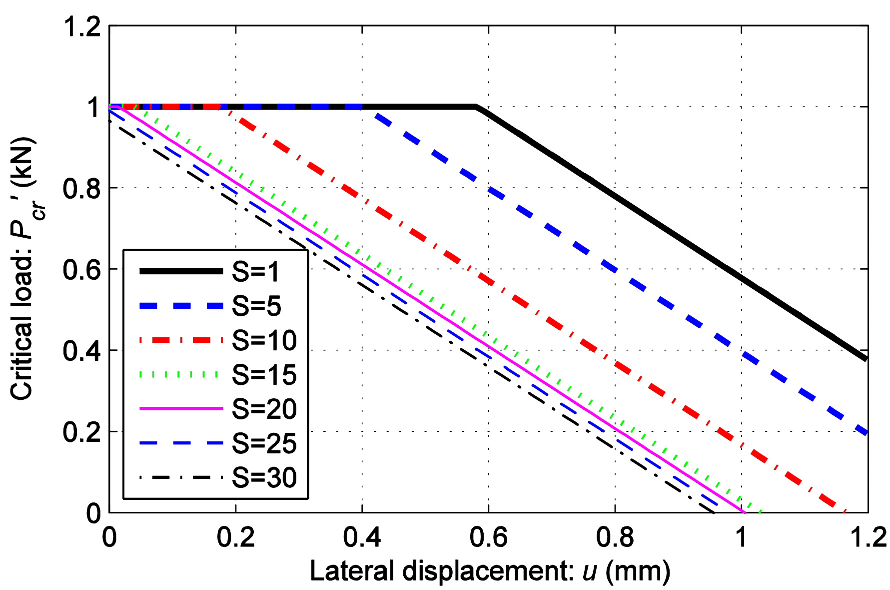

Figure 3.28 Illustration of mOLAM predictions

Figures 3.29, 3.30, 3.31, and 3.32 show a comparison of the mOLAM with the OLAM predictions for the b15tr1500n20 (S = 5), b15tr625n20 (S = 12), b12tr375n20 (S = 16), and b15tr250n20 (S = 30) bearing respectively.

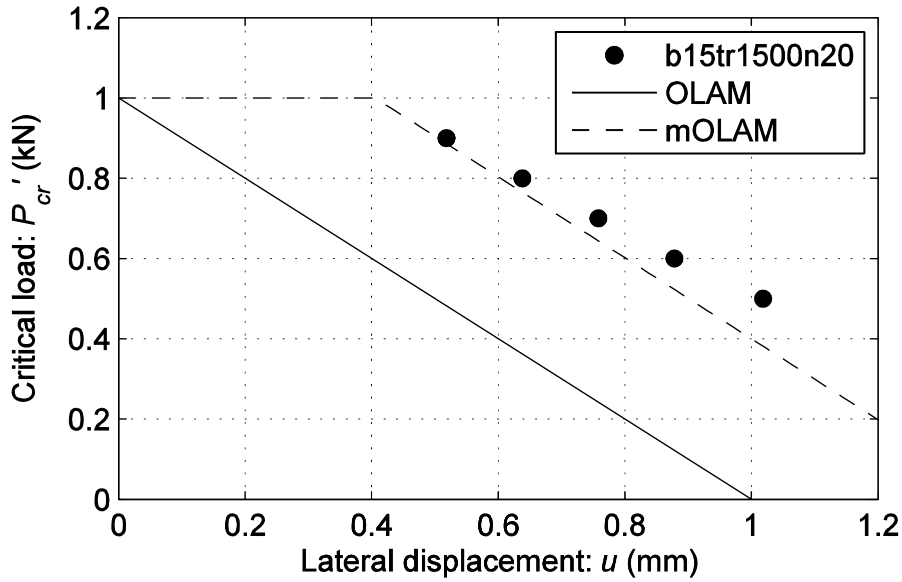

Figure 3.29 Comparison of mOLAM and OLAM for b15tr1500n20

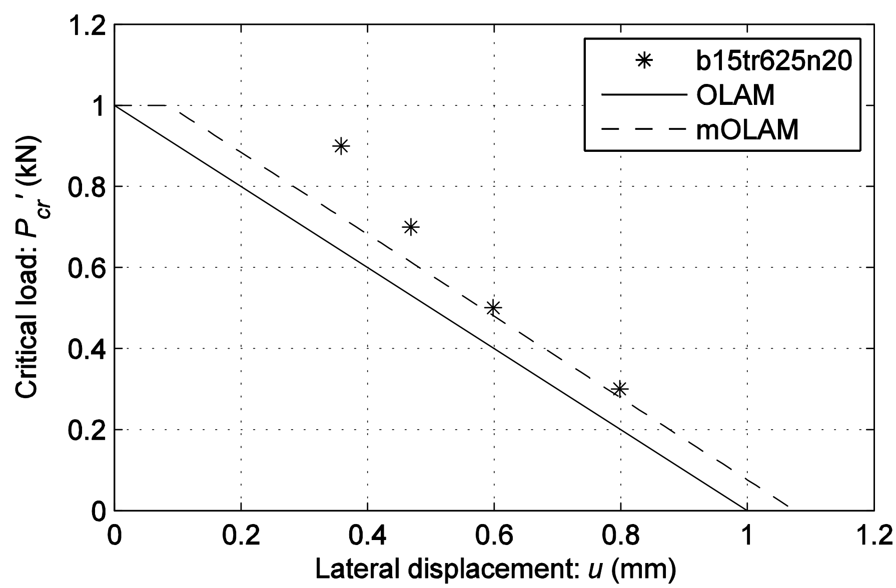

Figure 3.30 Comparison of mOLAM and OLAM for b15tr625n20

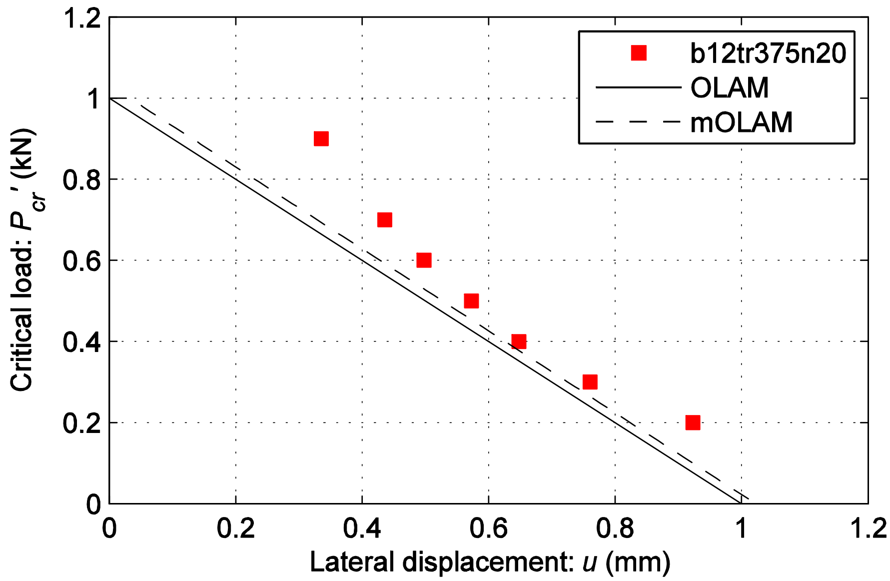

Figure 3.31 Comparison of mOLAM and OLAM for b12tr375n20

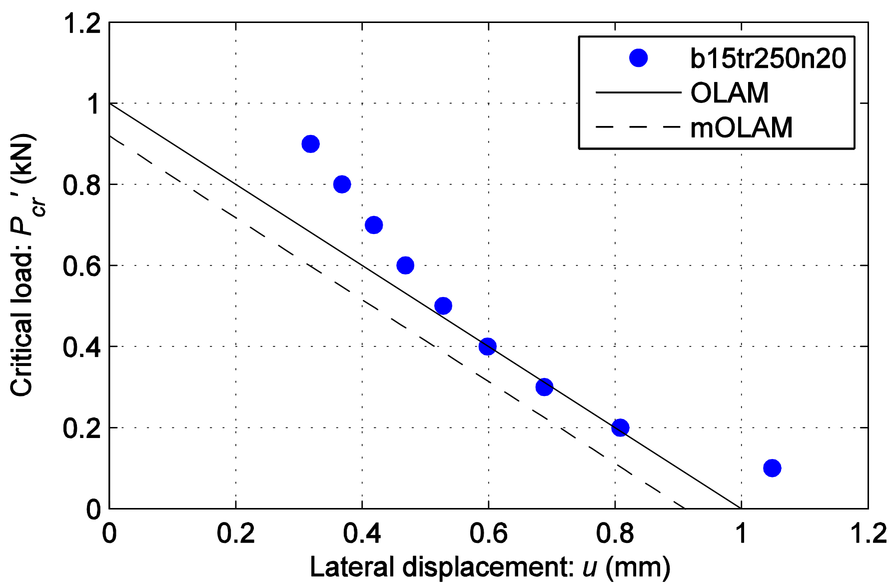

Figure 3.32 Comparison of mOLAM and OLAM for b15tr250n20

As shown in Figs. 3.29 to 3.32 the mOLAM provides conservative, but significantly better agreement to the predicted critical load from FEA. Although a mechanics based modification or formulation is preferred the λ factor proposed here retains the simplicity of the overlapping area calculation for design while improving its predictive capability. It should further be noted that the relationships derived are based on a limited number (14) of two-dimensional FEA strip bearings and might not be generally applicable as the results have not been verified experimentally.

CHAPTER 4

Experimental Investigation

4.1 General

The stability of low damping rubber (LDR) and lead-rubber (LR) bearings was investigated through experimental testing of bearing specimens described in Chapter 3 (S =10.2 and 12.7 respectively). The objective of the experimental investigation was collecting data to facilitate development of stability curves that will be used to validate the finite element (Chapter 3) and numerical (Chapter 5) results.

Testing was conducted at the State University of New York (SUNY) at Buffalo's Structural Engineering and Earthquake Simulation Laboratory (SEESL) using two bearing testing machines. The small bearing testing machine (SBTM), which permitted cycling of a bearing under constant axial load, was used to characterize the bearings (determine mechanical properties such as horizontal stiffness and effective shear modulus). Due to the limited axial load capacity of the SBTM, the large bearing testing machine (LBTM) was used for stability testing.

The stability tests consisted of laterally displacing the bearing to a specified level then monotonically increasing the axial load while monitoring the reduction in shear force. These tests generated equilibrium trajectories from which critical loads could be determined for a given lateral displacement. In addition to studying the behavior (mechanical and stability) of the two bearing types independently, the influence of the lead core on stability was also investigated by comparison to the LDR results. Bearing characterization testing in which the bearing was subjected to cyclic lateral displacements under constant axial load was used to determine mechanical properties.

4.2 Bearing Characterization

4.2.1 Setup and Instrumentation

Bearing characterization was conducted using the SBTM to determine mechanical properties (K_{eff}, G_{eff}) to be used in the FEA. A schematic and photograph of the apparatus are shown in Figs. 4.1a and 4.1b respectively. The SBTM has been designed to apply simultaneous axial load and lateral displacement.

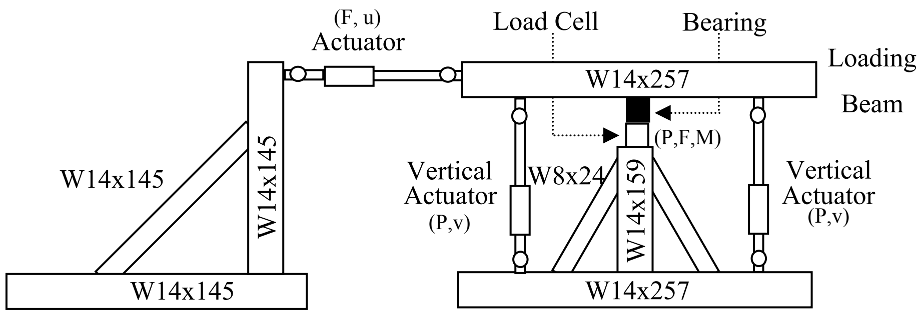

a) Schematic

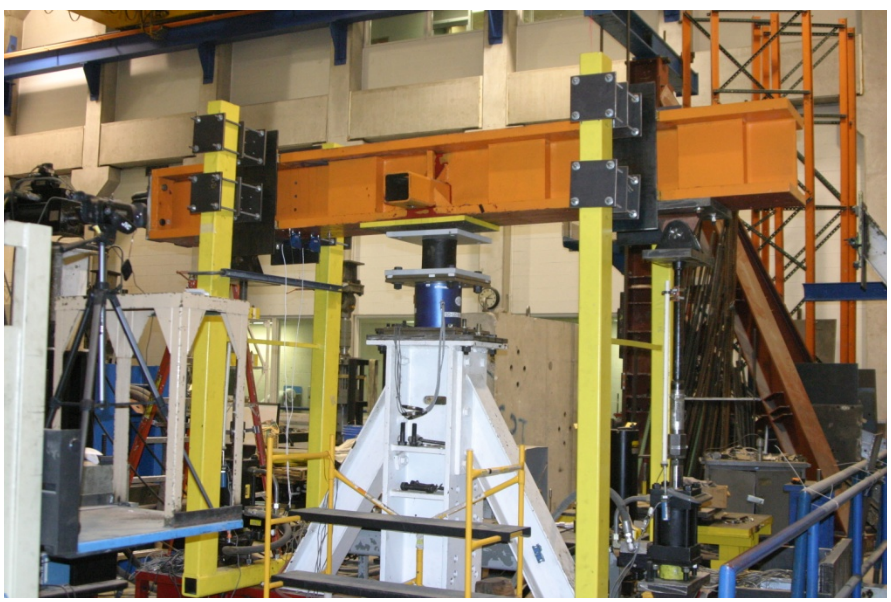

b) Photograph

Figure 4.1 Small bearing testing machine

Vertical load is applied via a horizontal loading beam and two force-controlled Parker vertical actuators both equipped with inline load cells. A horizontal actuator is used to laterally displace the loading beam and connected bearing. Relative lateral displacement is measured and recorded via an attached linear variable differential transformer (LVDT). A 5-channel reaction load cell located directly beneath the specimen is used to measure axial load, shear force, and bending moment. A summary of the instrumentation for the SBTM is found in Table 4.1.

Table 4.1 SBTM Instrumentation

No.	Data	Symbol	Source	Range
1	Lateral Force and Displacement	F , u	Horizontal Actuator/LC/LVDT	0-244.7kN, ±15.24cm
2	Vertical Force and Displacement	P , v	Parker Actuator (2)	0-622.8kN
3	Horizontal and Vertical Reaction, Moment	P , F , M	5-Channel Load Cell	0-222.4kN axial, 0-89kN lateral

In each characterization test the bearing was subjected to a constant axial load, then cycled three times to the specified displacement. The hysteretic loops (see Fig. 3.7) generated from the data permit the determination of the effective horizontal stiffness (K_{eff}) and the associated effective shear moduli (G_{eff}). In the case of the LR bearing the characteristic strength (Q_d) is also determined.

4.2.2 Test Program

Using the SBTM a single LDR bearing was tested to determine the horizontal stiffness and shear modulus. Three tests were performed at each strain level (100% and 150%) with axial loads of 0, 62, and 89 kN where shear strain is determined by:

$$\gamma = \frac{u}{T_r} \tag{4-1}$$

where is the γ shear strain, u is the displacement, and T_r is the total thickness of rubber (60 mm for this bearing). Table 4.2 summarizes the characterization program.

Table 4.2 Bearing Characterization Program

Test Number	Test Name	Bearing	Target Displacement (mm)	Target Vertical Load (kN)
1	DG100-00	LDR1	60	0
2	DG100-14	LDR1	60	62
3	DG100-20	LDR1	60	89
4	DG150-00	LDR1	90	0
5	DG150-14	LDR1	90	62
6	DG150-20	LDR1	90	89

Properties used for the LR bearing were taken from characterization testing by Warn and Whittaker (2006).

4.2.3 Results

Figure 4.2 presents sample results of bearing characterization for the LDR bearing. This figure shows the results of cycling the LDR bearing under 60 kN and 89 kN of vertical loading at 100% shear strain.

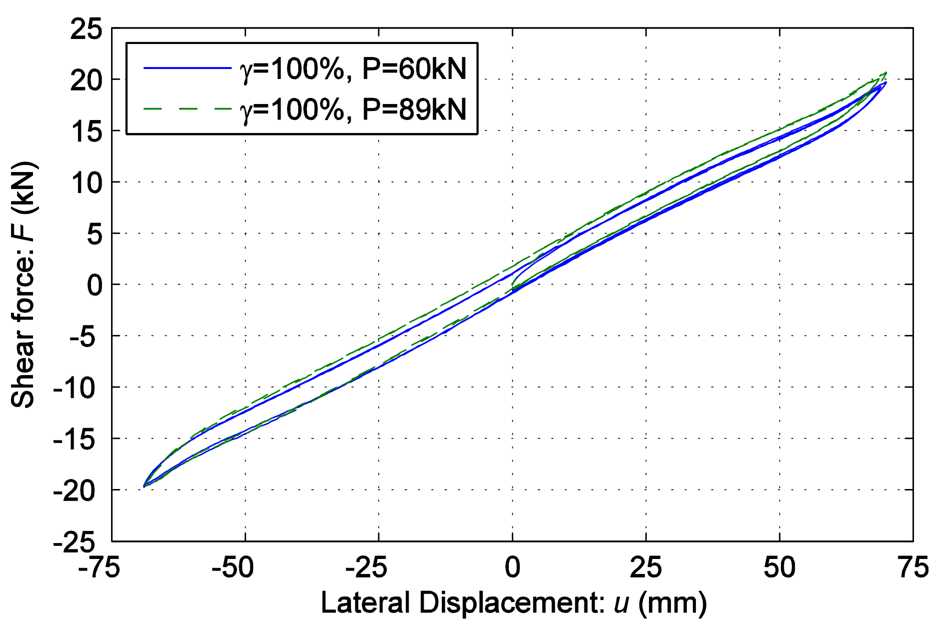

Figure 4.2 Sample results from LDR bearing characterization

A summary of the results from bearing characterization can be found in Table 4.3. For elastomeric bearings the effective horizontal stiffness, K_{eff} is calculated by:

$$K_{eff} = \frac{|F_{max}| + |F_{min}|}{|u_{max}| + |u_{min}|} \tag{4-2}$$

where F_{max}, F_{min}, u_{max}, and u_{min} correspond to the maximum and minimum shear force and maximum and minimum displacements respectively.

K_{eff} is related to the effective shear modulus, G_{eff}, by the following:

$$K_{eff} = \frac{G_{eff} \cdot A_b}{T_r} \tag{4-3}$$

where A_b is the bonded rubber area and T_r is the total thickness of rubber.

Table 4.3 LDR bearing characterization results

Test Number	Test Name	γ (%)	P (kN)	K_{eff} (kN/mm)	G_{eff} * (MPa)
1	DG100-00	115	13	0.263	0.75
2	DG100-14	116	61	0.254	0.73
3	DG100-20	116	90	0.238	0.68
4	DG150-00	169	11	0.271	0.78
5	DG150-14	167	66	0.255	0.73

* G_{eff} determined as $K_{eff}T_r / (1.2A_b)$

In lieu of performing bearing characterization tests on the LRB, mechanical properties of an identical bearing that was tested in earlier experimental work (Warn and Whittaker 2006) were used in calculations. Given little to no change was observed in the current tests as compared with Warn and Whittaker (2006) with the LDR bearings (the mechanical properties in this study were 0-4% different than those in Warn and Whittaker) the properties of the LR bearing reported in Warn and Whittaker (2006) were assumed to be representative of the tested bearing. Table 4.4 shows a summary of the LRB properties from Warn and Whittaker (2006).

Table 4.4 LR bearing characterization results

Test Number	γ (%)	P (kN)	K_{eff} (kN/mm)	G_{eff} (MPa)
1	104	60	0.42	1.44
2	104	60	0.40	1.37
3	104	60	0.40	1.37
4	104	60	0.40	1.37
1	155	60	0.35	1.20
2	155	60	0.35	1.20
3	155	60	0.34	1.20
4	155	60	0.34	1.20

4.3 Stability Testing

4.3.1 Setup and Instrumentation

Due to force requirements needed to observe critical loads over a wide range of displacements for the LDR and LR bearings the use of the LBTM was required. A schematic of the LBTM showing the bearing in the undeformed and deformed configurations can be seen in Figs. 4.3a and 4.3b respectively, while Fig. 4.4 shows a photograph of the LBTM.

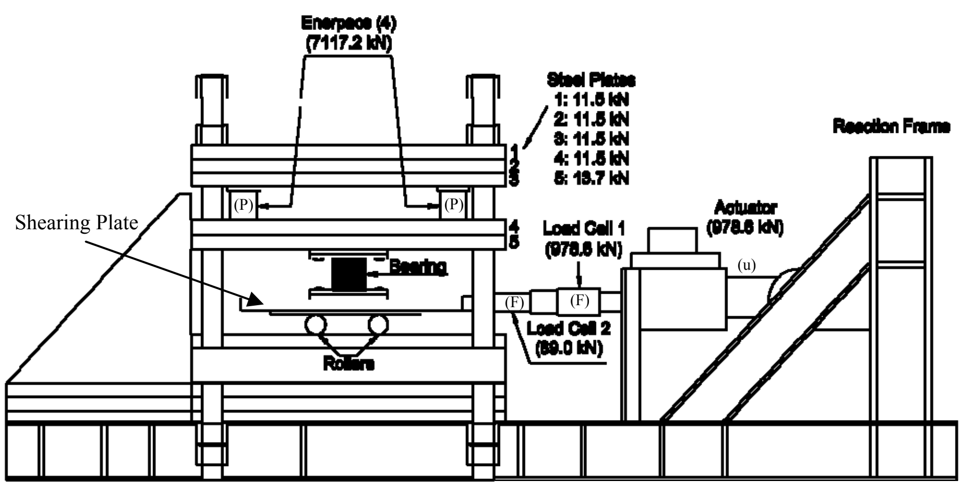

a) Undeformed configuration

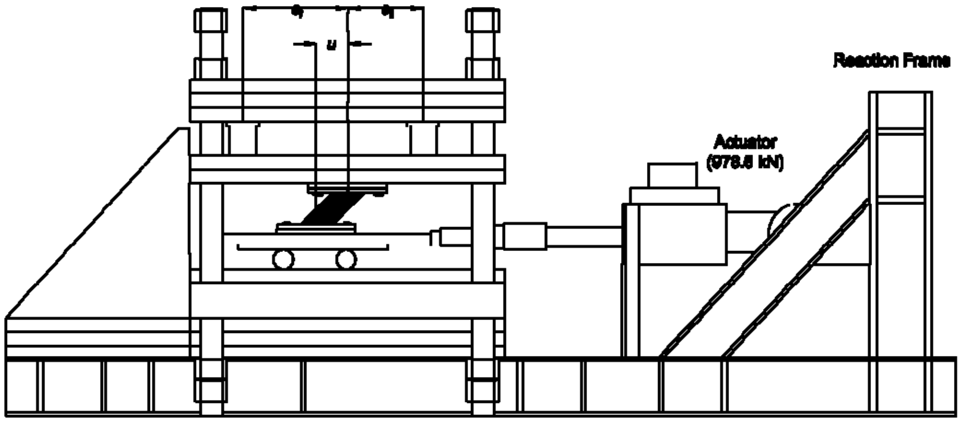

b) Deformed configuration

Figure 4.3 LBTM Schematic

Figure 4.4 LBTM Photograph

The setup of the LBTM is not conducive to maintaining a constant axial load during displacement for bearings that decrease in height with lateral displacement. Therefore the constant displacement method was used, in which the bearing is held at a specified displacement and then monotonically compressed. The constant displacement method has been used in previous studies (Buckle and Liu 1994, Buckle et al. 2002) and operates under the principle that the neutral equilibrium configuration ($\Pi = 0$) corresponds to a unique combination of axial and shear force. Unlike constant axial force methods, where the bearing is compressed to a specified load then displaced and force-displacement curves are obtained directly the constant displacement method requires an indirect determination of these curves and the corresponding critical points (discussed further in 4.3.3). The two methods should yield the same results for the LDR bearing (which exhibits path independent behavior), though the LR bearing results would likely be different due to the path dependency observed in FEA.

Loading in the horizontal direction was displacement controlled by the axial stroke of an MTS servo-controlled dynamic actuator that was positively connected to the shearing plate on which the bearing was placed. The shearing plate was stationed atop two steel cylinders to facilitate lateral translation (see Fig. 4.3a). A supplemental LC was added that had a more appropriate range for the anticipated force demands. Four string potentiometers were added at each corner to measure vertical displacement. Data from the string pots was used to monitor the rotations of the loading plates to ensure force was not being transmitted into the support posts. Table 4.5 summarizes the instrumentation used in the LBTM.

Table 4.5 LBTM Instrumentation

No.	Data	Symbol	Source	Range
1	Lateral Force and Displacement	F , u	MTS Actuator/LC Actuator/LC/LVDT	0-978.6kN, ±12.7cm
2	Axial Load	P	Enerpacs/LCs	0-7117.2kN
3	Vertical Displacement	v	String Potentiometers	±539.8cm

The vertical loading system of the LBTM consists of five loading plates and four Enerpac hydraulic jacks that self-react on nuts above the plates. The Enerpacs are used to apply additional vertical load beyond the self-weight of the system (60 kN). Vertical load was determined from pressure measured by a pressure cell (not shown in the schematic) in the hydraulic system multiplied by the area of the hydraulic jack piston. Initially the Enerpacs were spaced equidistant from the bearing center in the undeformed configuration. However, as the bearings were displaced the equidistant configuration induced rotation in the loading plates due to an unbalanced moment and violated the desired boundary conditions of having the top plate fixed against rotation (but free to translate) and the bottom plate fixed. This problem was ameliorated by locating the centroid of the four Enerpacs above the center of the bearing at the bottom plate such that $(e_1 - e_2)/2 = u$ (as shown in Fig. 4.3b) and verified using a hand level.

4.3.2 Test Program

Two LDR bearings and one LRB were subjected to stability testing via the LBTM. The use of a second, identical LDR bearing was necessary as the first LDR bearing became damaged during this phase of testing. Using the aforementioned constant displacement method each bearing was subjected to increasing vertical load at constant displacements ranging from 19 to 176 mm at approximately 6 mm intervals. This interval was chosen to allow the development of a stability curve with sufficient resolution.

Table 4.6 summarizes the stability testing program. The target vertical load reported in Table 4.6 is only an estimated value based on preliminary results of the finite element analysis in Chapter 3. During stability testing the axial load was increased until the shear force reduced nearly to zero. However, reaching zero force is not a requirement for use of the constant displacement method, which only requires the shear force-axial load trajectory of a given displacement level to cross trajectories from neighboring displacements.

Table 4.6 Stability Testing Program

Test Number	Test Name	Bearing	Target Displacement (mm)	Target Vertical Load (kN)
7	DP127-50	LDR1	76	222
8	DP138-47	LDR1	83	209
9	DP148-43	LDR1	89	191
10	DP148-43b	LDR1	89	191
11	DP138-47b	LDR1	83	209
12	DP127-50b	LDR1	76	222
13	DP127-50c	LDR1	76	222
14	DP138-47c	LDR1	83	209
15	DP148-43c	LDR1	89	191

Table 4.6 Stability Testing Program (cont.)

Test Number	Test Name	Bearing	Target Displacement (mm)	Target Vertical Load (kN)
17	DP138-47d	LDR1	83	209
18	DP148-43d	LDR1	89	191
19	DP169-36	LDR1	101	160
20	DP191-32	LDR1	114	142
21	DP212-27	LDR1	127	120
22	DP85-68	LDR1	51	302
23	DP64-73	LDR1	38	325
24	DS168-13	LDR1	101	58
25	DS168-45	LDR1	101	200
26	DS168-60	LDR1	101	267
27	DS168-90	LDR1	101	400
28	DP254-21	LDR1	152	93
30	DS168-13b	LDR1	101	58
31	DP233-24	LDR1	140	107
32	DP275-18	LDR1	165	80
33	DP297-18	LDR1	178	80
34	DP265-20	LDR1	159	89
35	DP244-23	LDR1	146	102
37	DP201-29	LDR2	120	129
38	DP117-55	LDR2	70	245
40	DP95-65	LDR2	57	289
41	DP85-68	LDR2	51	302
42	DP74-71	LDR2	44	316
43	DP169-36-2	LDR2	101	160
44	DP222-25	LDR2	133	111
45	DP127-50-2	LDR2	76	222
46	DP138-47-2	LDR2	83	209
47	DP148-43-2	LDR2	89	191
48	DP159-40-2	LDR2	95	178

Table 4.6 Stability Testing Program (cont.)

Test Number	Test Name	Bearing	Target Displacement (mm)	Target Vertical Load (kN)
50	DP212-27-2	LDR2	127	120
51	DP233-24-2	LDR2	140	107
52	DP244-23-2	LDR2	146	102
53	DP254-21-2	LDR2	152	93
54	DP265-20-2	LDR2	158	89
55	DP275-18-2	LDR2	165	80
56	DP32-80	LDR2	19	356
57	DLP32	LRB1	19	-
58	DLP64	LRB1	38	-
59	DLP85	LRB1	51	-
60	DLP106	LRB1	64	-
62	DLP148	LRB1	89	-
63	DLP169	LRB1	101	-
64	DLP191	LRB1	114	-
65	DLS169-14	LRB1	101	62
66	DLS169-50	LRB1	101	222
67	DLP212	LRB1	127	-
68	DLP233	LRB1	140	-
69	DLP254	LRB1	152	-
70	DLP275	LRB1	165	-
71	DLP297	LRB1	178	-
72	DLP42	LRB1	25	-

Notes:
1. During testing of LDR1, (particularly at 6” displacement) there was appreciable plate rotation in the test setup. This was fixed before the testing of LDR2 by rearranging the Enerpacs.
2. As of Test 191-32-2, LDR2 seemed to develop a bulge near the top end plate.

4.3.3 Results

This section presents a summary of the results from the stability testing. The complete data is presented in Appendix C. A description of the development of the experimental stability curves is discussed.

As discussed in Chapter 3, stability curves are generated indirectly when the constant displacement method is used. When the bearing is first laterally displaced to 114 mm it requires approximately 20.5 kN of shear force. This is done while the bearing is only under the self-weight of the loading plates (59.7 kN). Second, once the target displacement is reached, the axial load is monotically increased from the self-weight to 350 kN resulting in a single trajectory on Fig 4.5. This process is repeated for a large ranges of displacements. The resulting trajectories are shown in Fig. 4.5 to illustrate the determination of a critical point. After the shear force-axial load curves from each test are generated a vertical line denoting constant shear force (*F*=6kN) is then drawn.

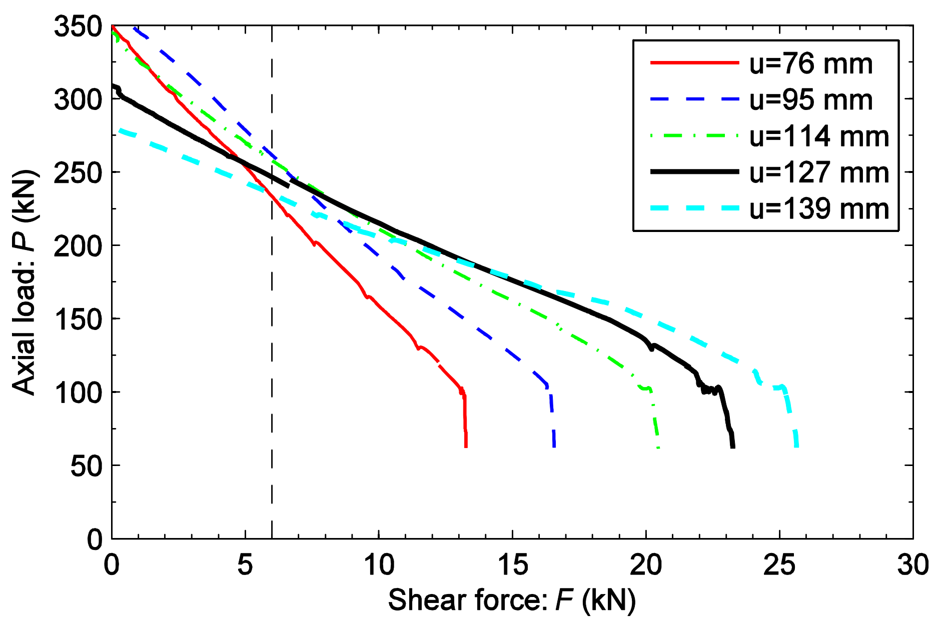

Figure 4.5 Shear force-axial load curves for LDR bearing

Points where trajectories intersect the line of constant shear are replotted on in the axial load – lateral displacement plane to find the point of neutral equilibrium as illustrated in Fig. 4.6.

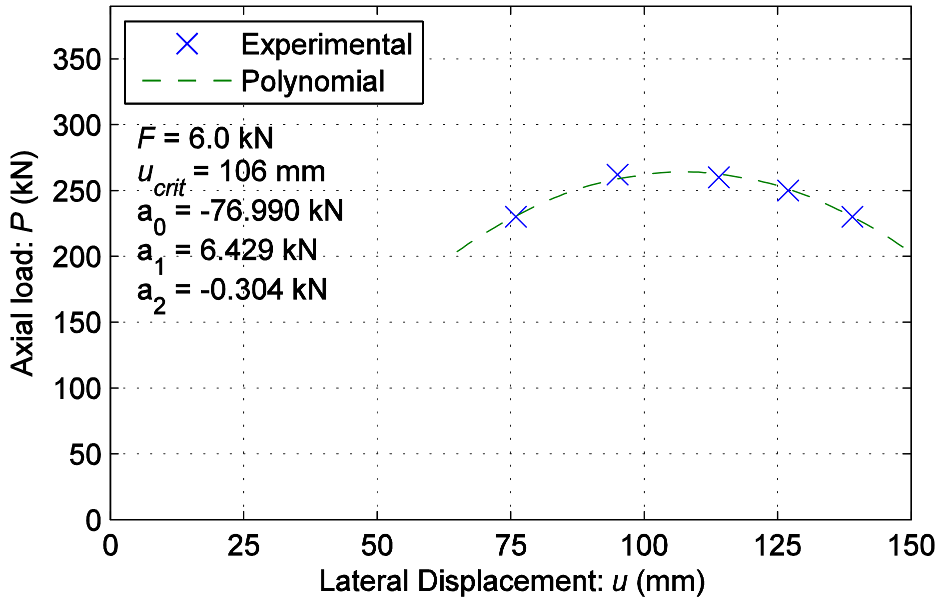

Figure 4.6 Sample axial load-displacement curve for LDR bearing

A limitation of the constant displacement method is that the discrete data points likely are not exactly coincidental with the maximum as shown in Fig. 4.6. Therefore, to be consistent from one displacement level to the next the neutral equilibrium point (maximum force) is determined from fitting a polynomial to the experimental stability results using MATLAB. The polyfit function in MATLAB uses best fit curves (in the least-squares sense) so that a reasonable estimate of the critical points could be found. In each case a polynomial of the form $P(u) = a_2u^2 + a_1u + a_0$ was fit to the data. Figure 4.6 shows an example where a critical point has been reached at approximately 106 mm when the axial load passes through a maximum of 262 kN under a constant shear force of 6 kN.

This process is repeated for both the LDR and LR bearing specimens at several shear force values using trajectories from the range of displacements at which the bearings were tested. The remaining axial load-displacement curves can be found in Appendix C. Assembling the critical load and displacement from each of these curves results in the experimental stability curves found in Fig. 4.7.

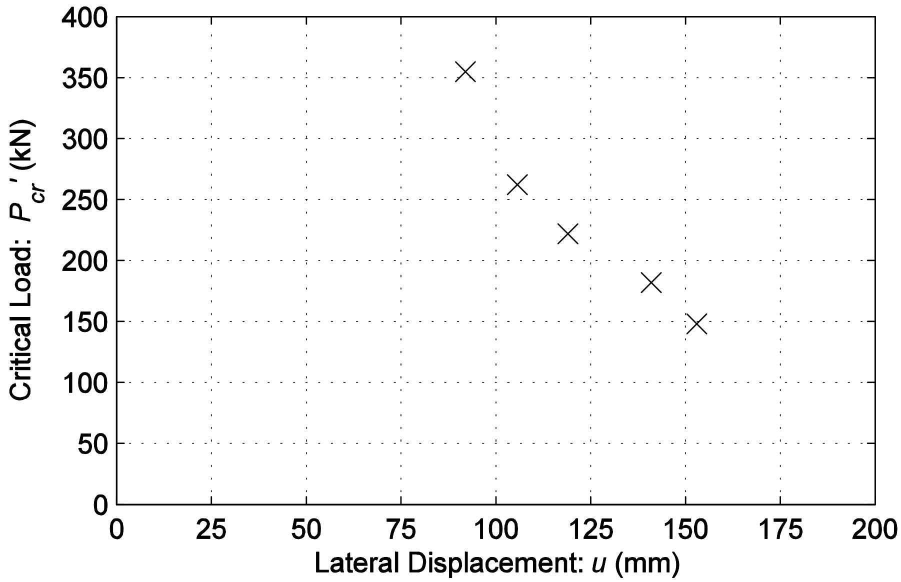

a) LDR bearing

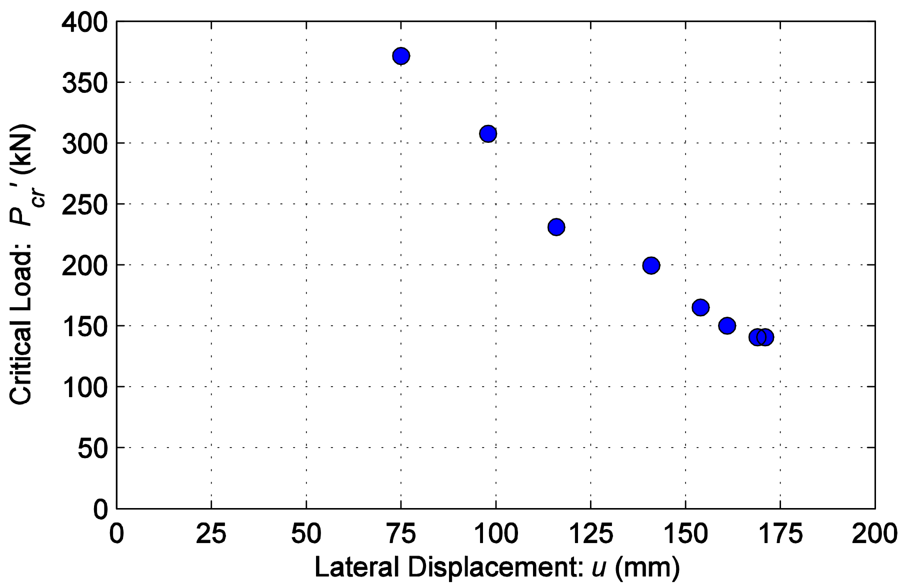

b) LR bearing

Figure 4.7 Experimental stability curves

4.4 Discussion of Experimental Results

For both the LDR and LR bearing the critical load decreases with increase lateral displacement. A visual comparison of the stability curves generated for the LDR and LR bearings shown in Fig. 4.7 provides insight into the effect of the lead core on bearing stability since the bearings are identical with the exception of the lead core. For the range of 90-150mm (where data was gathered for both bearings) the LDR and LR bearings displayed similar behavior in terms of P_{cr}' data and trend in reduction . A more direct comparison between the two bearings in absolute terms is presented in Chapter 6.

Figure 4.8 presents the stability curves in a normalized fashion – the reduced critical load, P_{cr}', is normalized by the critical load in the undeformed configuration (calculated as described in Chapter 3), P_{cr}, and the displacement is normalized by the bearing diameter, D.

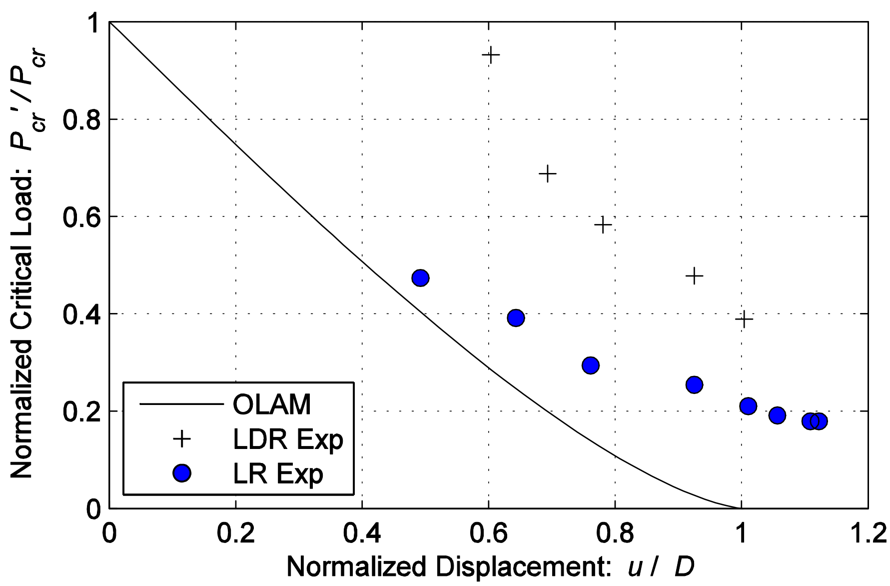

Figure 4.8 Normalized stability curves for the LDR and LR bearings

To facilitate a comparison of the experimental data with the overlapping area method the experimental data was normalized by P_{cr} (Eqns. 3-7 and 3-12 for the LDR and LR bearings respectively) and *D*. It is observed that for the full range of displacements that were tested the OLAM tends to under predict the actual capacity of the bearing. Further, when reaching a displacement equal to the bearing diameter the OLAM estimates zero capacity whereas the experimental results suggest a reserve capacity of $0.40P_{cr}$ and $0.20P_{cr}$ for the LDR and LR bearing respectively.

In summary, based on the experimental investigation several important observations can be made. These include:

1. The critical load reduces with increasing lateral displacement for both the LDR and LR bearing.
2. The LDR bearing has a reduced critical load of approximately $0.40\,P_{cr}$ at a displacement equal to the bearing diameter.
3. The LR bearing has a reduced critical load of approximately $0.20\,P_{cr}$ at displacement equal to the bearing diameter.
4. When normalized, the data shows that the OLAM provides inconsistent predictions of the capacity as it is significantly more conservative for the LDR bearing than the LR bearing.

CHAPTER 5

Analytical Investigation

5.1 General

An analytical investigation was conducted to investigate the application of the Koh-Kelly two-spring model (TSM) discussed in Chapter 2 for predicting the stability limit of elastomeric bearings. The purpose of this investigation is to explore the possibility of the use of the TSM to simulate the reduction in critical load with displacement for LDR bearings.

Although the TSM is an idealization of an elastomeric bearing, it has been shown to predict well the effect of axial load on the horizontal stiffness, damping and reduction in height (Kelly 1997, Nagarajaiah 1999) and might provide a more rigorous basis for predicting the stability limit of elastomeric bearings.

5.2 Analysis Using the Two-Spring Model

Previous studies (Nagarajaiah and Ferrrell 1999, Buckle et. al 2002) have shown that the TSM has the potential to predict instability in LDR bearings through the solution of the equilibrium equations of the model in the deformed configuration when the spring stiffnesses K_s and K_θ are reduced with displacement. After deriving and solving the equations of equilibrium for the TSM, the shear force (or axial load) can be plotted with displacement using the same methodology as the FEA to obtain the location of critical points. However, before the TSM can be used, various assumptions in the formulation of the equations of equilibrium and their effect on the solution require examination.

5.2.1 Equilibrium of the Two-Spring Model

Equilibrium of the TSM in the deformed configuration provides information that can be used to assess the stability of the model under various assumptions. Figure 2.3 is presented again as Fig. 5.1 for reference.

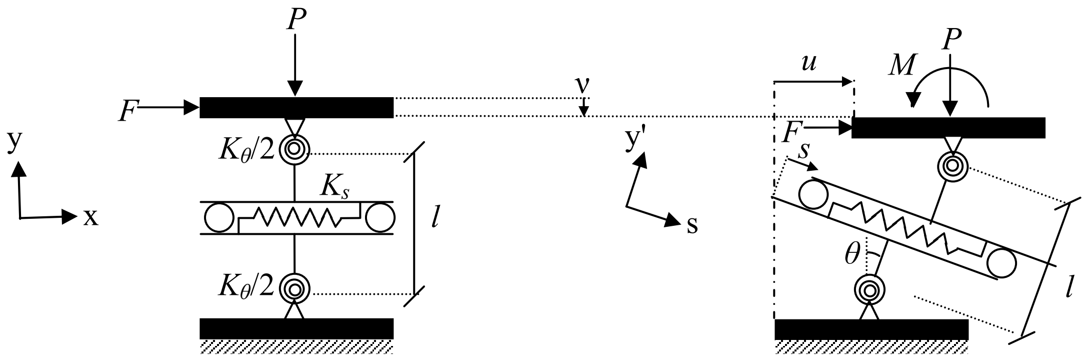

Figure 5.1 Koh-Kelly two-spring model

From Fig. 5.1 equilibrium of forces for the deformed configuration in the *s-direction* requires:

$$K_s \cdot s = F \cdot \cos(\theta) + P \cdot \sin(\theta) \tag{5-1}$$

where K_s denotes the shear stiffness (defined as GA_s / l), s is the shear deformation, θ is the bearing rotation, F is the horizontal force, and P is the vertical load. Similarly, summation of moments about the pin at the base yields:

$$K_\theta \cdot \theta = P \cdot [l \cdot \sin(\theta) + s \cdot \cos(\theta)] + F \cdot [l \cdot \cos(\theta) - s \cdot \sin(\theta)] \tag{5-2}$$

where K_θ is the rotational stiffness (initially defined as $P_E \cdot l$), and l is the bearing height. In addition to the force equilibrium equations, compatibility of the TSM dictates the global displacement quantities are related to the internal displacement quantities by:

$$u = l \cdot \sin(\theta) + s \cdot \cos(\theta) \tag{5-3}$$

where u is the global lateral displacement and the other variables have been previously defined.

Equations (5-1), (5-2), and (5-3) are solved simultaneously using iterative approaches (Gauss-Newton and Levenberg-Marquardt) in MATLAB by specifying two of the five unknown variables, for example F and u, then solving for the remaining unknowns P, s, and θ.

5.2.2 Impact of Assumptions

To identify the impact of geometric and material assumptions on the stability behavior (via spring stiffnesses), the system of equations (equilibrium and compatibility) were solved simultaneously using a MATLAB routine for the following cases:

1. linear geometry and linear material properties (LLL) – small angle theory is applied ($\cos(\theta) \approx 1, \sin(\theta) \approx \theta$) and the spring stiffnesses remain constant,
2. nonlinear geometry and linear material properties (NLL) – the trigonometric functions are used, but the spring stiffnesses are kept constant,
3. nonlinear geometry and nonlinear shear stiffness, but linear rotational stiffness (NNL) – the trigonometric functions are used and the shear spring stiffness is reduced as a function of displacement,
4. nonlinear geometry and nonlinear rotational stiffness, but linear shear stiffness (NLN) – the trigonometric functions are used and the rotational spring stiffness is reduced as a function of displacement, and
5. nonlinear geometry and nonlinear material properties (NNN) – the trigonometric functions are used and the spring stiffnesses are both reduced as a function of displacement.

In the third, fourth, and fifth cases the functions suggested in Nagarajaiah and Ferrell (1999) for $K_s^{'}$ and $K_\theta^{'}$ were used. These are:

$$K_s^{'} = K_s \cdot \left(1 - C_s \tanh(s)\right) \tag{5-4}$$

where $K_s^{'}$ is the shear stiffness at some shear deformation, *s*, and C_s is a dimensionless constant equal to 0.325 and,

$$K_\theta^{'} = K_\theta \cdot \left(1 - C_\theta^{'} \cdot s\right) \tag{5-5}$$

where $K_\theta^{'}$ is the rotational stiffness at some *s* and $C_\theta^{'}$ is given by $1/D - t_r/D$.

5.2.3 Results

Figures 5.2 to 5.6 demonstrate the importance of how geometry and material properties are considered to the stability behavior found in the TSM.

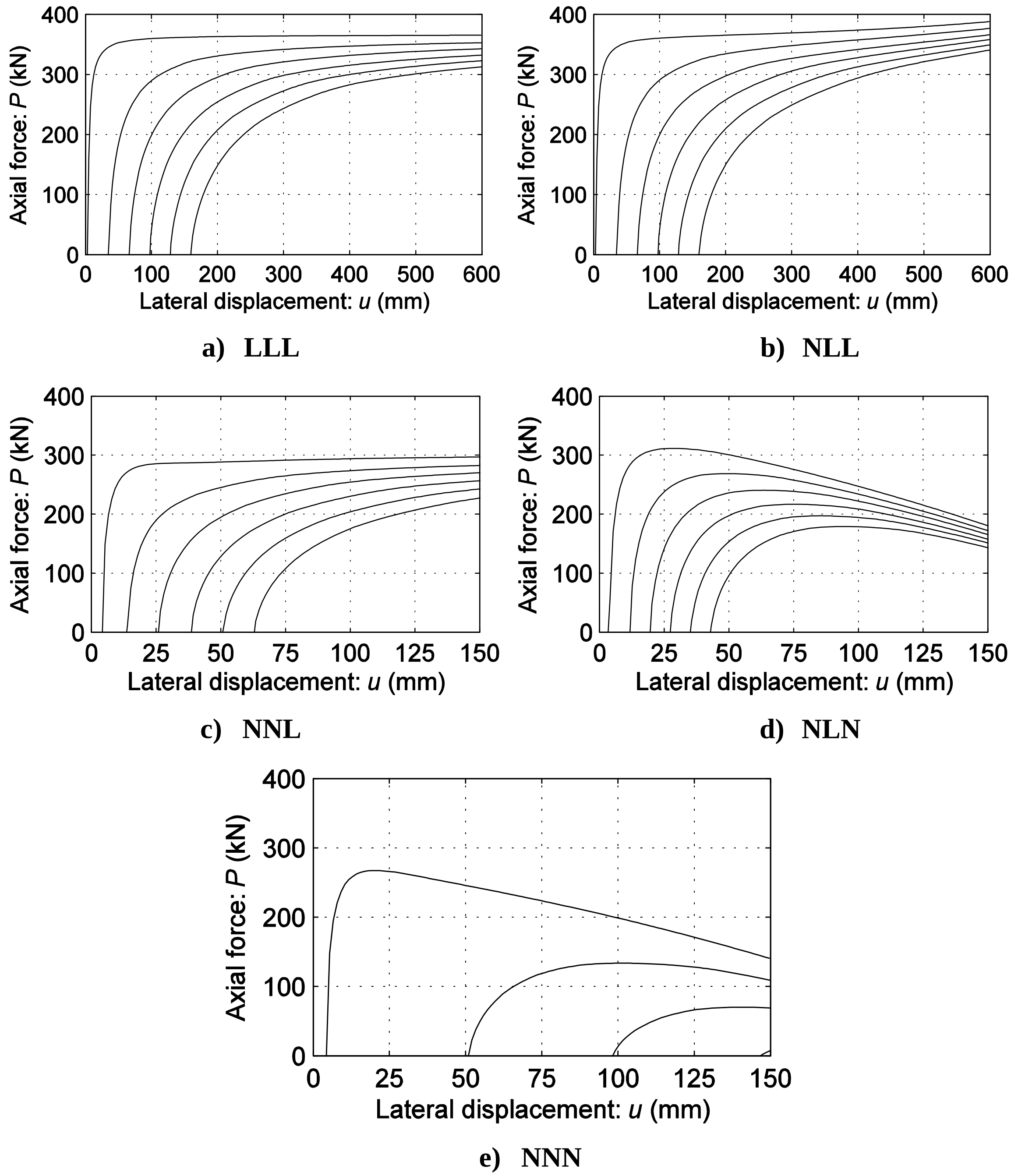

Figure 5.2 Two-spring model solutions

When everything is treated as linear (Fig. 5.2a) no critical point is reached as the axial force never passes through a maximum, even at displacements on the order of 4*D*. When geometric nonlinearity is considered, but the material properties do not reduce (Fig. 5.2b) there are once again no critical points as the bearing actually begins to display a hardening behavior at large displacements.

When geometric nonlinearity is considered along with a reducing shear stiffness and linear rotational stiffness (Fig. 5.2c) no critical points are obtained. However, assuming geometric nonlinearity in conjunction with a reducing rotational stiffness and linear shear stiffness (Fig. 5.2d) the curves pass through a maximum indicating instability does occur. The fact that no critical points are observed with a reducing shear stiffness, but critical points are observed with a reducing rotational stiffness suggests the dominating stiffness parameter is $K_\theta^{'}$.

In the final case where full nonlinearity is assumed (Fig. 5.2e) the axial forces pass through a maximum, indicating critical points have been reached. Using the assumptions from this case, analytical stability data is generated and presented in Fig. 5.3. This curve will be compared to the experimental and FEA data in Chapter 6 to determine the general applicability of the assumed functions for $K_s^{'}$ and $K_\theta^{'}$.

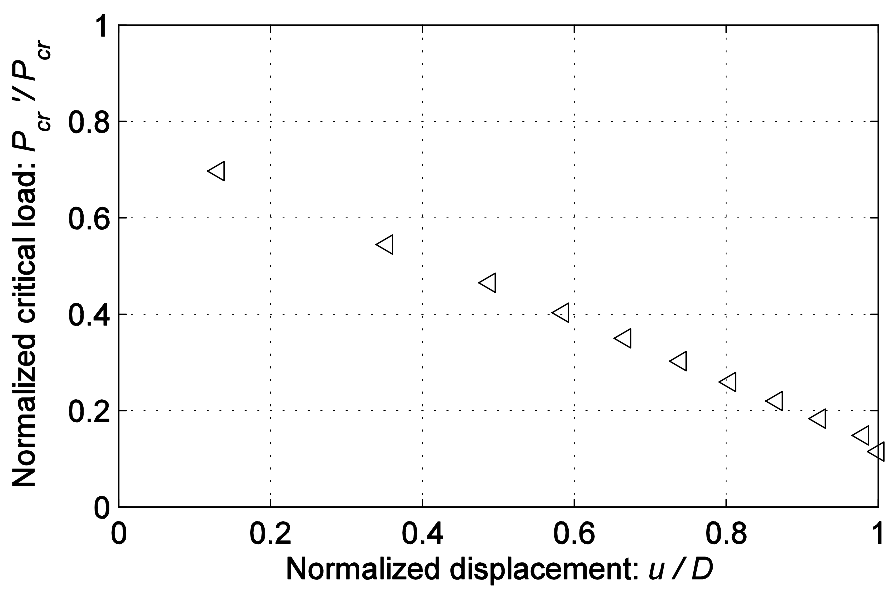

Figure 5.3 Analytical stability data

5.3 A Mechanics Based Approach

As demonstrated by the lack of critical points in Figs. 5.2a-5.2c it is necessary to consider a reduction in $K_\theta^{'}$ with shear deformation (or displacement) if the TSM is to be used to predict instability. However, Eqn. (5-5) provided by Nagarajaiah and Ferrell (1999) is based on empirical data rather than theoretical principles and might not be generally applicable.

As an alternative to the relationship for $K_\theta^{'}$ provided by Nagarajaiah and Ferrell (1999) a mechanics based approach was investigated that used by Iizuka (2000) to determine how the rotational stiffness ($K_\theta^{'}$) reduces with increasing lateral displacement was investigated. Iizuka (2000) considers the plastification of a single rubber layer and develops a relationship between the applied moment and rotation. Figure 5.4 shows an illustration of the plastification of this cross section.

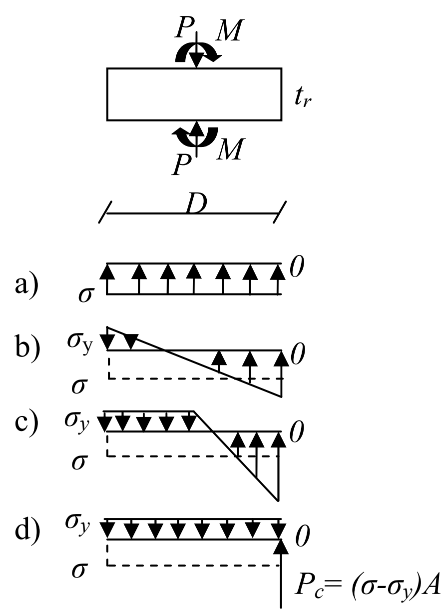

Figure 5.4 Rubber layer plastification: a) vertical load only b) vertical load and moment at the elastic limit c) between the elastic limit and ultimate d) ultimate (fully plastic)

Before yielding occurs ($\theta \le \theta_y$) the moment and rotation are linearly related by the initial rotational stiffness, K_θ. This results in:

$$M = K_\theta \theta \tag{5-6}$$

As the section begins to plastify $K_\theta^{'}$ reduces from this initial value to zero once the plastic moment has been reached. A hyperbolic function that met the required boundary conditions (from geometry of the cross-section $M_p = 4M_y$ and $M = M_y$ at $\theta = \theta_y$) was specified for the region beyond yield:

$$\frac{M}{M_y} = 4 - \frac{3}{\left[1 + \frac{1}{3}\left(\frac{\theta}{\theta_y} - 1\right)\right]^{\frac{1}{3}}} \tag{5-7}$$

where the yield moment, M_y, is given by (5-7):

$$M_y = Z \cdot (\sigma - \sigma_y) \tag{5-8}$$

in which Z is the section modulus, σ is the applied stress (P / A), and σ_y is the tensile yield stress. Differentiating the moment in (5-7) with respect to theta leads to the equation of $K_\theta^{'}$ for any rotation beyond yield. This results in:

$$K_\theta^{'} = \frac{M_y}{\theta_y\left(\frac{\theta}{3\theta_y} + \frac{2}{3}\right)^2} = \frac{K_\theta}{\left(\frac{\theta}{3\theta_y} + \frac{2}{3}\right)^2} \tag{5-9}$$

The pre-yield and post-yield values of $K_\theta^{'}$ were incorporated into the solution scheme used by MATLAB by making $K_\theta^{'}$ an additional unknown and using (5-9) as a fourth equilibrium equation along with (5-1), (5-2) and (5-3) so the system was still theoretically solvable. However, upon the introduction of this approach, the solutions provided by MATLAB no longer maintained equilibrium and therefore were deemed inadmissible.

5.4 Discussion

The TSM is only a viable model for predicting instability when a reduction in the rotational stiffness is considered. While the method using concepts from Iizuka (2000) presents a theoretical alternative to (5-5) it breaks down in application due to its simultaneous dependence on the axial load and rotation and the inability to solve the new system of equations without the introduction of significant error in equilibrium.

The general applicability of the treatment of the spring stiffnesses by Nagarajaiah and Ferrell (1999) is questionable, but will be investigated further when the results are compared with experimental values in the following chapter.

CHAPTER 6

Results and Conclusions

6.1 General

In this section the results of the finite element (Chapter 3), experimental (Chapter 4), and analytical (Chapter 5) studies are synthesized. These results are compared with the overlapping area method (OLAM) predictions to evaluate its performance. Conclusions with regard to what has been learned in these studies and remarks upon future investigations are made.

6.2 Results

Figure 6.1 shows results for the LDR bearing FEA (using both the constant axial force method and constant displacement method) and experimental investigation.

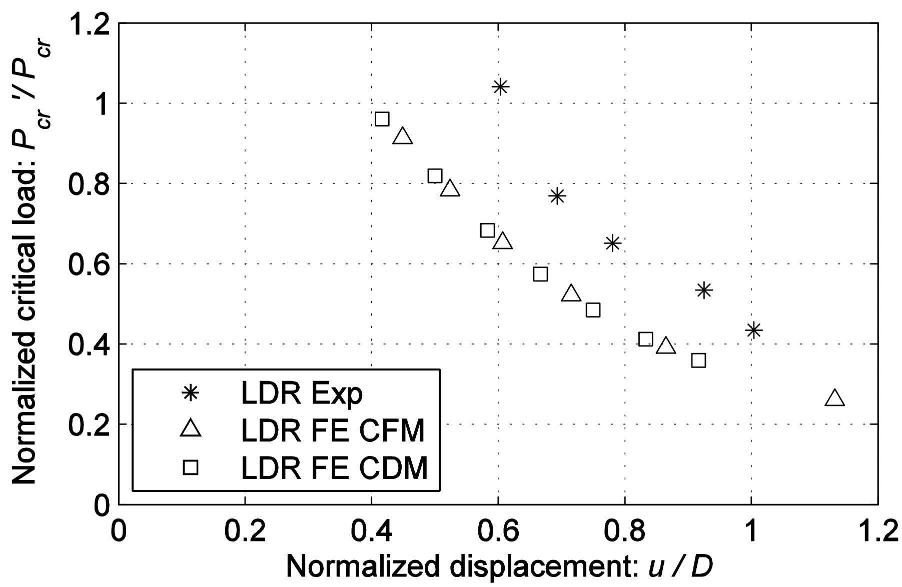

Figure 6.1 Comparison of FEA and experimental results for the LDR bearing

The finite element predictions for LDR bearing demonstrate reasonably good agreement with the observed trends in experimental data. However, there is a significant difference between values predicted by the FEA and those observed experimentally. At $u / D = 0.6$ the experimental results suggest nearly 45% more critical load capacity than the FEA predicts. At $u / D = 1.0$ the difference between results is approximately 15%. Two potential factors contributing to this difference are the material models and boundary conditions. The rubber layers were modeled using a simple hyperelastic model (the Neo-Hookean) which might not be appropriate for all loading conditions studied. For example, the Neo-Hookean does not consider the stiffening that occurs in elastomers (cross-linked polymers) at large shear strains after the polymeric chains are maximally stretched. While the Neo-Hookean provides an approximation of the behavior without the necessity of using empirically derived parameters, complex models such as the Mooney-Rivlin model have been shown to have better agreement with experimental data in previous studies (Buckle et al. 2002).

In addition to the material models, the boundary conditions enforced in the FEA were not fully maintained during experimental testing. In the models the bearings were restrained against rotation at the top and bottom end plates. However, while small (less than one degree), the experimental setup allowed some rotation in both the direction of loading (north-south) and the perpendicular direction. Rotation was calculated using a trigonometric relationship between measurements from string potentiometers located at the corners of the loading plates above the bearing and the fixed distance between them. Figure 6.2 shows a sample plot of the variation of rotation with axial load.

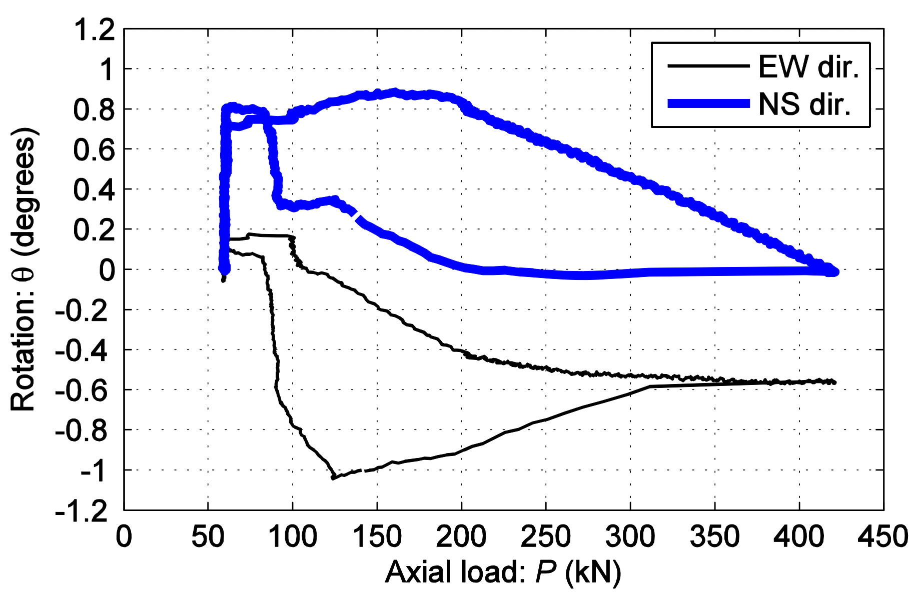

Figure 6.2 Rotation in the experimental setup

Figure 6.3 provides a comparison of the finite element solutions to the OLAM with reference to experimental results.

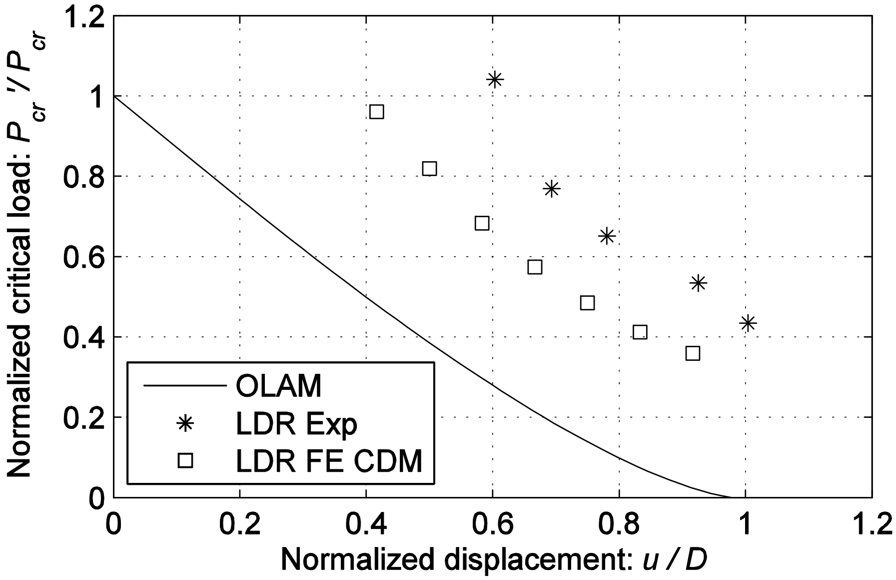

Figure 6.3 Comparison of FEA and OLAM results for the LDR bearing

Despite the aforementioned deviations between FEA and experimental results, the FEA performs significantly better than the OLAM over the entire range of displacements considered. At u / D = 0.6 the difference between experimental observations and OLAM predictions is on the order of 300%. When displacement reaches the bearing diameter the difference in results approaches infinity as the OLAM predicts zero critical load capacity at $u / D = 1.0$ whereas the experimental results suggest that a load of nearly $0.4P_{cr}$ can be sustained.

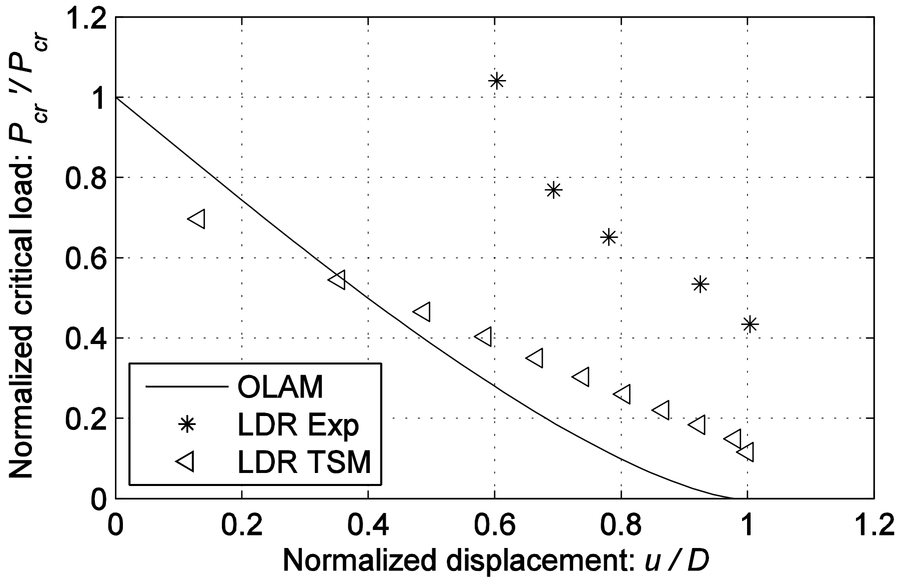

Figure 6.4 Comparison of TSM and OLAM results for the LDR bearing

Using the suggested reductions in spring stiffness properties from Nagarajaiah and Ferrell (1999) the TSM provides better estimates (compared to the experimental results) than the OLAM at displacements greater than u / D = 0.5. This suggests that the TSM has the capability of outperforming the OLAM. However, as both the TSM solutions and OLAM demonstrate significant error it is clear that both formulations can be improved upon. Figure 6.4 shows a comparison of the two FEA methods with experimental results.

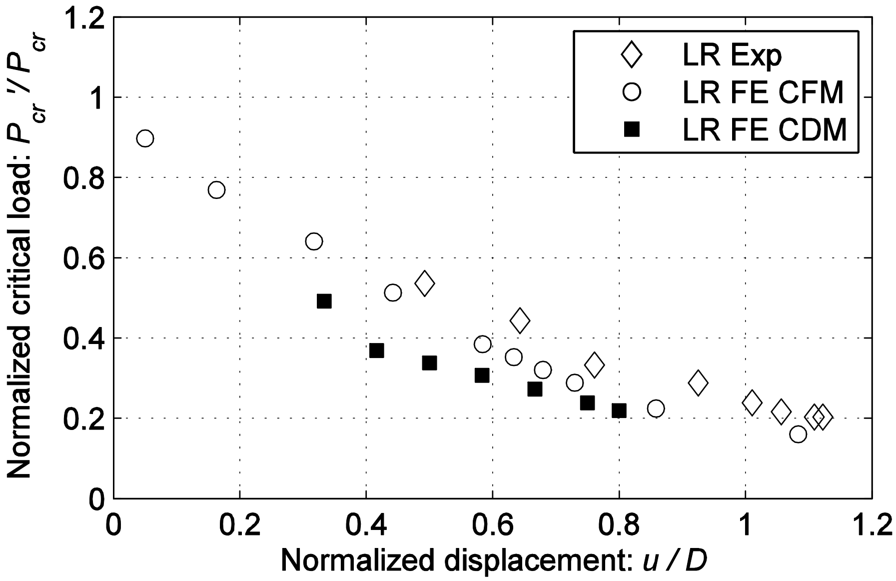

Figure 6.5 Comparison of FEA and experimental results for the LR bearing

Beyond a normalized displacement of 0.2, the constant axial force method more accurately estimates critical loads (with respect to the experimental observations) increasing in performance with increasing lateral displacement. The CDM also becomes more accurate with increasing displacement, but appears to provide a lower bound estimation of the critical load and is less accurate than the CFM over the range which they are able to be compared.

Similarly to the LDR bearing models, the FEA performed for the LR models had several potential sources of modeling error that may explain deviation from experimentally observed results. In addition to the boundary conditions and material model of the rubber layers, the lead core was assumed to be constrained to the surrounding elements when in reality the connectivity is via contact. The connected nodes in the FEMs are, however, justified to some degree by the fact that under axial load the tightly fit lead core will attempt to expand laterally into the rubber layers and as a result form keyed joints.

Because the CDM was used in the experimental investigation the FEA results from the CDM for the LR bearing was used for comparison with the OLAM in Fig. 6.6.

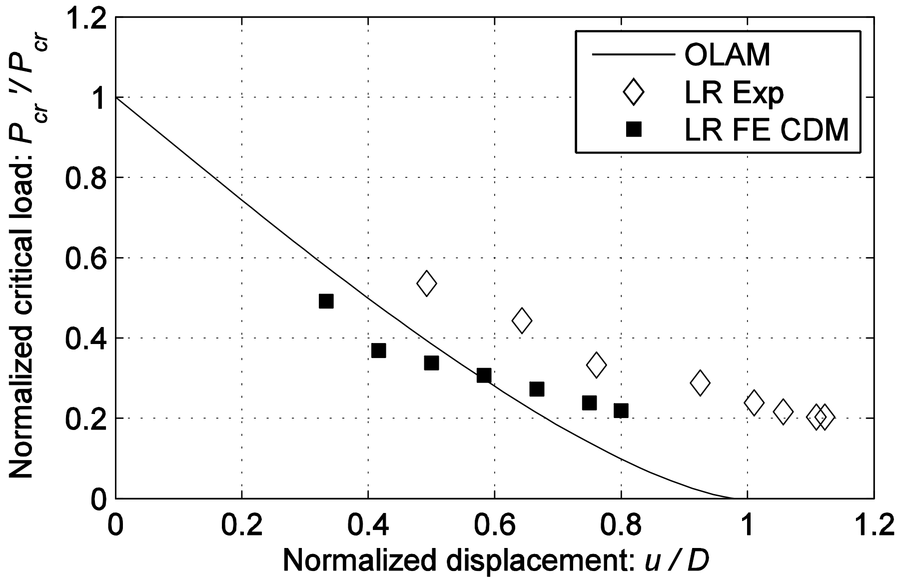

Figure 6.6 Comparison of FEA and OLAM results for the LR bearing

In the case of the LR bearing the OLAM performs to a similar degree of accuracy as the finite element results using the constant displacement method up to a normalized displacement of approximately 0.75. By comparison with Figure 6.3 it is evident that the margin of safety against failure for the LR bearing is smaller than for the LDR bearing.

For clarity on the effect of the lead core Fig. 6.7 presents the experimental stability data for both bearings in absolute terms.

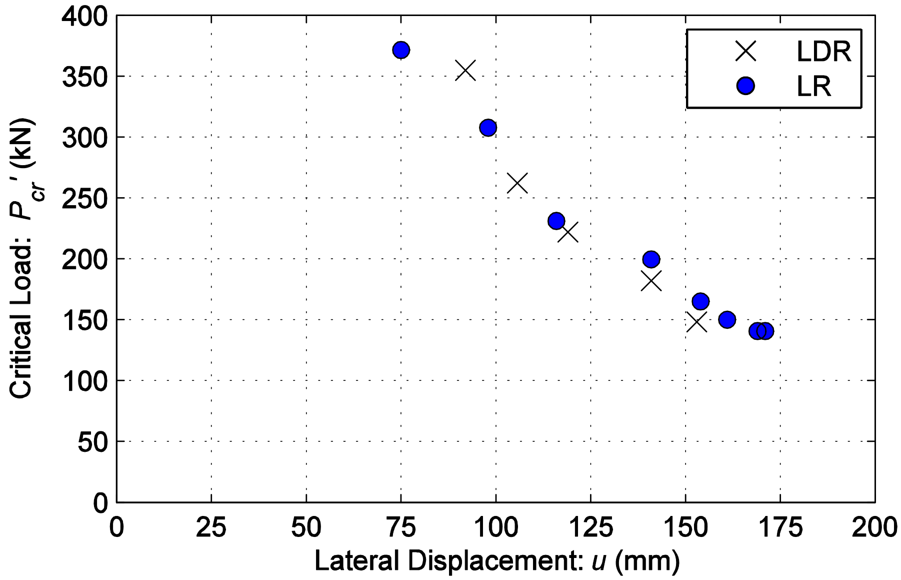

Figure 6.7 Stability curves for the LDR and LR bearings

The results shown in Fig. 6.7 indicate that the lead-core does not increase the capacity of the LR bearings over the LDR bearings in the displacement range of 75 to 175 mm, corresponding to 125% and 290% shear strain respectively. One likely explains for this observation in that the lead core yields soon after the bearing is sheared and therefore contributes no additional stiffness to the system, limiting the affect on the stability behavior in the range of displacements for which critical points could be determined. However, because the lead core does impact the calculation of P_{cr}, the two curves would deviate considerably as they approach zero lateral displacement.

6.3 Conclusions

Through these investigations several important observations have been made with respect to the stability behavior of LDR and LR bearings. It has been shown that the critical load reduces with increasing lateral displacement, while the bearing is subjected to the largest axial load demands due to overturning effects while simultaneously being at the largest displacement.

It was demonstrated experimentally that the stability behavior of elastomeric bearings is not enhanced through the addition of a lead core, so in order to meet requirements of the stability limit state other solutions (such as the use of shape memory alloys) might need to be investigated. The lead core has, however, been shown to impart path dependent behavior, suggesting further investigation will be needed when choosing between the constant displacement and constant axial force method and that correctly predicting the future loading scheme is important. However, the inherently random nature of earthquakes makes the CDM (which provides more conservative solutions) a more attractive method.

The investigation into the TSM has shown that the treatment of the reduction of the rotational stiffness is the overriding factor as to whether or not the TSM can be used to detect instability. The current, empirical approach for this reduction (Nagarajaiah and Ferrell 1999) does not appear to be generally applicable based on the comparison provided in Fig. 6.4. The use of a mechanics based solution utilizing concepts from Iizuka (2000) might be appropriate if it can be properly applied within a solution scheme.

The overlapping area method is inconsistent in its predictions between a LR and LDR bearing that were shown experimentally to exhibit similar stability behavior over the range of displacements studied. As a result the OLAM predicts critical loads with different margins of safety against exceeding the stability limit state for the two bearing types. Results from the FEA parametric study would suggest that this inconsistency is at least in part due to the OLAM's lack of incorporating the effect the shape factor (or alternatively the rubber layer thickness and diameter) into its predictions and that an improved formulation that includes these properties would be ideal. The incorporation of the λ factor derived from the parametric study (or something similar) might provide a method for making the OLAM generally applicable and more accurate, though another factor will be required to account for lead cores.

6.4 Future Study

Future work regarding the stability of LDR and LR bearings should further investigate the use of a mechanics based approach to the reduction in the rotational stiffness used in the Koh-Kelly two-spring model. Modeling the reduction with a rigorous basis might lead to the development of a closed form solution that can be used efficiently in design. In addition to the utilization of concepts from Iizuka (2000) it might prove useful to incorporate observed effects on the reduction in critical load from the two-dimensional parametric study into such a solution (or a modified version of the overlapping area method) so that it could be generally applicable for a wide range of bearing geometries and materials. Ultimately, however, this will require a more fundamental understanding of the general instability problem that is being observed in elastomeric bearings.

References

American Association of State Highway and Transportation Officials (1999). *Guide Specifications for Seismic Isolation Design*.

American Association of State Highway and Transportation Officials (1999). *AASHTO LRFD Bridge Design Specifications*.

American Society of Civil Engineers (2005). *ASCE 7-05: Minimum Design Loads for Buildings and Other Structures.*

American Society of Civil Engineers (2000). *FEMA 356: Prestandard and Commentary for the Seismic Rehabilitation of Buildings.*

Bathe, K.J. (1996). Finite element procedures, Prentice Hall, Englewood Cliffs, N.J.

Buckle, I.G. and Liu, H., (1994). "Experimental Determination of Critical Loads of Elastomeric Isolators at High Shear Strain," *NCEER Bulletin*, Vol 8, No 3, 1-5.

Buckle, I.G., Nagarajaiah, S., and Ferrell, K., (2002). "Stability of Elastomeric Isolation Bearings: Experimental Study," *J. Struct. Eng.,* 128(1), 3-11.

Building Seismic Safety Council (2003). *FEMA 450: NEHRP Recommended Provisions for Seismic Regulations for New Buildings and Other Structures*.

Constantinou, M.C., Kartoum, A., and Kelly, J.M. (1992). "Analysis of compression of hollow circular elastomeric bearings." *Engineering Structures*, 14(2), 103-111.

Derham, C. J., and Thomas, A.G. (1981). "The design of seismic isolation bearings." *Control of Seismic Response of Piping Systems and Other Structures by Base Isolation*. University of California, Berkeley, CA, 21-36.

DIS. Dynamic Isolation Systems. 18 May 2009. <http://www.dis-inc.com>.

DSSC (2008). *ABAQUS/CAE User's Manual: Version 6.8-1*. Dassault Systèmes Simulia Corp., Providence, RI.

Engesser, F., (1891) *Zentr. Bauverwaltung,* Vol 2, p. 483.

Ferrell, K., (1996). "Stability of Elastomeric Seismic Isolation Bearings," MS Thesis, University of Missouri, Columbia.

Gent, A.N., (1964). "Elastic Stability of Rubber Compression Springs," *J. Mech. Eng. Sci.,* Vol 6, No 4, 318-326.

Guruswamy, S., (2000). *Engineering Properties and Applications of Lead Alloys*. Marcel Dekker, Inc., NY.

Haringx, J.A., (1948-1949). "On Highly Compressive Helical Springs and Rubber Rods and Their Applications for Vibration Free Mountings – Parts I, II, and III," *Phillips Research Reports.*

Hirata, K., Matsuda, A., and Yabana, S. "Numerical Simulations of Rubber Bearing Tests and Shaking Table Tests," Central Research Institute of Electric Power Industry. < http://www.iaea.org/inisnkm/nkm/aws/fnss/fulltext/te_1288_prn_5.pdf>. 10 January 2010.

HPC Group. High Performance Computing. "Lion-XJ Computational Cluster." 5 April 2010. <http://rcc.its.psu.edu/hpc/systems/lionxj/#specs>.

Hirata, K., Matsuda, A., and Yabana, S. "Numerical Simulations of Rubber Bearing Tests and Shaking Table Tests," Central Research Institute of Electric Power Industry. < http://www.iaea.org/inisnkm/nkm/aws/fnss/fulltext/te_1288_prn_5.pdf>. 10 January 2010.

Imbimbo, M. and Kelly, J.M., (1998). "Influence of Material Stiffening on Stability of Elastomeric Bearings at Large Displacements," *J. Eng. Mech.*, September, 1045-1049.

International Code Council (2003). *International Building Code*.

Kelly, J.M., (1997). *Earthquake Resistant Design with Rubber*, 2nd Ed. Springer Verlag, NY.

Kelly, J.M. and Naeim, F., (1999). *Design of Seismic Isolated Structures: From Theory to Practice*. John Wiley & Sons, Inc., NY.

Kelly, J.M., (2003). "Tension Buckling in Multilayer Elastomeric Bearings," *J. Eng. Mech.*, 129 (12), 1363-1368.

Koh, C.G. and Kelly, J.M., (1987). "Effects of Axial Load on Elastomeric Bearings," UCB/EERC – 86/12, Earthquake Engineering Research Center, University of California, Berkeley.

MathWorks (2008). *MATLAB Version 7.6.0.324*. The MathWorks, Inc., Natick, MA.

Nagarajaiah, S. and Ferrell, K., (1999). "Stability of Elastomeric Isolation Bearings," *J. Struct. Eng.,* 125(9), 946-954.

Roeder, C.W., (1987). "Performance of Elastomeric Bearings," *NCHRP Report,* Washington, D.C. Highway Research Board, 102 pp.

Ryan, K., Kelly, J.M., and Chopra, A., (2005). "Nonlinear Model for Lead-Rubber Bearings Including Axial-Load Effects," *J. Eng. Mech.*, 131(12), 1270-1278.

Simo, J.C. and Kelly, J.M., (1984). "Finite Element Analysis of the Stability of Multilayer Elastomeric Bearings," *Engineering Structures*, Vol 6, 162-174.

Tauchert, T., (1974). *Energy Principles in Structural Mechanics*, McGraw-Hill, NY.

Timoshenko, S.P. and Gere, J.M., (1964). *Theory of Elastic Stability*, 2nd ed. McGraw-Hill Book Company, NY.

Warn, G. and Whittaker, A., (2006). "A Study of the Coupled Horizontal-Vertical Behavior of Elastomeric and Lead-Rubber Seismic Isolation Bearings," *MCEER-06-0011*, University at Buffalo, The State University of New York.

APPENDIX A

Supplemental Parametric Study Results

As it was discussed in Chapter 3, a parametric study was performed to better understand the importance of several geometric factors (shape factor, bearing width, and rubber layer thickness) on stability behavior of the bearing. A summary of the models generated along with corresponding notes is presented again in Table 1.

Table A.1 Model Bearings

Model Number	S	b (in.)	t_r (in.)	n	h (in.)	t_s (in.)	P_{cr} (k)	#Elements	Runtime[2] (s)
b15tr250n20	30.00	15	0.250	20	7.375	0.125	109.50	21,240	760.12
b15tr375n20	20.00	15	0.375	20	9.875	0.125	48.67	10,620	461.20
b15tr500n20	15.00	15	0.500	20	12.375	0.125	27.37	8,496	364.63
b15tr625n20	12.00	15	0.625	20	14.875	0.125	17.52	9,440	389.45
b10tr375n20	13.33	10	0.375	20	9.875	0.125	14.42	11,328	728.17
b12tr375n20	16.00	12	0.375	20	9.875	0.125	24.92	18,880	542.43
b20tr375n20[1]	26.67	20	0.375	20	9.875	0.125	115.36	3,360	602.67
b15tr375n5	20.00	15	0.375	5	2.375	0.125	194.67	6,960	225.07
b15tr375n10	20.00	15	0.375	10	4.875	0.125	97.33	10,560	440.52
b15tr375n15	20.00	15	0.375	15	7.375	0.125	64.89	14,160	654.40
b15tr1500n20	5.00	15	1.500	20	32.375	0.125	3.04	3,540	167.13
b375tr375n20	5.00	3.75	0.375	20	9.875	0.125	0.76	3,540	112.31
b15tr3000n20	2.50	15	3.000	20	62.375	0.125	0.76	1,770	97.170
b187tr375n20[3]	2.50	1.875	0.375	20	9.875	0.125	0.09	1,770	105.38

[1]The input file for b20tr375n20 is called S20b1500p10.
[2]The runtime is associated with the time it took to run each model using the LIONX cluster in Penn State's High Performance Computer network using 8 cpus in parallel.
[3]No critical points were obtained from this model.

Each model was run in ABAQUS at nine axial load levels varying from $0.1P_{cr}$ to $0.9P_{cr}$. When possible critical points were recovered, however, in several instances critical points were not observed due to an axial load that was too small in the displacement range of interest or failure of models to run due to solver issues in ABAQUS that were unable to be resolved.

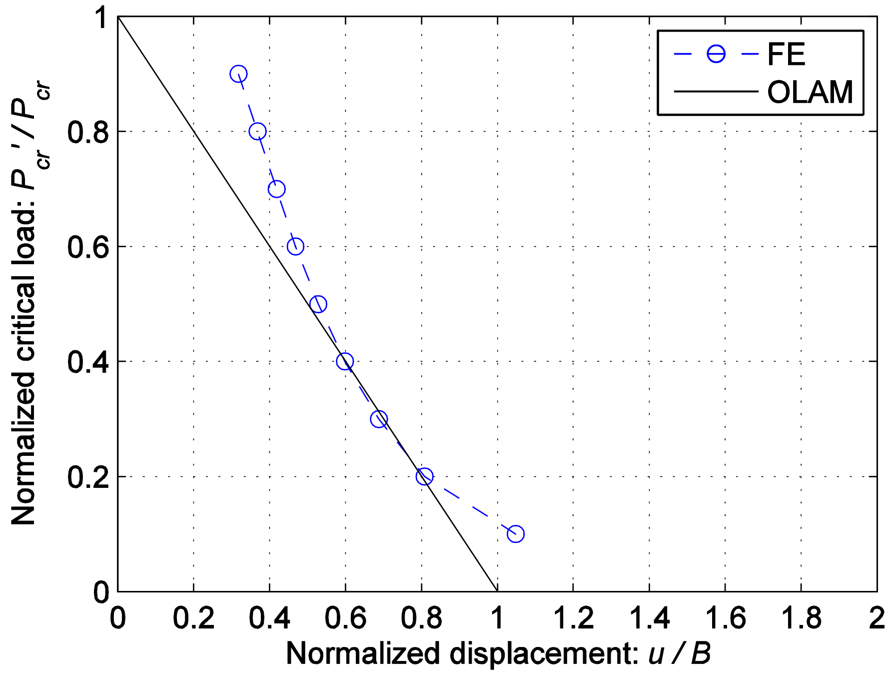

Figure A.1 Stability curve for b15tr250n20

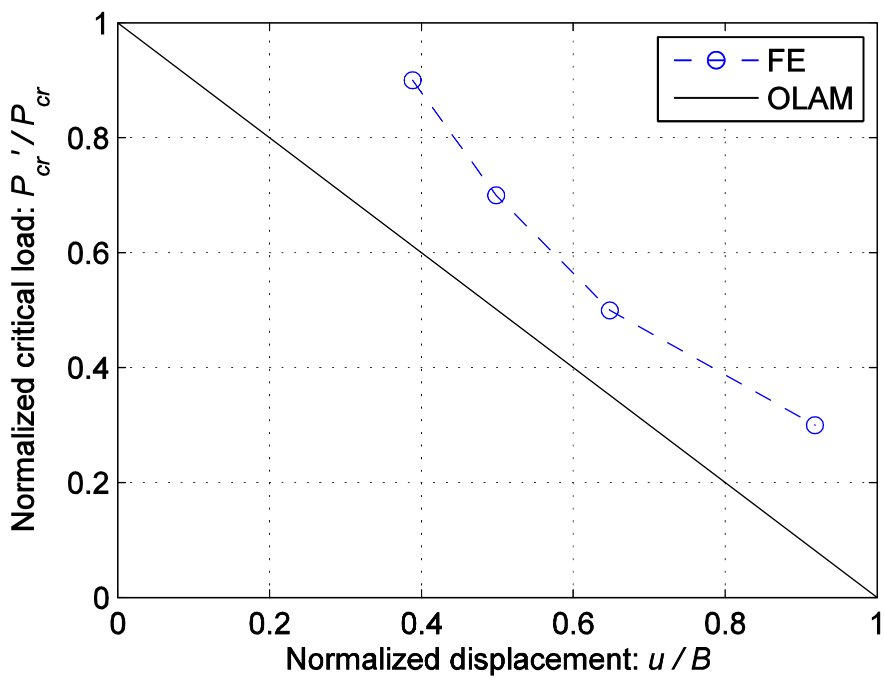

Figure A.2 Stability curve for b15tr375n20

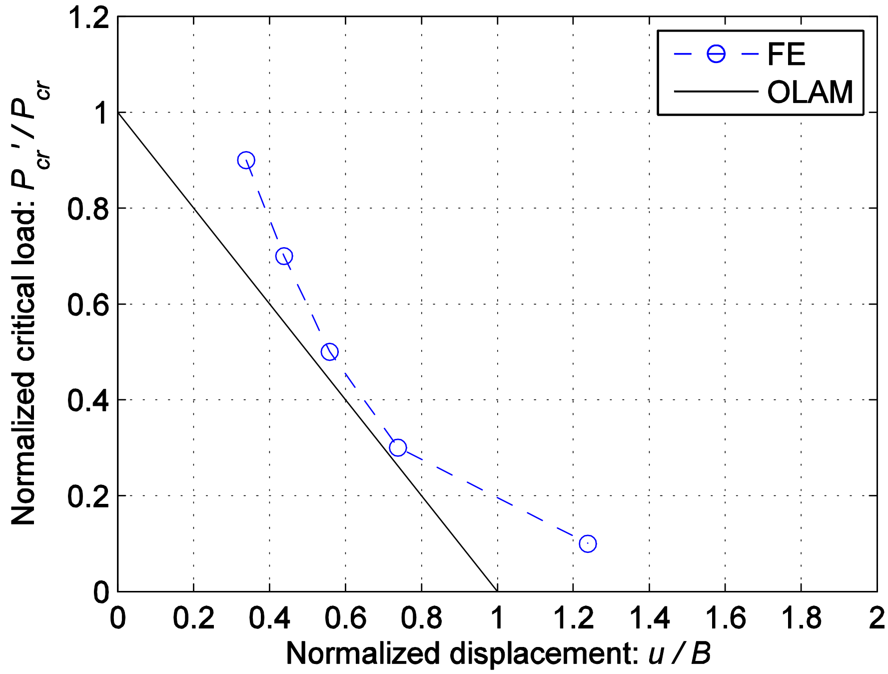

Figure A.3 Stability curve for b15tr500n20

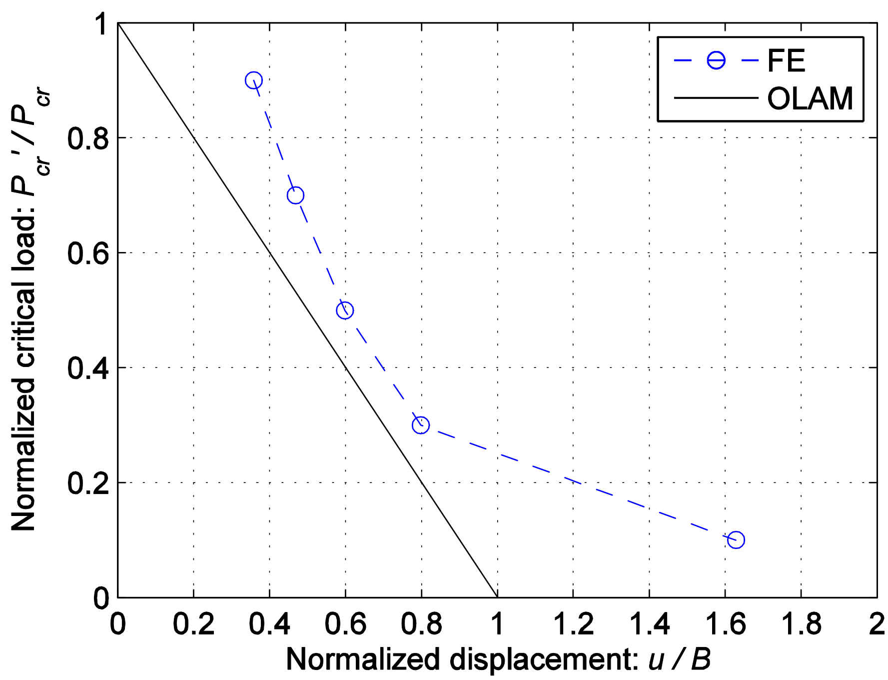

Figure A.4 Stability curve for b15tr625n20

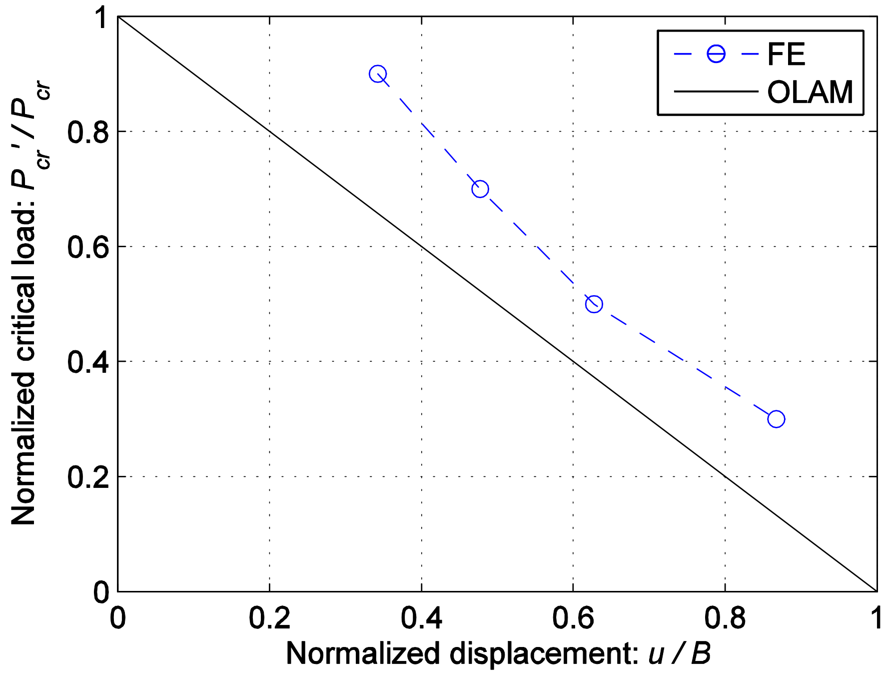

Figure A.5 Stability curve for b10tr375n20

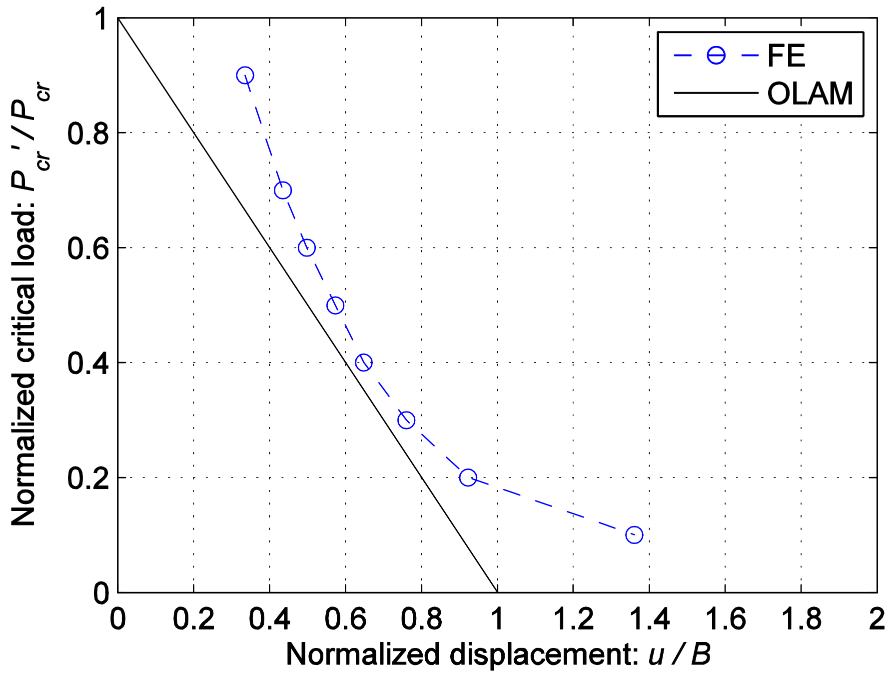

Figure A.6 Stability curve for b12tr375n20

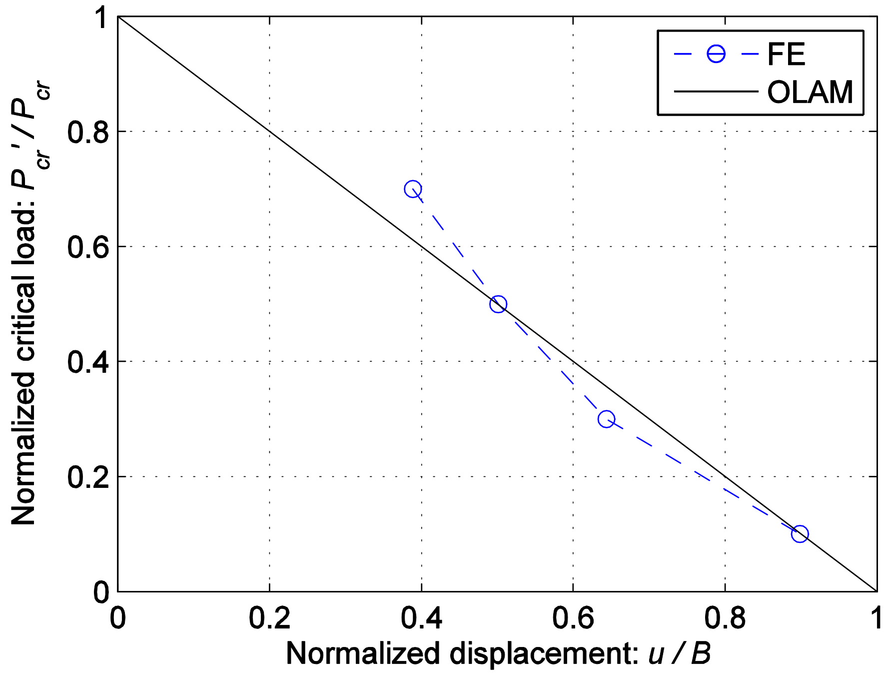

Figure A.7 Stability curve for b20tr375n20

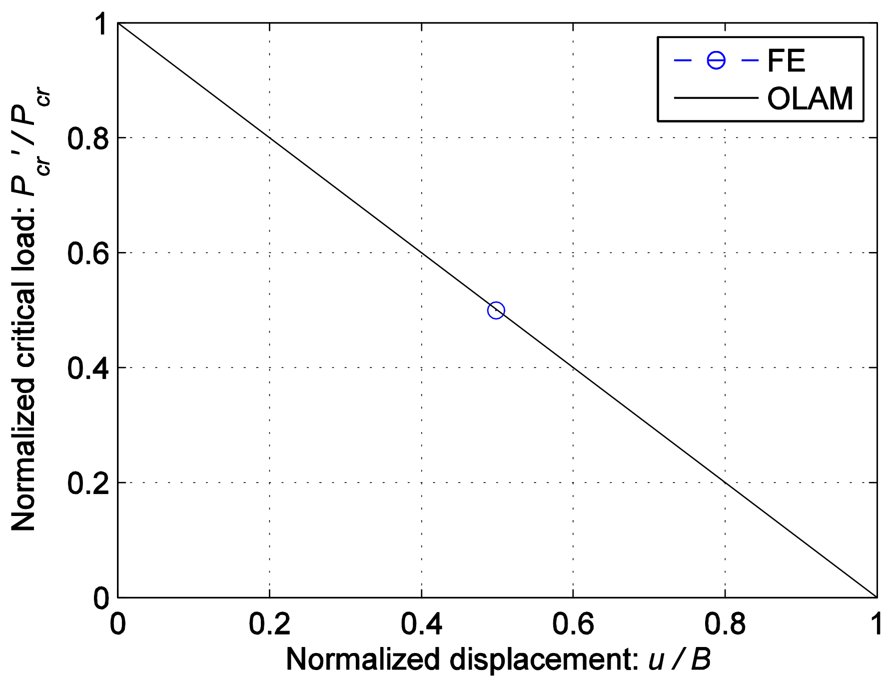

Figure A.8 Stability curve for b15tr375n5

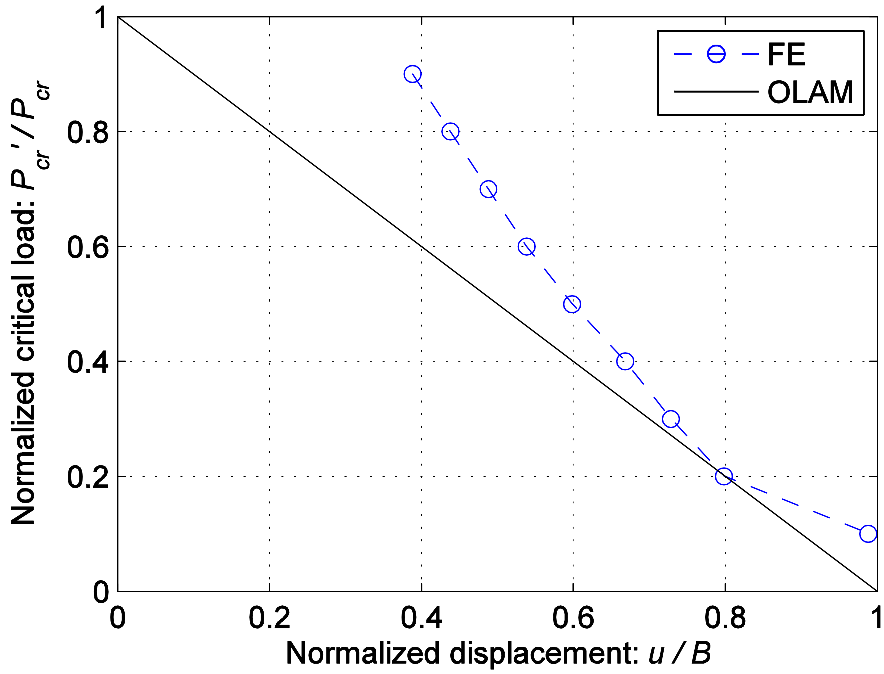

Figure A.9 Stability curve for b15tr375n10

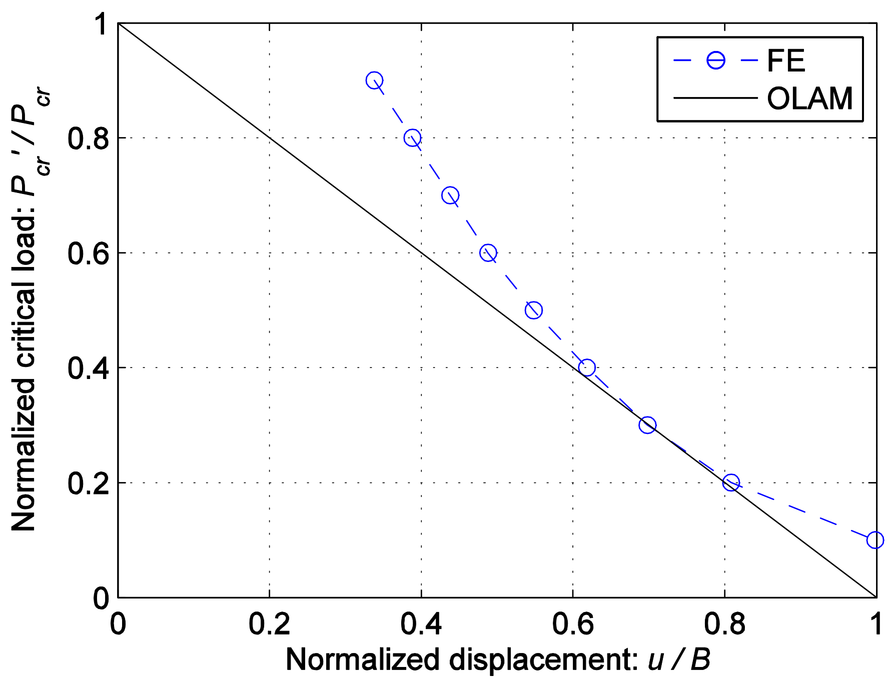

Figure A.10 Stability curve for b15tr375n15

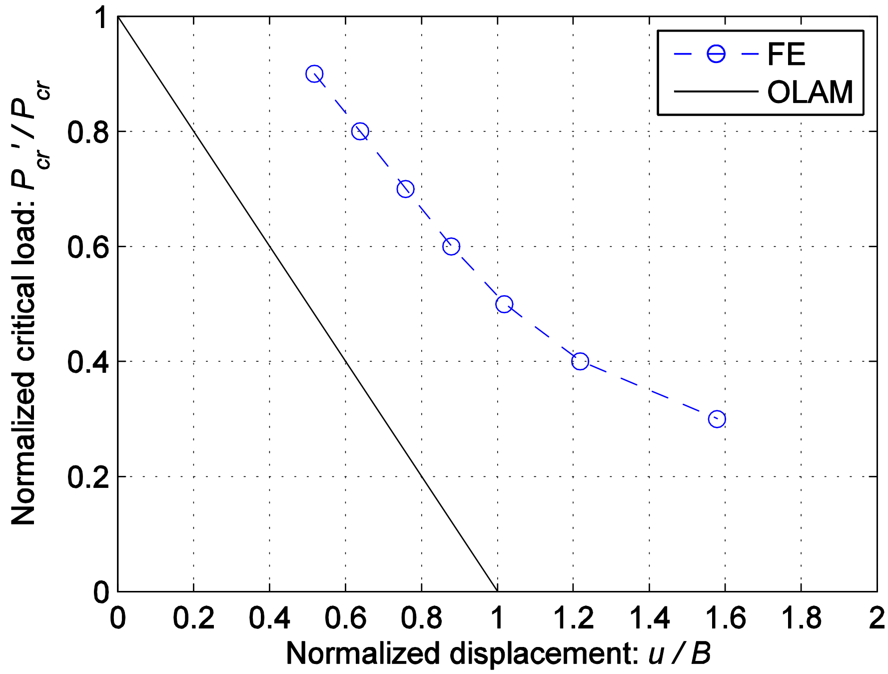

Figure A.11 Stability curve for b15tr1500n20

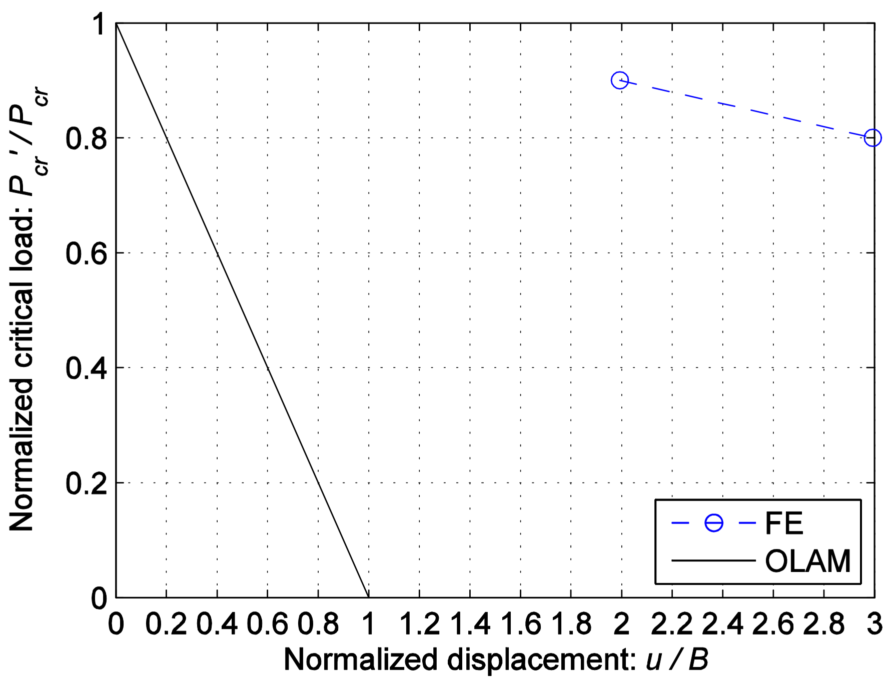

Figure A.12 Stability curve for b375tr375n20

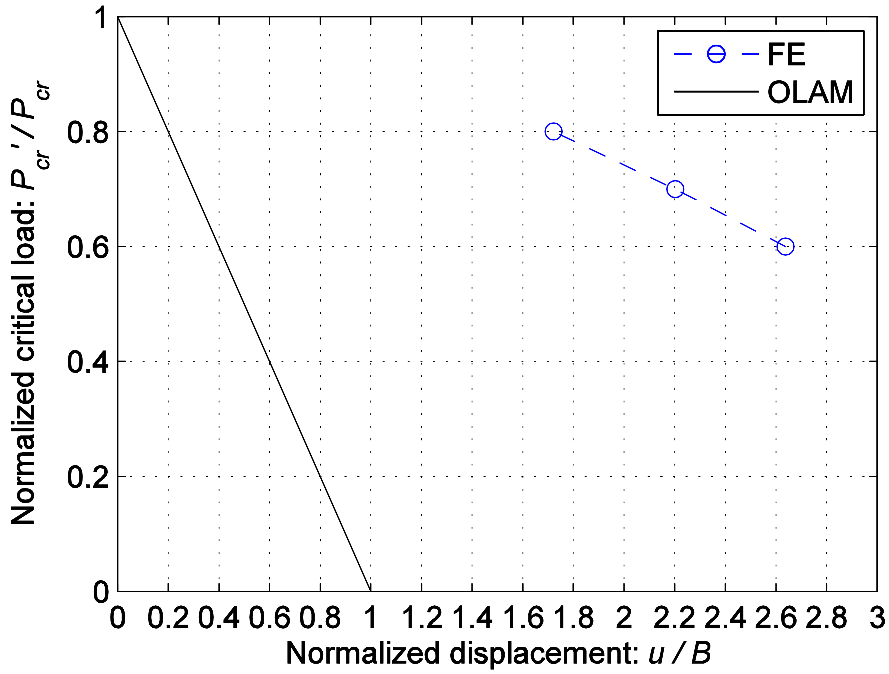

Figure A.13 Stability curve for b15tr3000n20

APPENDIX B

Data Processing

Data obtained from the stability testing at SUNY Buffalo was recorded into 71 electronic .ASC and .dat files. MATLAB was employed to reduce the data noise, zero correct, calibration correct, and gather the most relevant information concisely. The script (attached at the end of this section) was used to read in each file, add the weight of the steel plates (13.46 kips) which was not accounted for by the delta P cell to the axial load data, zero correct shear data (axial and displacement required no correction), then use a weighted average and decimating routine to remove noise and reduce data to a manageable size. Three different shear values were used for zero correction as each of the three bearing testing cycles began with a different residual shear reading. Figure B.1 shows an example (DP148_43d) with the decimated, weighted average plotted over the raw data. Figure B.2 shows the same graph after the script executes the 'relevant data' routine which only reads data where the specified displacement has been reached until the loading cycle ends.

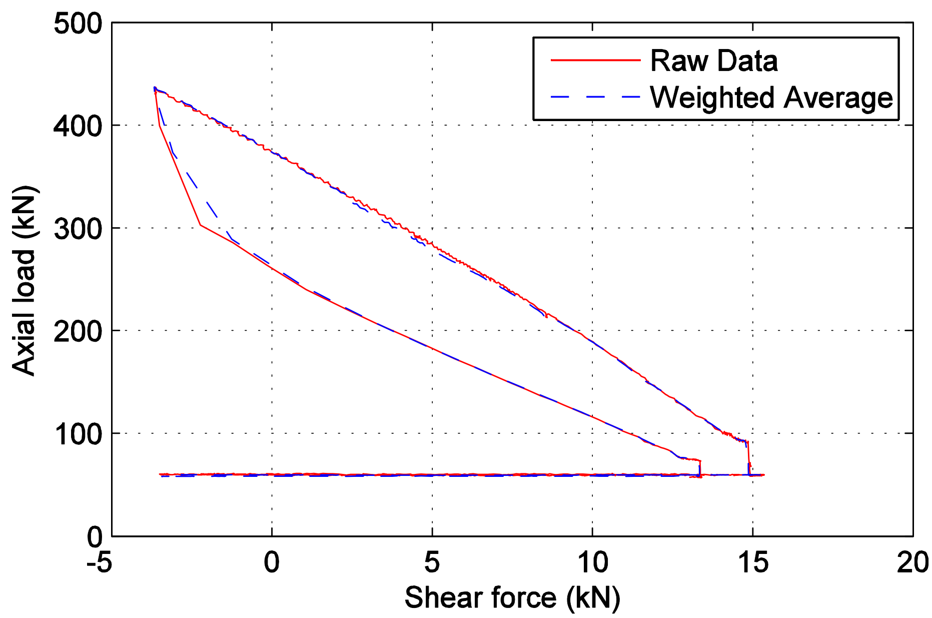

Figure B.1 Sample result from decimating routine

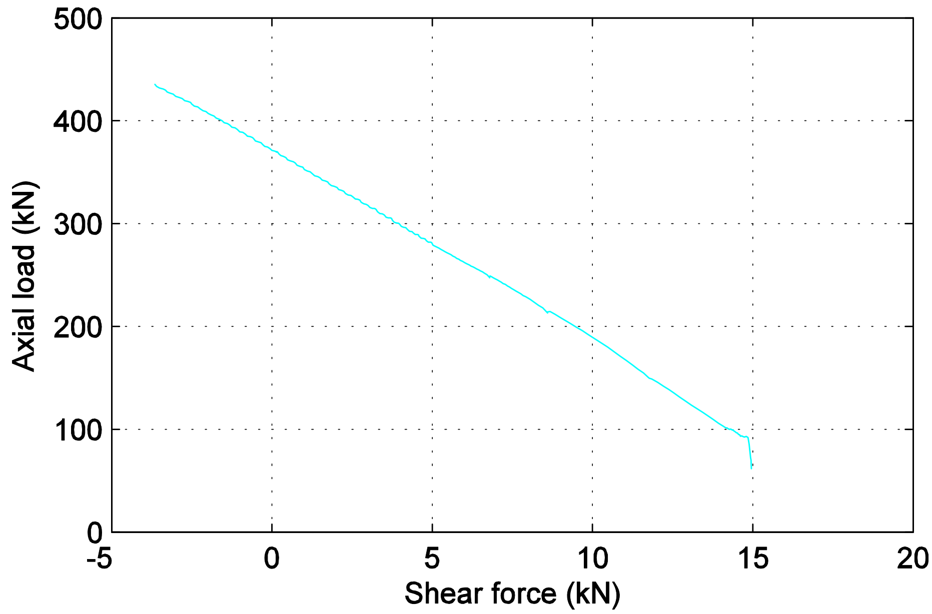

Figure B.2 Sample result from the 'relevant data' routine

MATLAB Script

```
%J.Weisman
%07/13/09
%Data Processing for Files from SUNY Buffalo

clear all;

%%%%%%%%%%%%%%%%%%%%%%%%%%%%%TESTS With .ASC
files%%%%%%%%%%%%%%%%%%%
Testsuf='_dat_1.ASC';
%Testsuf='.ASC';
FileName=['dg100-00.dat'];
%FileName=['dg100-14.dat'];
%FileName=['dg100-20.dat'];
%FileName=['dg150-00.dat'];
%FileName=['dg150-14.dat'];
%%%%%%%%%%%%%%%%%%%%%%%%%%%%%%%%%%%%%%%%%%%%%%%%%%%%%%%%%%%%%%%%%%%%%%%%%%%%%%%%
%%%
%%%%%%%%%%%%%BEARING 1 CRITICAL TESTS%%%%%%%%%%%%%%
%FileName=['DP127_~1_20090707_142047_0001_MD1' Testsuf];%
%FileName=['DP138_47_20090707_143130_0001_MD1' Testsuf];%
%FileName=['DP148_43_20090707_143737_0001_MD1' Testsuf];%
%FileName=['DP148_43b' Testsuf];%
%FileName=['DP138_47b' Testsuf];%
%FileName=['DP127_50b' Testsuf];%
%FileName=['DP127_50c' Testsuf];%
%FileName=['DP138_47c' Testsuf];%
%FileName=['DP148_43c' Testsuf];%
%FileName=['DP127_50d' Testsuf];%
%FileName=['DP138_47d' Testsuf];%
%FileName=['DP148_43d' Testsuf];%
%FileName=['DP169_36' Testsuf];%
%FileName=['DP191_32' Testsuf];%
%FileName=['DP212_27' Testsuf];%
%FileName=['DP085_68' Testsuf];%
%FileName=['DP064_73' Testsuf];%
%FileName=['DP254_21' Testsuf];%
%FileName=['DP254_21b' Testsuf];%
%FileName=['DP233_24' Testsuf];%
%FileName=['DP275_18' Testsuf];%
%FileName=['DP297_18' Testsuf];%
%FileName=['DP265_20' Testsuf];%
%%%%%%%%%%%%%%%%%%%%%%%%%%%%%%%%%%%%%%%%%%%%%%%%%%%%%%%%%%%%%%%
%FileName=['DP244_20' Testsuf];% Not a completed test.
%%%%%%%%%%%SHEAR TESTS, Bearing 1, LBTM%%%%%%%%%%%
```

```
%FileName=['DS168_13' Testsuf];
%FileName=['DS168_13b' Testsuf];
%FileName=['DS168_45' Testsuf];
%FileName=['DS168_60' Testsuf];
%FileName=['DS168_90' Testsuf];
%%%%%%%%%%%%%%%%%%%%%%%%%%%%%%%%%%%%%%%%%%%%%%%
%%%
%%%%%%%%%%%%%%%%%%%%BEARING 2 TESTS%%%%%%%%%%%%%%
%FileName=['DP180_34' Testsuf];%2
%FileName=['DP201_29' Testsuf];%2
%FileName=['DP117_55' Testsuf];%2
%FileName=['DP106_58' Testsuf];%2
%FileName=['DP095_65' Testsuf];%2
%FileName=['DP085_68_2' Testsuf];%2
%FileName=['DP074_71' Testsuf];%2
%FileName=['DP127_50_2' Testsuf];%
%FileName=['DP169_36_2' Testsuf];%2
%FileName=['DP222_25' Testsuf];%2
%FileName=['DP138_47_2' Testsuf];%2
%FileName=['DP148_43_2' Testsuf];%2
%FileName=['DP159_40_2' Testsuf];%2
%FileName=['DP191_32_2' Testsuf];%2
%FileName=['DP212_27_2' Testsuf];%2
%FileName=['DP233_24_2' Testsuf];%2
%FileName=['DP244_23_2' Testsuf];%2
%FileName=['DP254_21_2' Testsuf];%2
%FileName=['DP265_20_2' Testsuf];%2
%FileName=['DP275_18_2' Testsuf];%2
%FileName=['DP032_80_2' Testsuf];%2
%%%%%%%%%%%%%%%%%%%%%%%%%%%%%%%%%%%%%%%%%%%%%%%
%%%
%%%%%%%%%%%%%%%%%%%%%%LR TESTS%%%%%%%%%%%%%%%%%%%
%FileName=['DLP032' Testsuf];
%FileName=['DLP064' Testsuf];%%%CHANGE TO _dat_2.ASC
%FileName=['DLP085' Testsuf];
%FileName=['DLP106' Testsuf];
%FileName=['DLP127' Testsuf];
%FileName=['DLP148' Testsuf];
%FileName=['DLP169' Testsuf];
%FileName=['DLP191' Testsuf];
%FileName=['DLP212' Testsuf];
%FileName=['DLP233' Testsuf];
%FileName=['DLP254' Testsuf];
%FileName=['DLP275' Testsuf];
%FileName=['DLP297' Testsuf];
%FileName=['DLP042' Testsuf];
```

```
%FileName=['DLS169_14' Testsuf];
%FileName=['DLS169_50' Testsuf];



%%%%%%%%%%%%%%%%%%%%%%%%%%OPEN
FILES%%%%%%%%%%%%%%%%%%%%%%%%%%%%%%%%%%%%
%fid = fopen([FileName FileExtension]); % Open the file.  If this returns a -1, we did not open
the file successfully.
fid = fopen(FileName);
if fid==-1
  error('File not found or permission denied, recheck name and try again');
end

%%%%%%%%%%%%%%%%%%%%%INITIALIZE LOOP
VARIABLES%%%%%%%%%%%%%%%%%%%%%%%%%%%%
max_line=0;
nrows=0;
ncols=0;
data=[];

%%%%%%%%%%%%%%%%%%%%START PROCESSING
FILES%%%%%%%%%%%%%%%%%%%%%%%%%%%%%%%%%
line = fgetl(fid);
if ~isstr(line)
  disp('Warning: file contains no header and no data')
end;
[data, ncols, errmsg, nxtindex] = sscanf(line, '%f');
%ERRMSG is an optional output argument that returns an error message string if an error
occurred or an empty string if an error did not occur.
%NEXTINDEX is an optional output argument specifying one more than the number of
characters scanned in S.

while isempty(data)|(nxtindex==1)
  nrows=nrows+1;
  max_line = max([max_line, length(line)]);
  % Create unique variable to hold this line of text information.
  % Store the last-read line in this variable.
  eval(['line', num2str(nrows), '=line;']);
  line = fgetl(fid);
  if ~isstr(line)
    disp('Warning: file contains no data')
    break
    end;
  [data, ncols, errmsg, nxtindex] = sscanf(line, '%f');
  end % while
```

```
data = [data; fscanf(fid, '%f')];
fclose(fid);

header = setstr(' '*ones(nrows, max_line));
for i = 1:nrows
  varname = ['line' num2str(i)];
  if eval(['length(' varname ')~=0'])
    eval(['header(i, 1:length(' varname ')) = ' varname ';']);
    end
  end

eval('data = reshape(data, ncols, length(data)/ncols)'';', '');

%%%%%%%%Increase P by calibration factor, CF=1.185 and add self-weight%%%%%%
CF=1.185; %from actuator load cell vs reference load cell data see cal2_dat_2 and cal1_dat_1
SW=13.460; %self-weight of plates in kips, 2.6*3+2.584+3.076
data(:,5)=data(:,5)/CF;

%%%%%%%%%%%%%%%Zero Correct Axial Load, Displacement, and Shear
Force%%%%%%%%
zeroshear1=1.1165167E-001;
zeroshear2=3.7961567E-001;
zeroshear3=7.7039650E-001;

for i=1:length(data)
datao(i,1)=data(i,5)-data(1,5)-SW; %axial load
datao(i,2)=data(i,2)-data(1,2); %displacement
datao(i,3)=data(i,3)-zeroshear3; %shear
i=i+1;
end;

%%%%%%%%%%%%%%%%%WEIGHTED
AVERAGE%%%%%%%%%%%%%%%%%%%%%%%%%%%%%%
window=51; NCol=1;  %1=> axial load, 2=>displacement, 3=>shear
y=datao(:,NCol);

n=(window+1)/2;
w=zeros(1,window);
for i=1:n
   w(i)=i/n;
   w(window-(i-1))=i/n;
end
clear i;
```

```
a=(window-1)/2;

for i=1:length(y)-window
  if i<=window
    tmp(i)=0.5*y(i,1)+0.5*y(i+1,1);
  else
    tmp(i)=w*y(i-a:i+a,1)/sum(w);

    %tmp(i)=(w(1)*y(i-3,1)+w(2)*y(i-2,1)+w(3)*y(i-
1,1)+w(4)*y(i,1)+w(5)*y(i+1,1)+w(6)*y(i+2,1)+w(7)*y(i+3,1))/sum(w);
  end
end
clear i;

%fileout2='Processed Graph'
%f2=figure
%hold on
%grid on
%plot(datao(:,NCol),y,'r')
%plot(datao(1:length(y)-window,NCol),tmp,'b')
%print(f2,'-dpng',fileout2)
%axis([0,30,0,50])


%out=zeros(length(y)-window,2);
%out(:,1)=data(1:length(y)-window,1);
%out(:,2)=tmp';

%%%%%%%%%%%%%%%%%%%%%%%%%%%%%%%%%%%%%%%%%%%%%%%%%%%%%%%%%%%%%%%%%%%%%%%%%%%%%%%%%%%%%%%%%%%%%%%%
%%%%%%%%%%%%%%%%%%%%%%%%%%%%%%%%%%%%%%%%%%%%%%%%%%%%%
NCol2=2;  %1=> axial load, 2=>displacement, 3=>shear
y2=datao(:,NCol2);

n=(window+1)/2;
w=zeros(1,window);
for i=1:n
  w(i)=i/n;
  w(window-(i-1))=i/n;
end
clear i;


a=(window-1)/2;

for i=1:length(y2)-window
  if i<=window
```

```
      tmp2(i)=0.5*y2(i,1)+0.5*y2(i+1,1);
   else
      tmp2(i)=w*y2(i-a:i+a,1)/sum(w);

      %tmp(i)=(w(1)*y(i-3,1)+w(2)*y(i-2,1)+w(3)*y(i-
1,1)+w(4)*y(i,1)+w(5)*y(i+1,1)+w(6)*y(i+2,1)+w(7)*y(i+3,1))/sum(w);
   end
end
clear i;
%%%%%%%%%%%%%%%%%%%%%%%%%%%%%%%%%%%%%%%%%%%%%%%%%%%%%%%%%%%%
%%%%%%%%%%%%%%%%%%%%%%%%%%%%%%%
NCol3=3;  %1=> axial load, 2=>displacement, 3=>shear
y3=datao(:,NCol3);

n=(window+1)/2;
w=zeros(1,window);
for i=1:n
   w(i)=i/n;
   w(window-(i-1))=i/n;
end
clear i;


a=(window-1)/2;

for i=1:length(y3)-window
   if i<=window
      tmp3(i)=0.5*y3(i,1)+0.5*y3(i+1,1);
   else
      tmp3(i)=w*y3(i-a:i+a,1)/sum(w);

      %tmp(i)=(w(1)*y(i-3,1)+w(2)*y(i-2,1)+w(3)*y(i-
1,1)+w(4)*y(i,1)+w(5)*y(i+1,1)+w(6)*y(i+2,1)+w(7)*y(i+3,1))/sum(w);
   end
end
clear i;

%%%%%%%%%%%%%%%%%%%%%%%%%%%%%%%%%%%%%%%%%DATA
DECIMATION%%%%%%%%%%%%%%%%%%%%%%%%%%%%%%%%%%%%%%%%%%%%%
k=1;
for j=1:4:length(tmp) %take every 4th point starting at 1 i.e. 1,5,9 etc..
    datad(k,1)=tmp(j); %axial load
    datad(k,2)=tmp2(j); %displacement
    datad(k,3)=tmp3(j); %shear
    k=k+1;
end;
```

```
%%%%%%%%%%Remove Headers and Save to a
.txt%%%%%%%%%%file%%%%%%%%%%%%%%%%%%%%%%%%%%%
FileExtension2='.txt';
FileOut(:,1)=datad(:,1); %Decimated, Weighted Axial
FileOut(:,2)=datad(:,2); %Decimated, Weighted Displacement
FileOut(:,3)=datad(:,3); %Decimated, Weighted Shear
save(['1Processed ' FileName FileExtension2], 'FileOut','-ASCII', '-DOUBLE', '-TABS');

disp(['1Processed ' FileName])

%%%%%%%%%%%%%%STAGE 2 RELEVANT DATA
REPROCESSING%%%%%%%%%%%%%%%%

minindexfind=find(datad(:,1)<-13.75); %FINDS RELEVANT DATA
minindex=minindexfind(1);
maxindex=find(datad(:,1)==min(datad(:,1)));

datar(:,1)=datad(minindex:maxindex,1); %axial
datar(:,2)=datad(minindex:maxindex,2); %displacement
datar(:,3)=datad(minindex:maxindex,3); %shear

%%%%%%%%%%Remove Headers and Save to a
.txt%%%%%%%%%%file%%%%%%%%%%%%%%%%%%%%%%%%%%%
FileExtension2='.txt';
FileOut2(:,1)=datar(:,1); %Relevant Axial
FileOut2(:,2)=datar(:,2); %Relevant Displacement
FileOut2(:,3)=datar(:,3); %Relevant Shear
save(['1Reprocessed ' FileName FileExtension2], 'FileOut2','-ASCII', '-DOUBLE', '-TABS');
%FILE WITH RELEVANT INFORMATION

disp(['1Reprocessed ' FileName])
```

APPENDIX C

Supplemental Experimental Stability Data

Stability data not shown in Chapter 4 (Experimental Investigation) is presented. The shear force – axial load curves for the low damping rubber (LDR) and lead-rubber (LR) bearing are shown in Figs. C.1 and C.2 respectively. Figures C.3-C.7 provide individual LDR equilibrium paths while Figs. C.9-C.16 provide individual LR equilibrium paths. On each of these figures the critical displacement and axial load are indentified, as well as the coefficients of the best fit polynomial. Figs. C.8 and C.17 show all equilibrium paths for the LDR and LR bearing respectively to demonstrate the reduction in axial load with increasing shear force.

It should be noted that in the plotting of the LR bearing stability curve the equilibrium paths from shear forces of 25.3 kN and 27.0 kN were disregarded as the data collected did not allow for reasonable curve fitting (there is a near linear agreement between data points). Moreover, the data obtained from the test conducted at 25 mm was neglected in the determination of stability points as the results suggested the bearing was damaged.

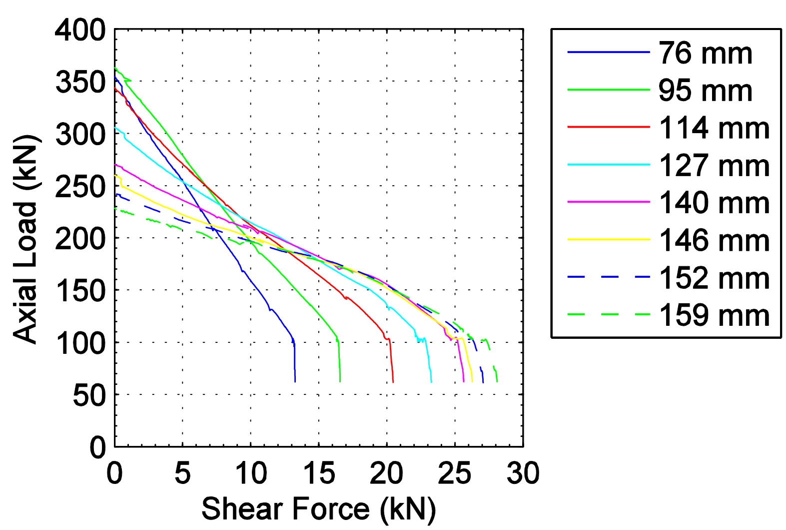

Figure C.1 LDR shear force – axial load plot

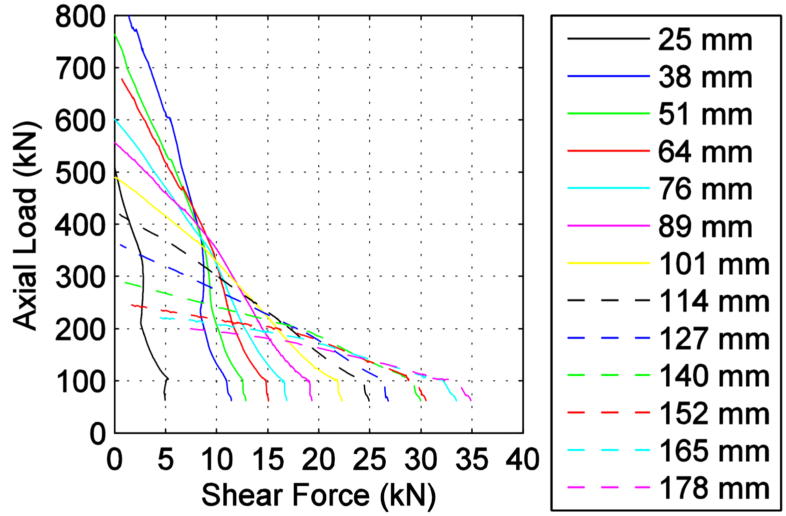

Figure C.2 LR shear force – axial load plot

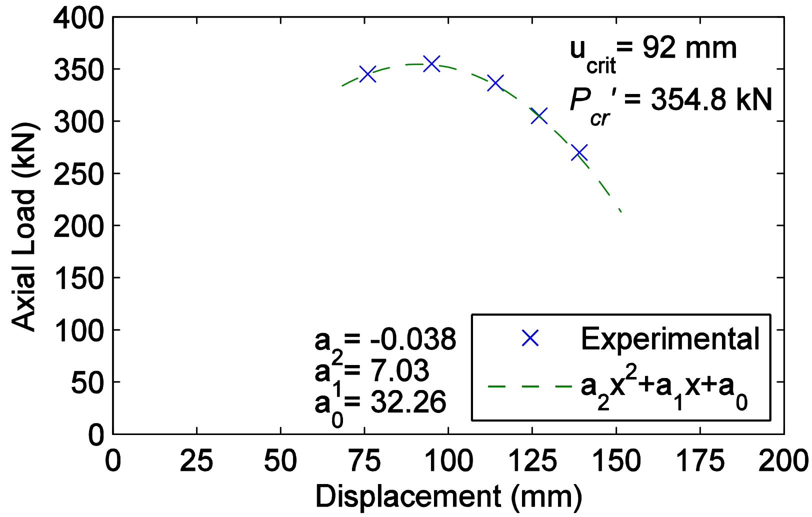

Figure C.3 LDR equilibrium path for *F*=0.4 kN

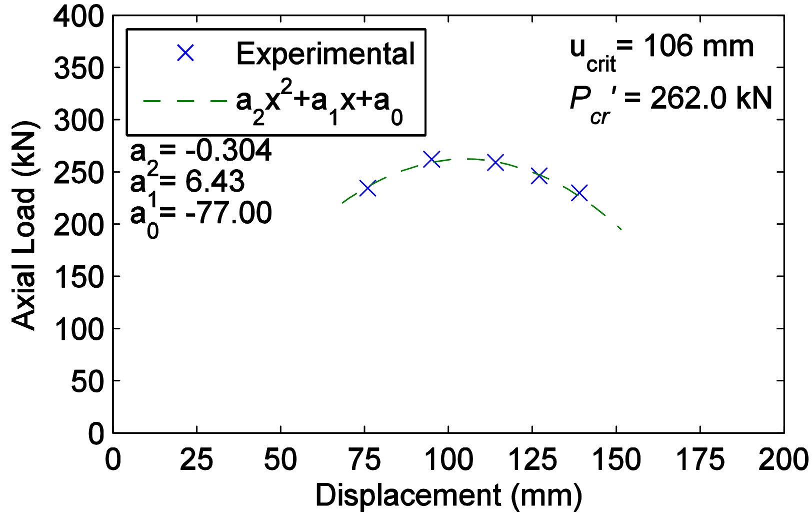

Figure C.4 LDR equilibrium path for *F*=6.0 kN

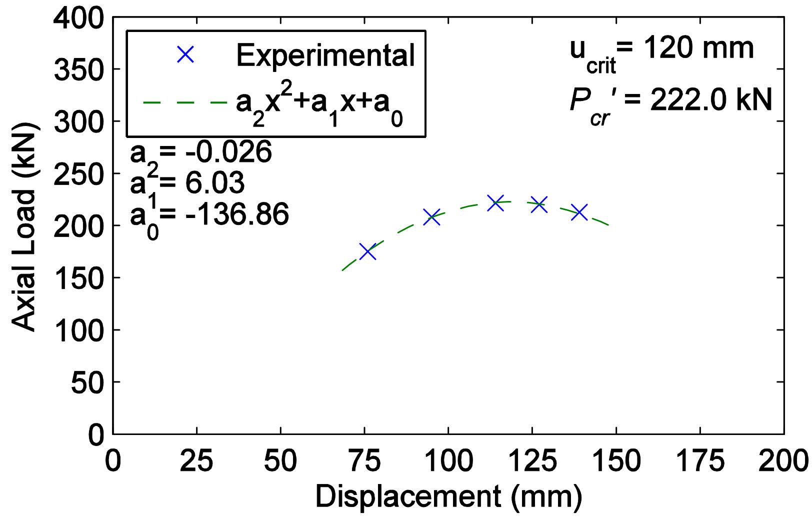

Figure C.5 LDR equilibrium path for *F*= 9.4 kN

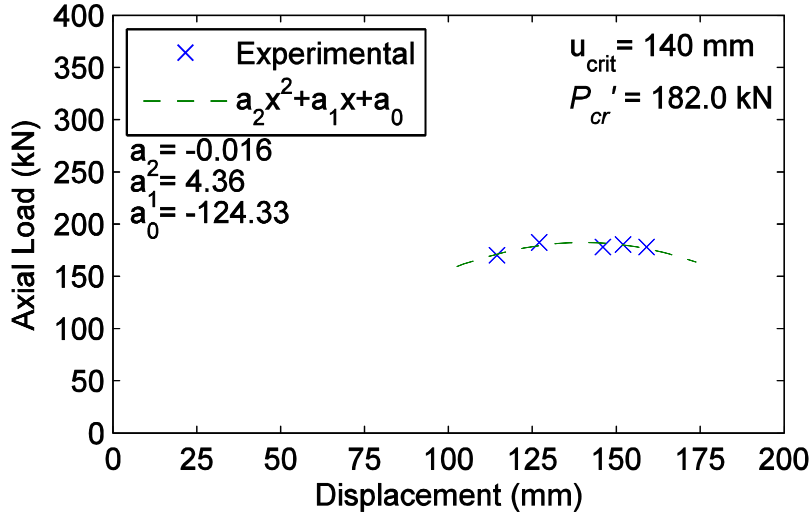

Figure C.6 LDR equilibrium path for *F*=14.9 kN

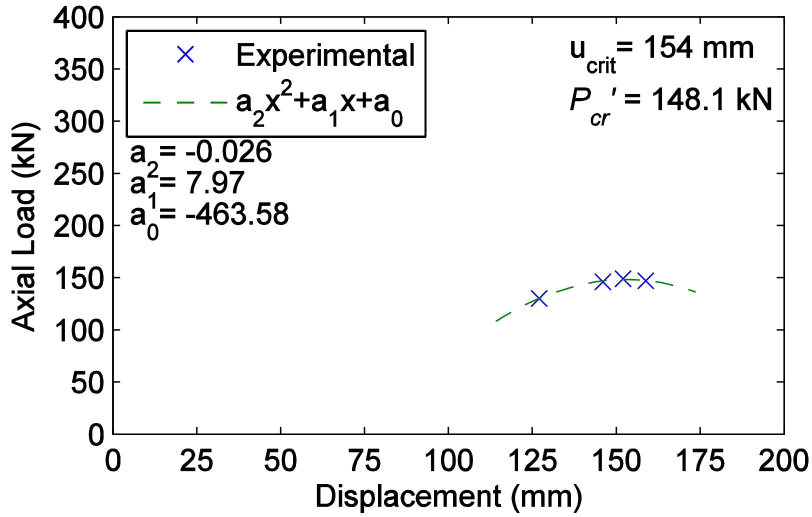

Figure C.7 LDR equilibrium path for *F*=20.7 kN

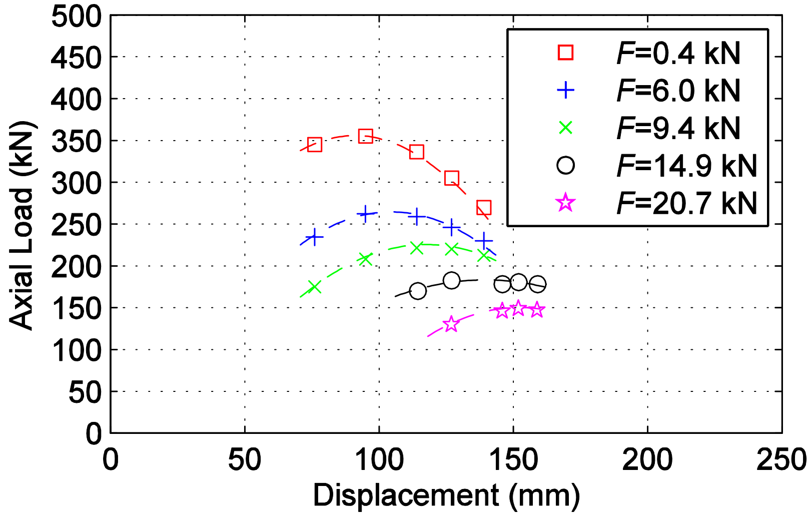

Figure C.8 All LDR equilibrium paths

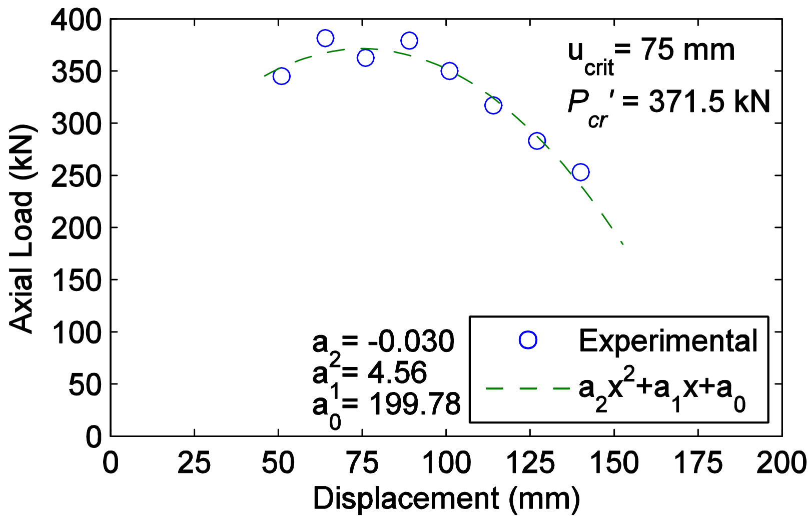

Figure C.9 LR equilibrium path for *F*= 9.0 kN

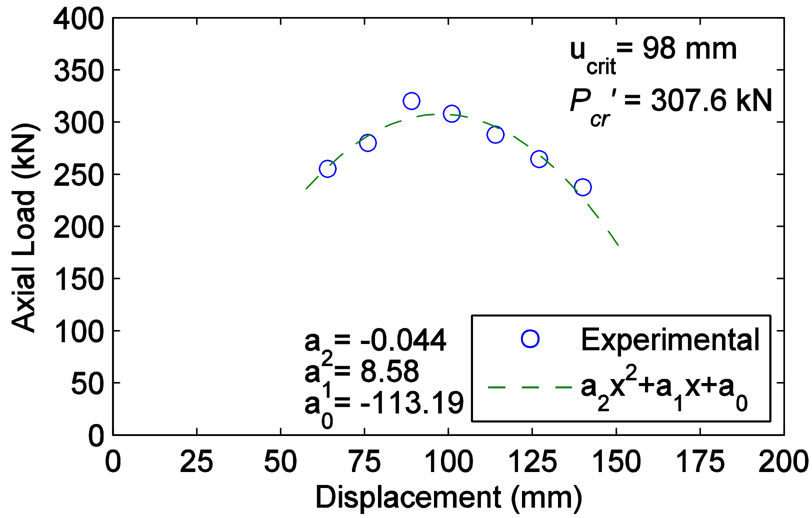

Figure C.10 LR equilibrium path for *F*=11.0 kN

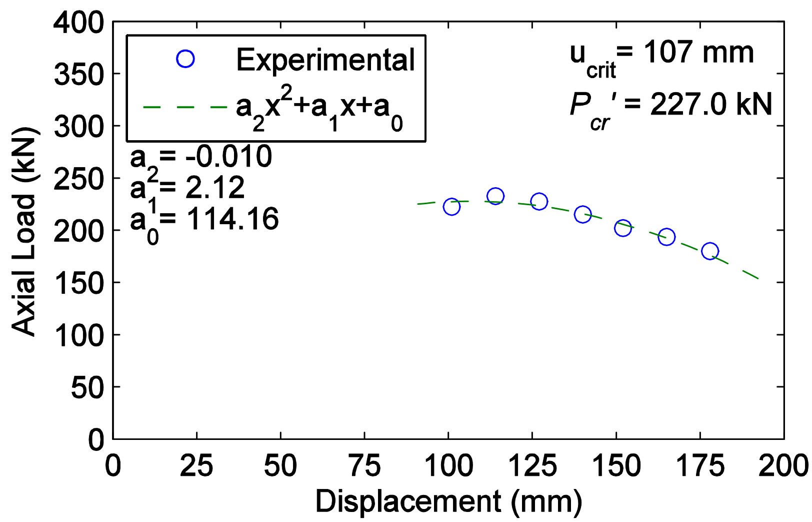

Figure C.11 LR equilibrium path for *F*=15.0 kN

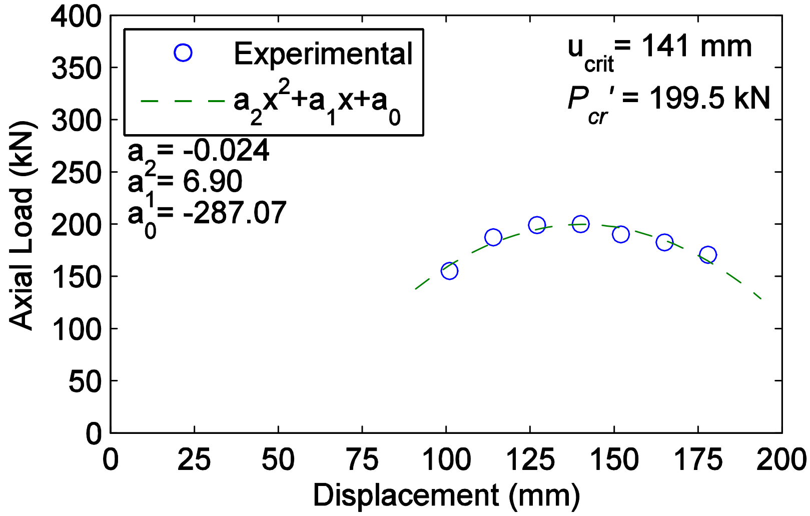

Figure C.12 LR equilibrium path for *F*=18.0 kN

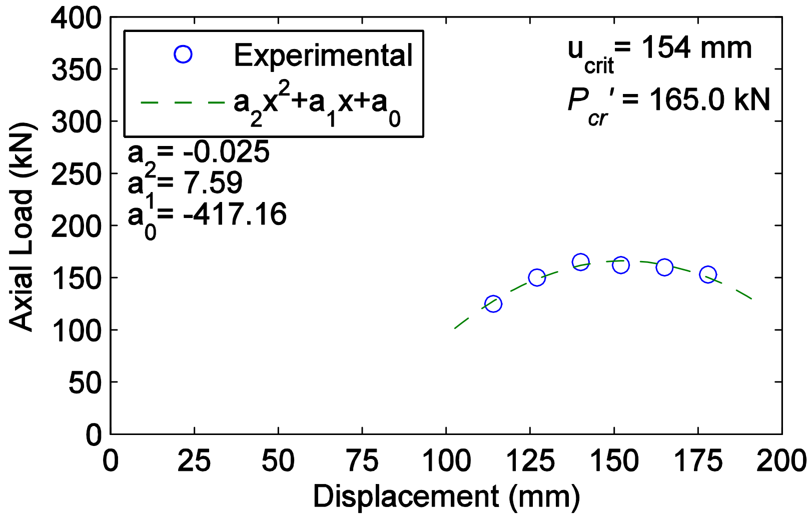

Figure C.13 LR equilibrium path for *F*=22.0 kN

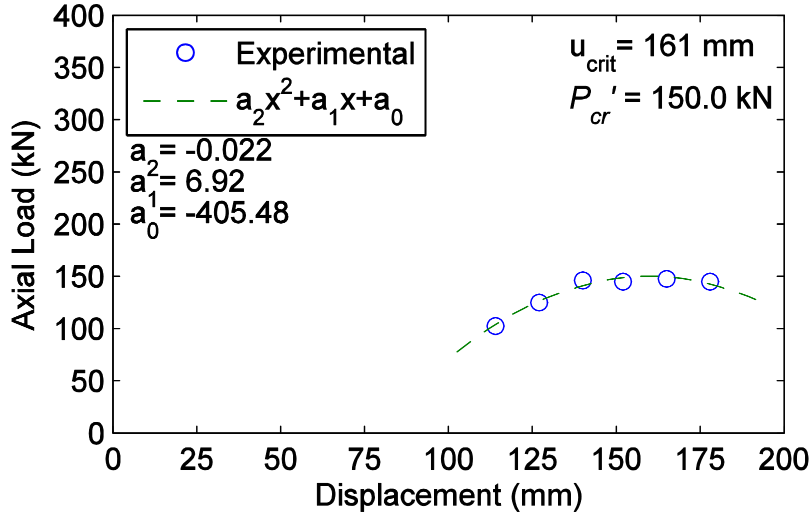

Figure C.14 LR equilibrium path for *F*=24.0 kN

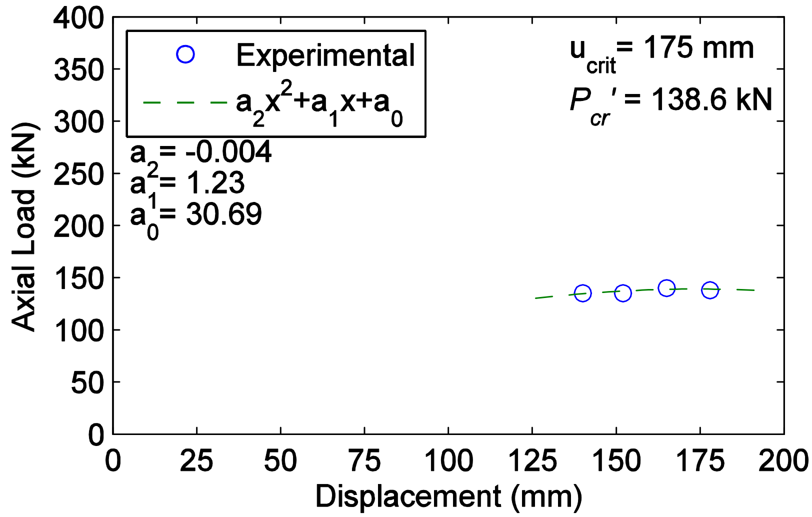

Figure C.15 LR equilibrium path for *F*=25.3 kN

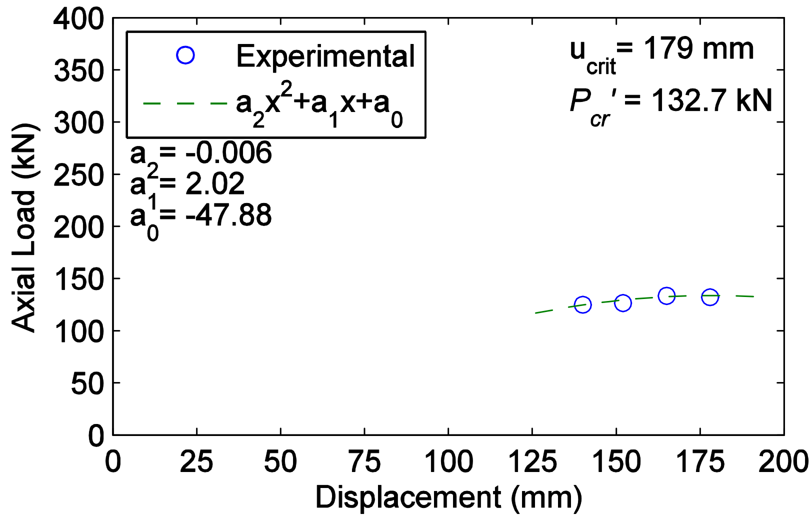

Figure C.16 LR equilibrium path for *F*=27.0 kN

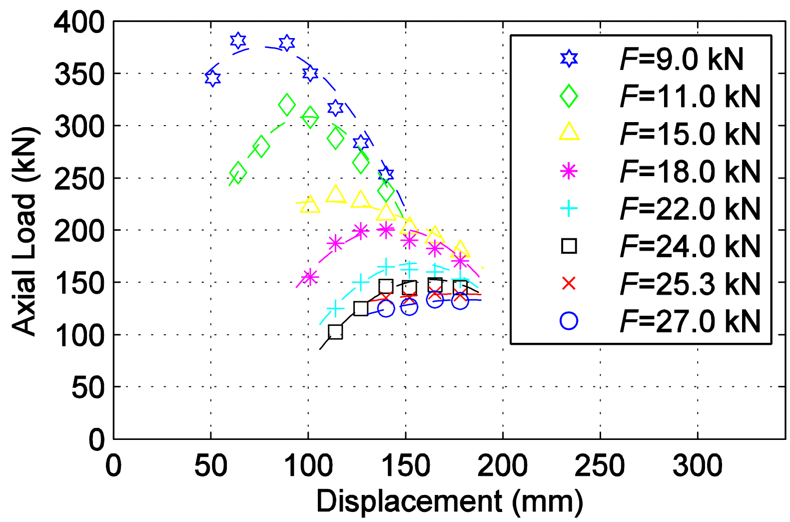

Figure C.17 All LR equilibrium paths